A numerical study for the interdecadal variation in the northern-hemisphere winter circulation

by

Jau-Ming Chen

A Dissertation Submitted to the

Graduate Faculty in Partial Fulfillment of the

Requirements for the Degree of

DOCTOR OF PHILOSOPHY

Department: Geological and Atmospheric Sciences
Major: Meteorology

Approved:

Signature was redacted for privacy.

In Charge of Major Work

Signature was redacted for privacy.

For the Major Department

Signature was redacted for privacy.

For the Graduate College

Iowa State University
Ames, Iowa

1995

UMI Number: 9531724

TABLE OF CONTENTS

ABSTRACT

It has been revealed in previous studies that one possible mechanism responsible for the interdecadal change of the Northern-Hemisphere (NH) circulation is the interdecadal sea-surface temperature (SST) change. It is thus hypothesized that the interdecadal SST change is one of the possible mechanisms to induce the interdecadal change of the NH winter circulation. To test this hypothesis, two multi-decade (1946-92) climate simulations were performed with the R15 resolution of the NCAR CCM1: one incorporating the 12 calendar month climatological SSTs, the other using the real-time SSTs. By contrasting the results of these two climate simulations, the effect of SST anomalies on the interdecadal change of the NH winter circulation was found to induce (1) the equatorward expansion of the circumpolar vortex, (2) the deepening of three climatological troughs, and (3) three interdecadal variation modes of stationary eddies: Pacific/North America (PNA), PNA west (PNAW), and North Atlantic (NA) modes. These three interdecadal modes were found to be equivalent barotropic in their vertical structure. Horizontally, both the PNA and PNAW modes exhibited a teleconnection pattern over the Pacific/North American region, while the NA mode possessed a north-south three-cell structure over the Greenland/North Atlantic

region. The temporal variations of these three modes consisted of a decadal trend and 15~20 year low-frequency oscillations.

The interdecadal variation of general circulation statistics is regulated by that of the atmospheric circulation. In the thermal field, the transient heat flux diverges out of the warm anomalies and converges toward the cold anomalies. In the dynamic field, the cyclone activity over the midlatitude storm track region is affected by the variability of the north-south wind shear which is induced by the equatorward expansion of the circumpolar vortex.

It is further demonstrated by linearized model simulations that (1) the tropical heating anomalies dominate over the extratropical heating anomalies as the primary mechanism to maintain the interdecadal change of the NH winter circulation, (2) the transient forcing anomalies are not important to the interdecadal circulation variability, and (3) the effect of the polar cooling is to amplify the stationary eddies.

I. INTRODUCTION

One of the least understood aspects of climate variability is the interdecadal change of the atmospheric circulation. In the past two decades, observational studies devoted to this phenomenon have focused on the Northern-Hemisphere (NH) winter circulation. This is merely due to the fact that the NH has the longest record, up to four decades, of observational data. Moreover, the intensity of the atmospheric circulation reaches its maximum in the winter season and hence the interdecadal circulation change is most likely to be significant in winter.

It was found by several observational studies that the interdecadal change of the NH winter circulation exhibits a spatial structure which resembles the Pacific/North America (PNA) teleconnection pattern (e.g., Douglas et al. 1982; Trenberth 1990; Shabbar et al. 1990). Numerous studies have demonstrated that the PNA teleconnection pattern associated with the El Nino/Southern Oscillation (ENSO) is the response of the midlatitude stationary waves to the change in tropical heating which is induced by the equatorial Pacific SST anomalies (e.g., Blackmon et al. 1983). Douglas et al. (1982) and Folland and Parker (1989) examined the interdecadal air-sea relationship over the Pacific and found a coherence between patterns of SST and the overlying atmospheric anomalies. Furthermore, Chen and Chen (1994) demonstrated that the interdecadal mode of the atmospheric circulation over the Pacific oscillates coherently with the interdecadal mode of the North-Pacific SST. The aforementioned observational studies suggest that the interdecadal change of the atmospheric circulation is closely correlated to the Pacific SST anomalies. However, the issue of cause-and-effect between the interdecadal changes of SST and atmospheric circulation forms a subtle problem for observational studies to resolve. This difficulty can be resolved by a numerical study.

Recently, Graham et al. (1994) conducted general circulation model (GCM) experiments forced by real-time SSTs for the period 1970-88 to explore the role of SSTs in producing atmospheric variability. They concluded that the observed decadal change of North Pacific (NP) winter circulation during the mid-1970s was forced by changes in tropical SSTs. It was thus substantiated numerically by Graham et al. that the interdecadal SST change is one possible mechanism to induce the observed interdecadal circulation variability.

After Graham et al.'s study, some questions related to the interdecadal climate change remain unanswered. Knox et al. (1988) analyzed the 500 mb height field for the years 1946-85 and found that the NH atmospheric circulation has two subclimate regimes: 1946-62 and 1963-85. Consequently, the decadal change of the atmospheric circulation is most significant between these two subclimate regimes. Apparently, Graham et al. only examined the interdecadal change within one subclimate regime, but not the most significant change between two subclimate regimes. Therefore, a numerical study is needed to explore the role of SST changes in the interdecadal circulation variability over both subclimate regimes, that is, for the period from the 1950s to the 1990s. Moreover, Graham et al. have confirmed the dynamic coupling between the SST changes and the decadal variability of the atmospheric circulation. However, they did not illustrate how this coupling is achieved. In other words, the dynamic processes associated with the interdecadal change of the ocean-atmosphere system have not been examined by a numerical study. Several questions related to these dynamic processes are raised:

(1) How did the interdecadal SST changes affect the interdecadal variation of the atmospheric circulation over the past four decades?

(2) What are the temporal and spatial characteristics of the atmospheric circulation induced by the interdecadal SST changes?

(3) What atmospheric processes are involved in shaping the spatial structure of interdecadal change in the

atmospheric circulation?

(4) How do the general circulation statistics respond to the interdecadal circulation changes?

(5) What are the roles played by different atmospheric forcings in the interdecadal circulation variability?

In order to answer the aforementioned five questions and to examine the role of SST anomalies in the interdecadal atmospheric variability, we performed both a GCM study and a linearized model study. Based upon the findings of previous studies concerning the possible relationship between the SST anomalies and the atmospheric circulation variability, the following hypothesis is introduced: *the interdecadal SST change is one of the possible mechanisms responsible for the interdecadal variation of the NH winter circulation.*

In order to test the hypothesis and also to answer the question (1) raised previously, two multi-decade (1946-92) GCM experiments, one incorporating 12 calendar month climatological SSTs and the other using real-time SSTs, were conducted with the version 1 of the National Center for Atmospheric Research (NCAR) Community Climate Model (CCM). The contrast between the results of these two simulations will explicitly reveal the effect of SST anomalies on the simulated interdecadal climate change. However, it is not our attempt to use these GCM experiments to simulate the real interdecadal climate change.

In order to answer question (2), a pattern analysis of correlation coefficients and an empirical orthogonal function (EOF) analysis were performed with the GCM data to identify interdecadal variation modes in the model NH climate system. The temporal and spatial properties of these interdecadal modes are thus portrayed as well.

The atmospheric processes mentioned in question (3) are examined from the interactions between the tropical diabatic heating and the planetary-scale atmospheric circulation. To portray these interactions, the χ(velocity potential)-maintenance (Chen and Yen 1991b) and ψ(streamfunction)-budget (Chen and Chen 1990) analyses are conducted.

The fourth question will be answered by examining the response of the general circulation statistics to the interdecadal changes of the atmospheric thermal and dynamic fields. Therefore, the interdecadal changes of the transient heat flux and cyclone activity will be compared with the interdecadal variations of temperature field and zonal flows, respectively.

In order to answer question (5), a hierarchy of linear model experiments incorporating different atmospheric forcings were performed to examine the relative importance of these forcings on the interdecadal atmospheric variability.

The remainder of this study described in detail the analyses and results that answer the fundamental questions listed above. The next chapter contains a review of past studies associated with the interdecadal climate variability. The results from the GCM experiment and the linear model experiment are contained in Chapter III and IV, respectively. In Chapter V, concluding remarks are made and suggestions for future study are proposed.

II. A REVIEW OF PAST STUDIES

Generally speaking, the research associated with a meteorological phenomenon can be categorized into the following four phases:

(1) discovering the phenomenon;

(2) understanding the characteristics of the phenomenon;

(3) proposing possible mechanisms; and

(4) verifying the proposed mechanisms.

The first three phases are commonly carried out by observational and diagnostic studies, and numerical or analytical studies are applied in the fourth phase. Past studies associated with the wintertime interdecadal climate variation are reviewed in accordance with these different phases of the research process.

A. The Observational Evidence

Willett (1950) combined temperature records from more than 100 stations and found a warming trend in the global winter mean temperature since 1885. Mitchell (1961) demonstrated that because of the various cells of the general circulation, secular temperature trend changes varied as much with longitude as they did with latitude. Inspired by Michell's study, van Loon and Williams (1976) attempted to relate the trends in temperature and circulation by compiling NH station data between 1900 and 1972. They showed that the regional trends of surface temperature are correlated with changes in the circulation on the scale of long waves.

Due to the increase of available observational data, the study of interdecadal climate change has attracted more research attention in the past one and a half decades. The interdecadal variation signal was found in the fields of geopotential height (e.g., Douglas et al. 1982; Knox et al. 1988; Shabbar et al. 1988; Chen et al. 1992), air temperature (e.g., Douglas et al. 1982; Jones 1988), pressure (e.g., Nitta and Yamada 1989; Trenberth 1990; Chen et al. 1992), moisture content (Hense et al. 1988), sea surface temperature (e.g., Posmentier et al. 1989; Chapman and Walsh 1993), and sea ice (Chapman and Walsh, 1993). These observational studies concluded that climate changes on the decadal time scale indeed took place in the ocean-atmosphere system. The characteristics of the aforementioned climate changes are discussed in detail in the next section.

B. The Characteristics of Interdecadal Climate Variability

Interdecadal climate change has been observed to be most significant in the Pacific/North America region, while some changes have also been reported in the North Atlantic (NA) and even the arctic areas. The reviews are therefore divided into three parts to outline the climate change in each region.

1. The Pacific/North America Region

Postmentier et al. (1989) analyzed the surface air and sea surface temperatures over the tropical Pacific and found that both have been increasing since 1960. The departure of 1977 through 1986 temperatures from the 1951-80 mean shows an increase in the vicinity of Alaska and a substantial decrease in the North Pacific (Folland and Parker 1989). In the latter region, the lower temperature was accompanied by a significant deepening of the Aleutian low (Trenberth 1990). The contrast of temperature anomalies over Alaska and the North Pacific suggests a change in the circulation regimes over this region. By investigating the spatial characteristics of the interdecadal change in the 500-mb height field from 1946-62 to 1963-85, Shabbar et al. (1990) found that the pattern of change resembles the positive phase of the PNA teleconnection pattern. This PNA-like pattern was later found in the correlations between the North Pacific sea level pressure (SLP) index and 700-mb temperature (Trenberth 1990), and in the EOF analysis for 500 mb height (Wallace et al. 1993).

Chen et al. (1992) studied the vertical structure of interdecadal variability by matching the interdecadal changes of wintertime SLP and 500-mb height between the first and the last decades in the period 1950-88. They asserted that the interdecadal variations of these two fields were nearly barotropic and took place on the scale of long waves. They also illustrated that the falls/rises of SLP and 500-mb height in the Pacific were associated with the intensification/weakening of the low-latitude westerlies.

2. The North Atlantic region

Since the 18th century, Europeans have noticed one peculiar climatic phenomenon: when the winter in Denmark was severe, the winter in Greenland was mild, and vice versa. This phenomenon illustrates the essential nature of the North Atlantic climate change: a north-south oscillation. van Loon and Rogers (1978) studied this oscillation in terms of winter temperature anomalies at Jakobshavn, Greenland, and Oslo, Norway. The temperature cospectrum between these two stations for the years 1873-1973 revealed the occurrence of decadal changes in a major frequency band centered around 14 years. Five-year running means of winter temperatures showed warming and cooling trends for Jakobshavn and Oslo, respectively. One decade later, Shabbar et al. (1990) illustrated that the change of 500 mb height from the periods 1946-62 to 1963-85 consisted of a minor increase in the vicinity of Iceland and a dramatic decrease over the entire subtropical North Atlantic.

For the ocean, Bjerknes (1964) detected an interdecadal warming trend in SST during the 1920s over the 30°-50°N band of the North Atlantic ocean. Deser and Blackmon (1992) studied the air-sea relationship by analyzing SSTs and surface circulations for winters from 1900-89. They pointed out that one important decadal variability mode is characterized by a dipole structure in SSTs and air temperatures, with anomalies of one sign east of Newfoundland, and anomalies of the opposite polarity off the southeast coast of the United States. Recently, Kushnir (1994) reported the NA air-sea relationship as in the mid-ocean area, the interdecadal warm/cool SST anomaly was accompanied by an anomalous cyclonic/anticyclonic surface circulation.

3. The arctic area

The temperature averaged over the polar cap (area poleward of 70°N) has exhibited a cooling trend since the 1950s (Wallace et al. 1993). Chapman and Walsh (1993) analyzed the wintertime temperature trends of the past three decades and showed that the warming occurred over northern North America and northern Asia, and the cooling took place over the Baffin Bay/Greenland area and eastern Siberia. In addition, the sea ice extent increased in the Baffin Bay/ Labrador Sea region and the Bering Sea, and decreased in the longitudes of the warming. In the dynamic field, Burnett (1993) found that the winter circumpolar vortex size, represented by the area poleward of 5454-meter 500 mb height contour, shows an expansion trend over the past four decades.

Past observational studies have found that the interdecadal variability of the atmospheric circulation was related to the variability of oceans through certain ocean-atmosphere interactions. This review also reveals that the previous research attention primarily focused on the PNA area, while the NA and the arctic regions received less attention. Consequently, the interdecadal circulation changes over the latter two regions remains largely unclear. At any rate, after the two-decade-long research effort, the observational studies have successfully portrayed the general characteristics of the interdecadal climate variability. However, they have fallen short of interpreting the findings to provide a comprehensive description of the dynamic processes related to this climate variability.

C. The Possible Mechanisms for Circulation Changes

Recently, Chen and Chen (1994) analyzed the observational data over the past four decades to study the interdecadal change of the ocean-atmosphere system. The major findings of their study are summarized as follows. (1) The interdecadal variation of the NH winter circulation over the past four decades results from the amplification of stationary eddies: the deepening of the three major stationary troughs, and weak amplification of the three major stationary ridges. (2) With some simple statistical analyses, two interdecadal variation modes of the NH winter circulation were identified: Pacific and Atlantic modes. The former mode exhibits a spatial structure similar to the Pacific/North America teleconnection pattern, while the latter mode possesses a spatial structure like the North-Atlantic oscillation. Furthermore, although these two interdecadal modes are characterized by an equivalent barotropic structure and have the same linear trend in their interdecadal evolution, they oscillate independently. The Pacific interdecadal mode oscillates coherently with the interdecadal mode of the North-Pacific SST. In contrast, the Atlantic interdecadal mode does not oscillate in a coherent way with that of the North Atlantic SST. (3) The Pacific interdecadal mode induces the equatorward shift of the North Pacific jet stream and the associated cyclone activity of the Pacific storm track. The Atlantic interdecadal mode causes a slightly poleward shift of the North Atlantic jet stream, but enhances the cyclone activity only along the Atlantic storm track.

Based upon the aforementioned results, Chen and Chen proposed three possible physical causes of the interdecadal variation of the NH winter circulation over the past four decades: (1) the amplification of stationary eddies by polar cooling, (2) the intensification of stationary eddies by the interdecadal warming of the tropical SST, and (3) the interdecadal variation of the Atlantic thermohaline circulation.

D. Numerical Study

As pointed out by Chen and Chen (1994), the interdecadal SST change is one possible mechanism for the NH interdecadal circulation variability. In addition, the polar cooling, which is related to the variability of the arctic sea ice, is also likely to affect the interdecadal variation of the NH circulation. Practically, the SST data is more readily available than the sea ice data. Therefore, the SST anomalies, rather than the sea ice anomalies, have been used in several numerical studies to simulate the interdecadal climate variability. Chen et al. (1992) performed two perpetual January experiments with Version 1 of the NCAR CCM by imposing the North Pacific (NP) SST anomalies during the decades 1950-59 and 1979-88, with respect to the 1950-88 mean, on the climatological SSTs. The results demonstrated that the observed PNA mode was apparently associated with the interdecadal Pacific SST changes. In a real-time simulation, Graham et al. (1993) imposed monthly-varying SSTs from 1970-88 on the GCM and demonstrated that the tropical SST changes were important to the major interdecadal change of NP circulation regime during the mid-1970s.

Both Chen et al.'s and Graham et al.'s studies substantiated numerically that the interdecadal SST anomalies are one possible factor for the interdecadal variability of the NH winter circulation. However, the former study can not portray the temporal characteristic of the interdecadal circulation variability, and the latter study only focused on the decadal change of NP circulation during the mid-1970s. In addition, neither study investigated the dynamic processes involved in inducing the atmospheric circulation variability. Therefore, a multi-decade GCM simulation incorporating SST boundary conditions is needed to study the characteristics of the interdecadal change in the ocean-atmosphere system over the past four decades, as well as the dynamic processes associated with this change. Only after the aforementioned characteristics and dynamic processes are understood, is it possible that one can improve the GCM experiment to reasonably simulate the real interdecadal climate changes.

The dynamic processes inferred from the GCM experiment are commonly verified by a linearized model simulation. This diagnostic technique has been applied to study the formation of wintertime stationary eddies (Nigam et al. 1986,1988) and the maintenance of the low-frequency atmospheric anomalies (e.g., Branstator 1992; Ting and Lau 1993). By examining the linear response to a particular component of the anomalous forcings, one can distinguish the relative importance of different individual processes to the total GCM response. The forcings often considered include diabatic heating, transient eddy forcing, and so on. On the decadal time scale, the relative importance of different atmospheric processes on the interdecadal variability of the NH winter circulation has not been examined.

III. GENERAL CIRCULATION MODEL EXPERIMENT

A. Introduction

As pointed out previously, SST anomalies lead to changes in tropical diabatic heating. These changes in tropical heating then induce changes in midlatitude stationary waves. In view of the above dynamic link, the interdecadal change of SSTs may be one of the major mechanisms responsible for the interdecadal variability of the NH atmospheric circulation. This was explored by Graham et al. (1994) with an 18-year simulation. They found that tropical SSTs are effective at inducing the interdecadal change of the simulated climate. However, in order to substantiate the hypothesis that the interdecadal SST change is a possible mechanism responsible for the interdecadal variability of the NH winter circulation, we shall impose the global SSTs on the GCM to simulate the atmospheric climate.

The objective of the GCM experiment study is to disclose the dynamic processes involved in the interdecadal change of the ocean-atmosphere system. These dynamic processes are interpreted from the response of GCM atmospheric circulation to the prescribed SST changes. In particular, four aspects of these dynamic processes are considered in detail: (1) the effect of interdecadal SST changes on the interdecadal atmospheric circulation variability, (2) the temporal and spatial characteristics of the interdecadal circulation variability, (3) the dynamic processes which determine the spatial structure of the model interdecadal variability, and (4) the response of general circulation statistics to the change in atmospheric circulation.

These four aspects of the interdecadal variability are analyzed with the following approaches. (1) The results from two multi-decade GCM simulations, with and without global SST anomalies, are contrasted to examine the effect of SST anomalies on the interdecadal changes of the NH winter circulation. (2) A pattern analysis of the correlation coefficient and EOF analyses is employed to depict the temporal and spatial characteristics of the simulated interdecadal variation modes. (3) The physical processes involved in shaping the spatial structure of the interdecadal variation modes are examined by the χ-maintenance and ψ-budget analyses. The former analysis depicts the relationship between the diabatic heating and divergent circulation, while the latter analysis portrays the dynamic processes associated with the mutual interaction between the divergent and rotational circulation. (4) The responses of the general circulation statistics to the interdecadal changes of atmospheric thermal and dynamic fields are analyzed in terms of the interdecadal variability of the transient heat flux and cyclone activity, respectively.

The outline of this chapter is as follows. Section B presents a brief description of the GCM used to perform the experiment. The design of the GCM experiment and SST dataset used to conduct the simulations are described in Section C. In Section D, the diagnostic methods for analyzing the simulation experiments are documented. Experiment results are presented and diagnosed in section E, and summarized and discussed in section F.

B. The Model

The model used to perform the GCM simulations is version 1 of the Community Climate Model (CCM1) developed at the National Center for Atmospheric Research (NCAR). There are three practical reasons for adopting this model: (1) the NCAR CCM1 is in the public domain and thus accessible to the entire meteorological community; (2) this model has been widely used in many studies, so its characteristics are well understood, and (3) the NCAR CCM1 can be run on a workstation which makes the study of long-term climate change possible with limited computer resources. An additional reason for using this model is related to the objective of this particular GCM study. As mentioned previously, this GCM study is simply a tool with which to examine the effect of SST anomalies on the variability of the atmospheric circulation. The NCAR CCM has been used for this purpose in numerous studies. For example, by prescribing ENSO SST anomalies in the CCM, Blackmon et al. (1983) has had some success in reproducing the observed PNA-like extratropical anomalies accompanying such events. Imposing the real-time Pacific SSTs on the CCM1, Chen and Yen (1994a,b) were able to simulate reasonably the interannual variations of summertime stationary eddies associated with the Indian monsoons and of the atmospheric circulation related to extreme ENSO events.

The CCM1 can be integrated with different horizonal resolutions. Chen and Tribbia (1993) compared the CCM1 climate simulations with different horizonal resolutions and concluded that the wintertime stationary eddies can be reasonably simulated by the CCM1 with the lowest resolution: rhomboidal 15-wave (R15) truncation. Thus, for this reason, and for the sake of conserving computer resources, the NCAR CCM1 with R15 truncation was adopted to perform the simulations. Readers are referred to Williamson et al.(1987) for a detailed description of the NCAR CCM1. A brief summary is presented here.

In accordance with Bourke et al. (1977) and McAvaney et al. (1978), the CCM1 was developed in terms of the vorticity and divergence equations derived from the primitive equations. This model is global and includes full physics.

Its horizontal domain is formulated with spherical harmonics. The vertical coordinate system has 12 discrete σ levels and uses an energy conserving finite difference scheme. The SST and sea ice distribution are specified from the climatological data compiled by Alexander and Mobley (1976) and are updated monthly for the seasonal cycle simulation. The instantaneous surface temperature over land, snow, and sea ice are calculated via a surface energy budget equation (Halloway and Manabe, 1971). The thickness of sea ice is prescribed to be 2m, while the snow depth and cover change with time. In the R15 version, the transform grid is 7.5° longitude by 4.5° latitude.

C. The Experiment

It is hypothesized in this study that the interdecadal SST change is one of the possible mechanisms to induce the interdecadal variability of the NH winter circulation. In order to test this hypothesis, two parallel multi-decade climate simulations were performed with the NCAR CCM1: a control experiment (EC) using 12 calendar month climatological SSTs over all oceans, and a real-time experiment (ER) incorporating the global real-time SSTs. The only difference between the two simulations is the SST anomalies. Thus, the role of SST anomalies on the interdecadal change of the atmospheric circulation can be revealed explicitly from the difference between the results of the ER and EC simulations.

The source of SST data for the simulations was the Comprehensive Ocean-Atmosphere Data Set (COADS, Woodruff et al. 1987). The data set spanned from 1854 up to the present. However, the data coverage became extensive only after 1950. In particular, the oceans were poorly sampled during the World War II (WWII). Furthermore, a change of measuring procedures around the beginning of WWII led to an apparent "warming" of measured SSTs since 1940 (Barnett 1984). Due to concerns as to the quality and consistency of the SST data, we started the simulation after the WWII period (1946-1992). The diagnostic analysis of the simulations focused only on the years 1950-92 because marine observations were more available, as well as reliable, in this period. During the simulation, the monthly-mean SST data were linearly interpolated into the daily data used in the model.

D. Diagnostic Methods

Descriptions of the diagnostic schemes used to evaluate the different model analyses are included in this section. These diagnostic schemes include (1) the isolation of the interdecadal variation component, (2) correlation coefficient and EOF analyses, (3) χ-maintenance and ψ-budget analyses, and (4) transient heat flux and cyclone activity analyses.

1. The isolation of the interdecadal variation component

Chen and Chen (1994) illustrated that over the past four decades the total variance of the wintertime 500 mb height field can be split between its interannual and interdecadal components in ratio of about 4 to 1, respectively. In order to specifically study the interdecadal climate variability, the interannual-variation mode must be removed. The interannual variation of winter circulation is highly linked to the recurrence of ENSO events, which occur at irregular intervals of 2 to 7 years. By excluding the variability induced by the ENSO events, the interdecadal-change mode can be reasonably isolated. Hence, the interdecadal variation component of any winter-averaged ( ) field is defined as its seven-year-running mean and is hereafter denoted as $(\tilde{\ })$.

2. Correlation coefficient and EOF analyses

Two features of the interdecadal circulation variability are particularly important in this study: temporal variation and spatial structure. The correlation coefficient pattern and EOF analyses are commonly used to diagnose these features. From the correlation coefficient distribution, it is possible to infer the basic structure of one variable's temporal variation as it corresponds to another's. Different correlation patterns indicate different circulation regimes. For example, Wallace and Gutzler (1981) used the 500 mb height correlation coefficients to identify several teleconnection patterns associated with the wintertime atmospheric low-frequency mode. However, the correlation coefficient cannot distinguish the relative importance between different circulation regimes, nor can it depict the temporal variation of these regimes.

The deficiencies of the correlation coefficient analysis are not present in an EOF analysis. For any mode identified by the EOF analysis, its temporal variation and spatial structure are illustrated by each mode's eigencoefficient and eigenvector, respectively. Because of the EOF's orthogonal character, all of its modes are regarded as independent from each other. The relative importance of a mode is measured by the percentage of total variance explained by the mode. A detailed description of the EOF procedure can be found in Kutzbach (1967).

By applying the pattern analysis of the correlation coefficients and the EOF analysis, one can identify different interdecadal variation modes simulated in the model. After these interdecadal modes are identified, we next diagnose the dynamic processes responsible for these modes in terms of the χ-maintenance and ψ-budget analyses.

3. χ-maintenance and ψ-budget analyses

The χ-maintenance equation proposed by Chen and Yen (1991a) is the inverse Laplacian of the combined continuity and vertically differentiated thermodynamic equations:

$$\chi = \nabla^{-2}\left[\frac{\partial}{\partial p}\left(\frac{1}{\sigma C_p}\dot{Q}\right)\right] - \nabla^{-2}\left\{\frac{\partial}{\partial p}\left[\frac{1}{\sigma}\left(\frac{\partial T}{\partial t} + V\cdot\nabla T\right)\right]\right\}$$

where $\sigma = -(T/\theta)(\partial\theta/\partial p)$, and $\dot{Q}$ is diabatic heating. This equation indicates that the maintenance of the global-scale divergent circulation is attributed to the vertical differential diabatic and adiabatic heating. Chen and Yen further demonstrated that in the 30-60 day mode, the divergent circulation is primarily maintained by diabatic heating through the latent heat released by cumulus convection.

The global-scale divergent circulation can interact with the rotational circulation to maintain/adjust the rotational flows. Chen and Chen (1990) used the ψ-budget analysis to illustrate the physical processes involved in the interactions between the planetary-scale divergent and rotational circulations. The ψ-budget equation reads:

$$\frac{\partial\psi}{\partial t} = \nabla^{-2}\left[-V_\psi\cdot\nabla(\zeta+f)\right] + \nabla^{-2}\left\{-\nabla\cdot\left[V_\chi(\zeta+f)\right]\right\} + \nabla^{-2}F$$

or $\frac{\partial\psi}{\partial t}=\psi_{AV}+\psi_{\chi}+\psi_{F}$

where V_{ψ} and V_{χ} are rotational and divergent wind vectors, respectively, and F includes vertical advection, twisting, and dissipation of vorticity. Using the 200 mb winter-mean eddy streamfunction (ψ_E) as an example, Chen and Chen illustrated that the streamfunction tendencies induced by the vorticity advection (ψ_{AV}) and vorticity source (ψ_{χ}) are spatially in quadrature with the stationary eddies; and the counterbalance of ψ_{AV} and ψ_{χ} is the primary mechanism for maintaining these stationary eddies. The physical processes associated with the ψ_F term are generally insignificant.

4. Transient heat flux and cyclone activity analyses

In accordance with the interdecadal change of the atmospheric circulation, the general circulation statistics should also experience interdecadal variability. In this study, we analyzed the interdecadal variations of the general circulation statistics for both the thermal and dynamic fields.

In the thermal field, the contribution of transient eddies to the thermal structure can be illustrated as

$$\frac{\partial T}{\partial t} \sim -\nabla\cdot(V'T'),$$

where the prime indicates the departure from the time mean. The characteristics of the transient heat flux has been examined in several studies. Chen (1982) studied the spectral energetics of the Northern Hemisphere in the winter season and found that both the standing and transient waves contribute to the total eddy sensible heat transport. The contribution from the standing waves is larger than that from the transient waves. In other words, the standing waves are the major agent of the total eddy sensible heat transport. Blackmon et al. (1977) computed the root-mean-square (RMS) patterns of the bandpass (2.5-6 days) filtered temperature and meridional heat transports at 850mb. Both RMS patterns are characterized by elongated bands of large variability near 45°N, which correspond closely to the North Atlantic and Pacific storm tracks. Blackmon et al.'s results indicate that the variability of the temperature field is related to that of the high-frequency transient eddy heat transports. Therefore, we analyzed the effect of transient eddies on the interdecadal variability of the thermal field in terms of the potential function of the divergence of 850 mb high-frequency heat flux, i.e., $\chi_{HF} = \nabla^{2}[-\nabla\cdot(\overline{V''T''})]$. The double prime denotes the 2.5-6 day filtered field, and the overbar refers to the winter mean. The reason for using χ_{HF} rather than $-\nabla\cdot(\overline{V''T''})$ is to take the advantage of the former field's broader scale structure which can facilitate the comparison between the variations of the transient heat flux and the temperature field.

Also examined in this study is the effect of transient eddies on the interdecadal variability of the zonal-mean thermal field. We analyzed the standing and transient components of the zonal-averaged meridional sensible heat transports in terms of $(\bar{v}_E\bar{T}_E)_Z$(850 mb) and $\overline{(v''_E T''_E)}_Z$(850 mb), respectively. The subscript E and Z denote the eddy and zonal-mean components, respectively. The reason for analyzing both the standing and transient components is based upon Chen's (1982) result that both the standing and transient waves play important roles in the total sensible heat transport. A first-order Butterworth bandpass filter was employed to extract the high-frequency (2.5-6 days) mode from the 90-day winter daily data.

For the dynamic field, one significant transient activity is associated with cyclones near the storm track regions. Blackmon et al. (1977) showed that the RMS distribution of the 2.5-6 day filtered 500 mb geopotential height is characterized by distinctive elongated maxima extending across much of the North Atlantic and Pacific along the major storm tracks. They also illustrated that the positions of storm tracks are highly correlated with those of the subtropical jet streams. Based upon Blackmon et al.'s results, we analyzed the interdecadal variability of cyclone activity in terms of the winter-mean RMS values of the 2.5-6 day filtered ψ(200 mb) anomalies. However, only the short-wave regime (wavenumbers 5-15) of ψ(200 mb) is included in the analysis. This linked regime was considered because the high-frequency variability of long waves (small wavenumbers) can be explained in terms of travelling planetary Rossby waves (e.g., Madden 1979; Madden and Labitzke 1981) rather than cyclone activity.

E. Results

The results of the GCM simulations are analyzed in such a way as to answer the first four questions raised in the Introduction of this study. The outline of this section is as follows. (1) To be sure that the GCM can properly simulate the atmospheric climate, we first examined the winter climatologies of the model circulation. (2) In order to investigate the effect of SST anomalies on the interdecadal climate change (i.e., the first question) and the characteristics of the model interdecadal circulation variability (i.e., the second question), we analyzed the interdecadal variations of the model total field and the stationary eddy field. (3) To illustrate the dynamic processes associated with the maintenance of the interdecadal variability of the model circulation (i.e., the third question), the possible effect of tropical heating on the atmospheric anomalies was analyzed in terms of the χ-maintenance and ψ-budget analyses. (4) The response of the general circulation statistics to the interdecadal change of the atmospheric circulation (i.e., the fourth question) was analyzed in terms of the interdecadal changes of the transient heat flux and cyclone activity.

The diagnostic analyses of the simulations performed in this study were conducted on areas north of 20°N. This region was chosen because the major response of the atmospheric circulation to the interdecadal SST changes occurs in the extratropics and high latitudes (e.g., Chen et al. 1992). To delineate the horizonal structure of the atmospheric circulation, geopotential height and streamfunction have often been used. In addition, a linearized model written in the primitive equation (PE) form was used here to examine the dynamic processes identified in the maintenance of the interdecadal variation modes. Since streamfunction is the common variable used in both the GCM and the linearized model, we decided to use it for the diagnostic analyses.

1. Climatology of the simulated winter circulation

To portray the climatologies of the winter (December-February) circulation simulated in the ER experiment, the 43-winter (1950-1992) averaged streamfunction ($\overline{\psi}$) and its asymmetric components, namely eddy streamfunction ($\overline{\Psi}_E$), at 200 mb and 850 mb are shown in Figure 1. The year assigned to each winter refers to the year in which January and February occur. Furthermore, ($\overline{\ }$) hereafter denotes the 43-winter mean of ( ). Since both the EC and ER experiments were forced by SST fields which have the same climatological mean and annual cycle, the simulated climatologies of these two experiments should resemble each other. In fact, the $\overline{\Psi}$ and $\overline{\Psi}_E$ fields from the EC experiment (not shown) do not differ noticeably from their ER counterparts. For the sake of brevity, we shall focus the discussion on the ER case.

The $\overline{\Psi}$(200 mb) field (Figure 1a) exhibits three major troughs over the east coasts of the Asian, North American, and North African continents. In addition, three major ridges are located over the west coasts of North America, the eastern Atlantic, and central Asia. In the subtropics, three subtropical jetstreams with wind speed greater than 35 ms^{-1} (heavily shaded) are located over the regions with the sharpest $\overline{\Psi}$ gradients: the East Asia/western Pacific, eastern North America, and North Africa/Middle East areas. In the lower troposphere, the salient features of the $\overline{\Psi}$(850 mb) field are the Aleutian low over the North Pacific and the Icelandic low over northeastern North America.

In order to more clearly illustrate the structure of asymmetric components, $\overline{\Psi}_E$(200 mb) is displayed in Figure 1c.

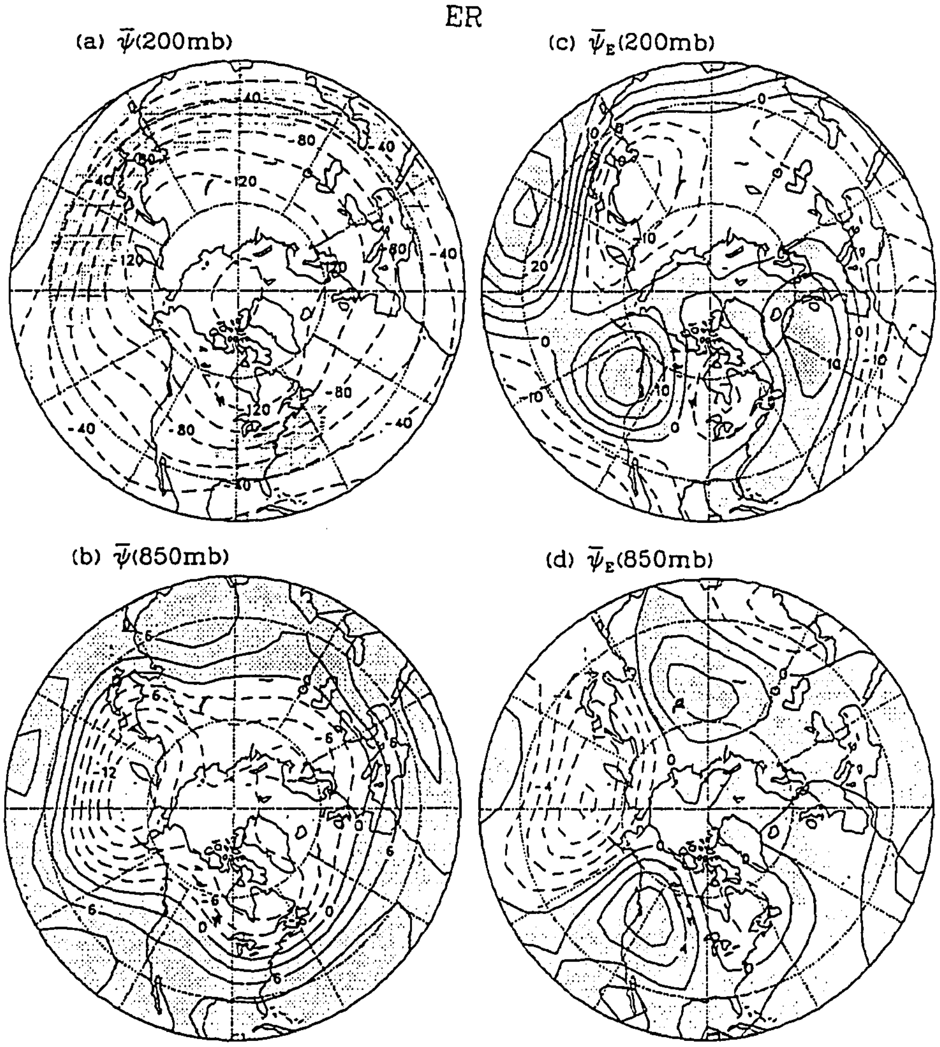

Figure 1. The multiple (1950-92) winter-mean total streamfunction ($\overline{\Psi}$) and eddy streamfunction ($\overline{\Psi}_E$) at 200 mb and 850 mb: (a) $\overline{\Psi}$(200 mb), (b) $\overline{\Psi}$(850 mb), (c) $\overline{\Psi}_E$(200 mb), and (d) $\overline{\Psi}_E$(850 mb). The positive values of $\overline{\Psi}$ and $\overline{\Psi}_E$ are shaded. The isotachs greater than 35 ms^{-1} are superimposed and heavily shaded on the $\overline{\Psi}$(200 mb) contours. Contour intervals: (a) $2x10^7$ m^2s^{-1}, (b) $3x10^6$ m^2s^{-1}, (c) $5x10^6$ m^2s^{-1}, and (d) $2x10^6$ m^2s^{-1}.

The $\overline{\Psi}_E$(200 mb) field is characterized by distinct low- and high-latitude regimes with a sign reversal at about 30°N. In high latitudes, major low centers are located near the east coasts of the Asian and North American continents, while the major high centers are near the west coasts of North America and Europe. The major low centers are accompanied by subtropical high centers forming doublets with negative-positive cellular structure. The subtropical jetstreams are situated between the centers of the doublets. The high-latitude high and low centers in the $\overline{\Psi}_E$(850 mb) field (Figure 1d) are located eastward of their 200 mb counterparts. The baroclinicity of high-latitude circulation regimes is characterized by the westward tilting of low and high centers from 850 mb to 200 mb.

To verify the simulation performance, we used the 1979-92 winter climatologies constructed from the data generated by National Meteorological Center (NMC) (Figure 2). The comparison between the NMC and ER climatologies reveals that the structure and salient features of the simulated circulations are relatively consistent with those of the observed. However, a systematic discrepancy does exist: the intensity of model circulations is weaker than the observed. For example, the maximum wind speed of the observed jet cores over North Africa, the western Pacific, and North America are (49,70,45) ms^{-1}, respectively, while those of the ER 200 mb

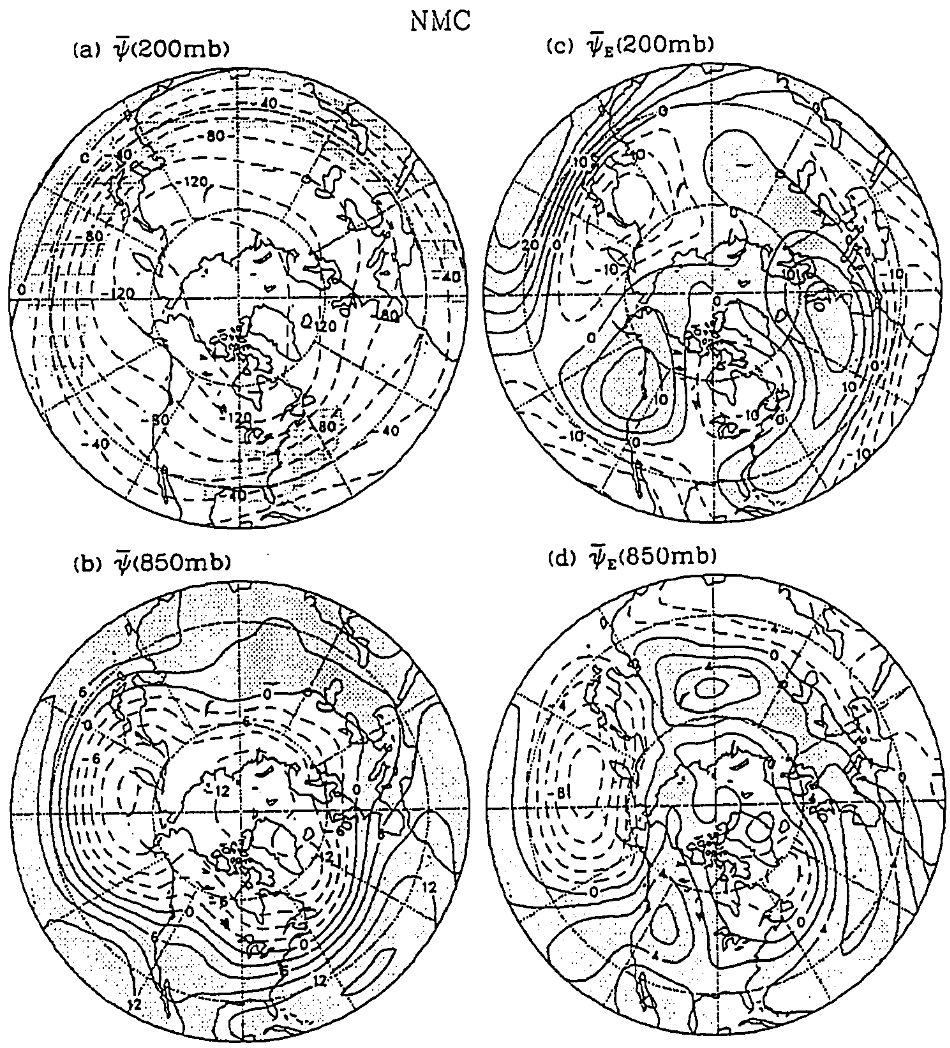

Figure 2. As in Figure 1, except for the 1979-92 winter climatologies of NMC data.

circulation are (38,61,44) ms^{-1}, respectively. For the eddy fields at 200 mb and 850 mb, the low center east of North America and the high center over the eastern Atlantic are clearly undersimulated in the ER experiment.

2. Interdecadal change of total field

In order to study the characteristics of the model interdecadal climate change as well as the effect of SST anomalies on that change, we first examined the interdecadal variation of the total field. The interdecadal change of the total field is analyzed in terms of the Ψ field. The variance of the Ψ(200 mb) field can be revealed from the distribution of RMS values of this field's departure from $\overline{\Psi}$(200 mb), i.e., RMS[$\Delta\Psi$(200 mb)], where $\Delta(\;) = (\bar{\;}) - (\overline{\;\;})$. As shown in Figure 3, the RMS[$\Delta\Psi$(200 mb)] of both the EC and ER experiments are larger in high latitudes. This contrast of RMS[$\Delta\Psi$] between low and high latitudes indicates that both simulations have more interdecadal variability in high latitudes. Additionally, a predominant wave-3 pattern appears at high latitudes on both RMS charts, although the RMS[$\Delta\Psi$(200 mb)] spatial distributions of the two experiments differ. The effect of adding SST anomalies to the EC experiment (to establish the ER experiment) can be revealed by the contrast of RMS[$\Delta\Psi$(200 mb)] between these two experiments. The RMS[$\Delta\Psi$(200 mb)] values of the ER experiment are larger than

(a) RMS[$\Delta\tilde{\psi}$(200mb)] EC

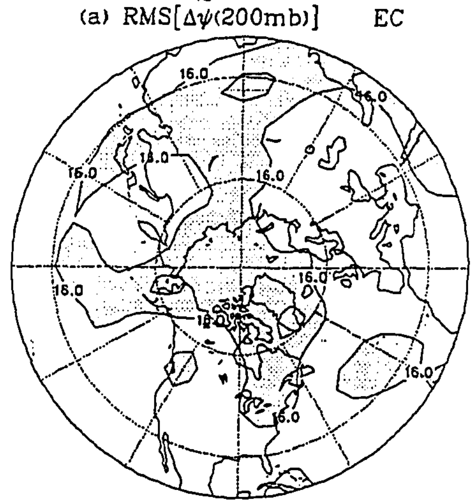

(b) RMS[$\Delta\tilde{\psi}$(200mb)] ER

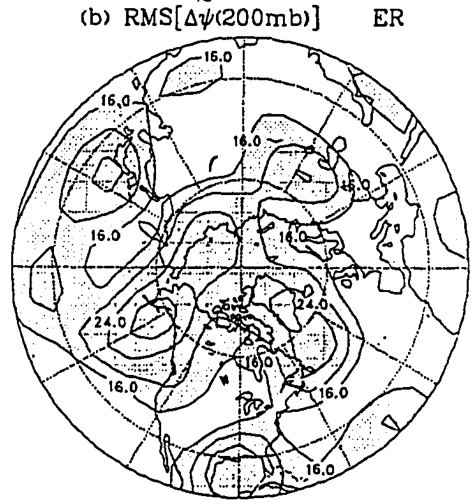

Figure 3. The root-mean-square (RMS) of winter $\tilde{\psi}$(200 mb) for the (a) EC and (b) ER experiments. The contour interval is 4×10^5 m^2s^{-1}. The RMS values between 1.6×10^6 m^2s^{-1} and 2×10^6 m^2s^{-1} are lightly shaded, and those greater than 2×10^6 m^2s^{-1} are heavily shaded.

those of the EC experiment. Apparently, the interdecadal change of the ER experiment is stronger. This contrast indicates that the SST anomalies are one possible cause for the interdecadal variability in the model NH winter circulation.

To compare the temporal behavior of the interdecadal circulation variability between the EC and ER experiments, the time series of $\Delta\Psi$(200 mb) at the six maximum RMS[$\Delta\Psi$(200 mb)] centers of each experiment are displayed in Figure 4. The EC and ER $\Delta\Psi$(200 mb) time series in Figure 4 clearly exhibit interdecadal variability in both experiments. However, the comparison between the EC and ER $\Delta\Psi$(200 mb) time series reveals three major differences. *First*, the amplitude of the fluctuation in the ER $\Delta\Psi$ time series is larger than that in the EC $\Delta\Psi$ time series. *Second*, the low-frequency oscillation in the ER $\Delta\Psi$ field is more well-defined than that in the EC $\Delta\Psi$ field. *Third*, a linearly descending trend over the entire four decades is clear in the ER $\Delta\Psi$ time series, but not in the $\Delta\Psi$ time series of the EC experiment. As mentioned previously, the only difference between the EC and ER experiments is the presence of SST anomalies in the ER case. The contrast between the EC and ER $\Delta\Psi$(200 mb) time series indicates that the SST anomalies can induce systematic changes in the simulated atmospheric circulation. On the other hand, the interdecadal variability in the EC experiment

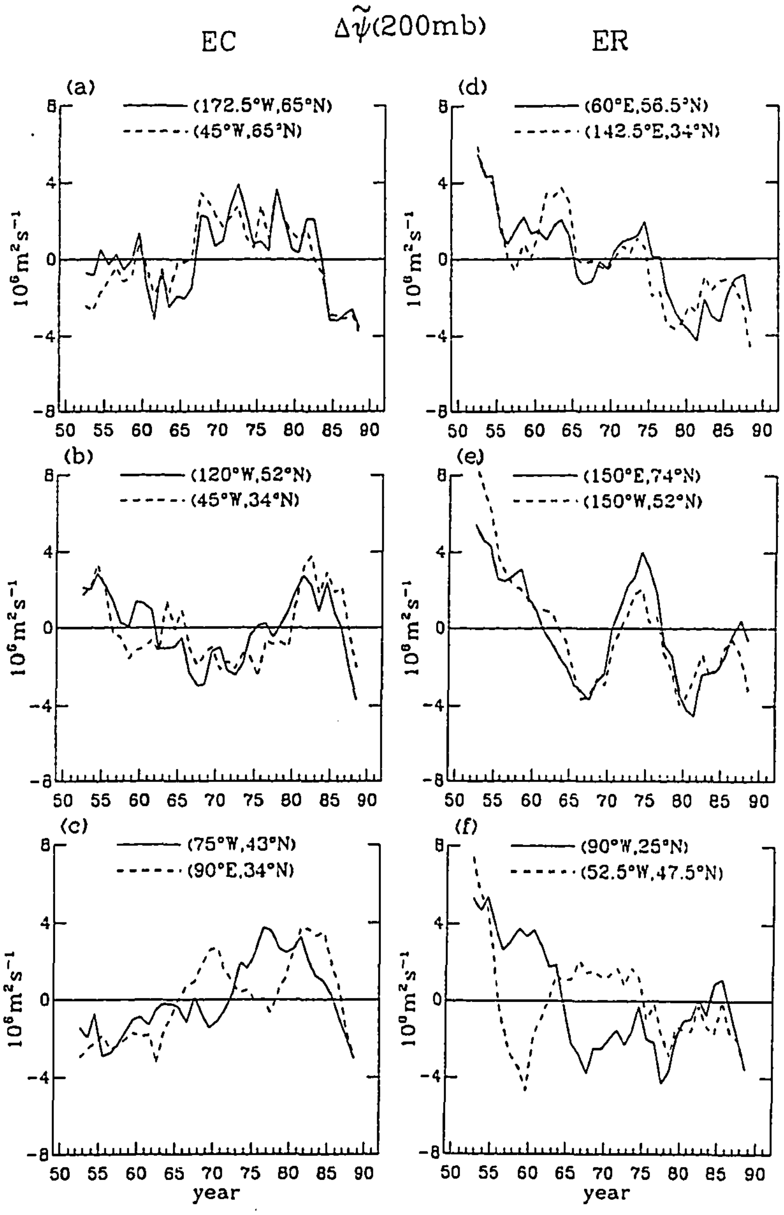

Figure 4. The $\Delta\tilde{\psi}$(200 mb) time series at the maximum RMS[$\Delta\tilde{\psi}$(200 mb)] centers for the EC[(a)-(c)] and ER[(d)-(f)] experiments.

is weaker and without a common oscillation pattern. In view of the aforementioned contrasts, we shall focus our analysis on the interdecadal variability in the ER experiment.

As revealed from the RMS[Ψ(200 mb)] distribution and the $\Delta\Psi$(200 mb) time series, the spatial and temporal characteristics of the interdecadal circulation variability in the EC and ER experiments differ. In order to analyze the temporal and spatial characteristics of the model interdecadal variability simultaneously, we performed EOF analyses on the model total field. Because the effect of SST anomalies on the interdecadal circulation variability is of primary concern in this study, the EOF analyses were performed on the ER Ψ(200 mb) and Ψ(850 mb) fields.

The first eigencoefficient (C1) timeseries and eigenvectors (E1) of ER Ψ(850 mb) and Ψ(200 mb) are shown in Figures 5a-d. The total variance explained by the first eigenmode is 63% for Ψ(200 mb) and 71% for Ψ(850 mb). These high percentages of explained variance suggested that these first eigenmodes are appropriate for delineating the interdecadal change of the total field. The C1[Ψ(200 mb)] and C1[Ψ(850 mb)] time series exhibit a coherent oscillation: two cycles with approximately 20-year low-frequency variations. As for the spatial structure, both E1[Ψ(200 mb)] and E1[Ψ(850 mb)] are characterized by a pattern of north-south contrast: relatively negative and more zonal circulation in high

Figure 5. The eigencoefficient time series/eigenvectors of the first (a)/(b) Ψ(850 mb), (c)/(d) Ψ(200 mb), and (e)/(f) Ψ_Z(200 mb) eigenmodes from the ER experiment. The contour interval of the eigenvectors is 0.15 and the positive values are shaded. The numbers at the upper right corner of the eigencoefficient plots indicate the percentages of the total variance explained by that mode.

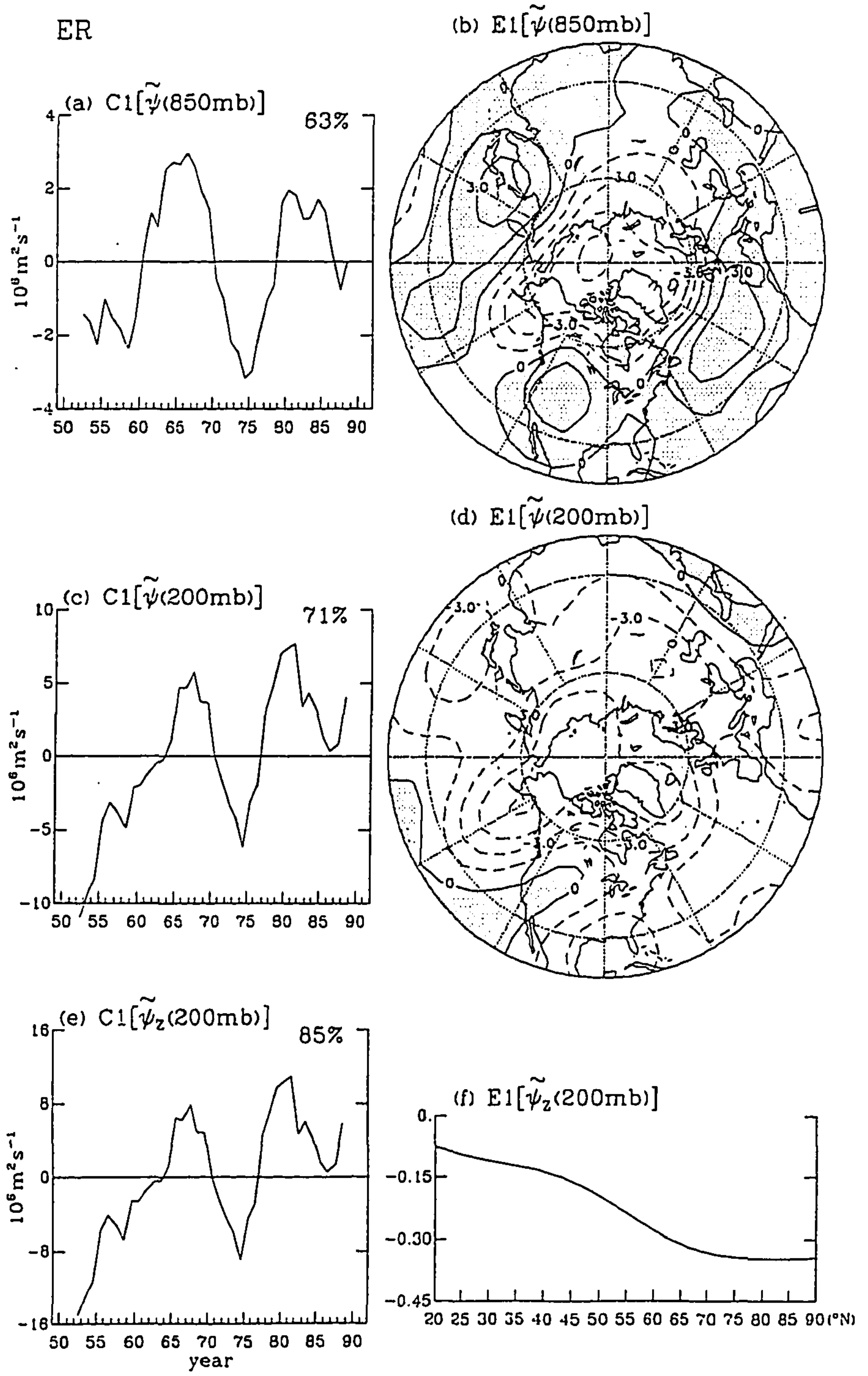
ER
(a) C1[$\tilde{\psi}$(850mb)]
63%
(b) E1[$\tilde{\psi}$(850mb)]
(c) C1[$\tilde{\psi}$(200mb)]
71%
(d) E1[$\tilde{\psi}$(200mb)]
(e) C1[$\tilde{\psi}_z$(200mb)]
85%
(f) E1[$\tilde{\psi}_z$(200mb)]
$10^6 m^2 s^{-1}$
year
20 25 30 35 40 45 50 55 60 65 70 75 80 85 90(°N)

latitudes and relatively positive and more wavier circulation in low latitudes. In high latitudes, both the E1[Ψ(200 mb)] and E1[Ψ(850 mb)] fields exhibit a wave-3 structure. Since the C1[Ψ(200 mb)] and C1[Ψ(850 mb)] series oscillate coherently and the E1[Ψ(200 mb)] and E1[Ψ(850 mb)] resemble each other at high latitudes, the interdecadal change of the ER total field in the high latitudes is regarded as nearly barotropic.

The spatial pattern of the E1[Ψ(200 mb)] field is also similar to that of the ER RMS[$\Delta\Psi$(200 mb)] (Figure 3b), particularly in high latitudes. However, the E1[Ψ(200 mb)] field contains a more zonal structure in high latitudes. In addition, the RMS[$\Delta\Psi$(200 mb)] value is much larger in high latitudes than that in low latitudes. The resemblance between the RMS[$\Delta\Psi$(200 mb)] chart and the E1[Ψ(200 mb)] pattern implies that the major contribution to the interdecadal variability of the total field in high latitudes is contained in the zonal-mean flow. In order to verify this implication, the ER 200 mb zonally-averaged Ψ (Ψ_Z) was analyzed with an EOF analysis.

The first eigenmode of Ψ_Z(200 mb) (Figure 5e-f) accounts for 85% of the total variance. The C1[Ψ_Z(200 mb)] time series has a coherent oscillation with the C1[Ψ(200 mb)] series. The E1[Ψ_Z(200 mb)] pattern reveals that the interdecadal variation of zonal-mean flow is most significant north of

60^oN and becomes weaker as the location shifts southward. This result supports the previous conclusion that the major contribution to the interdecadal circulation variability in high latitudes is from the zonal-mean flow. On the other hand, the smaller value of $E1[\psi_2(200\ mb)]$ in the mid- and low- latitudes implies that the interdecadal variability at these latitudes mainly results from the variation of stationary eddies.

As shown by Burnett (1993) and Chen and Chen (1994), an alternative way of studying the interdecadal circulation variability is to examine the size variation of circumpolar vortices. We thus ask: what is the effect exerted by SST changes on the interdecadal variation of the circumpolar vortex? To answer this question, changes in the circumpolar vortex size for both the EC and ER experiments were compared. For the 200 mb circulation, the circumpolar vortex size is defined as the area poleward of the $\psi(-10^8\ m^2s^{-1})$ contour. This contour is selected because its climatology overlaps with the $RMS[\Delta\psi(200\ mb)]$ centers south of Alaska and Greenland. The diagnostic scheme for estimating the circumpolar vortex size is discussed by Burnett (1993).

Shown in Figures 6a and 6b are the vortex size time series (solid line) and its decadal trend (dashed line) derived from a least-square-fit analysis of the EC and ER simulations, respectively. The trends in the vortex size time

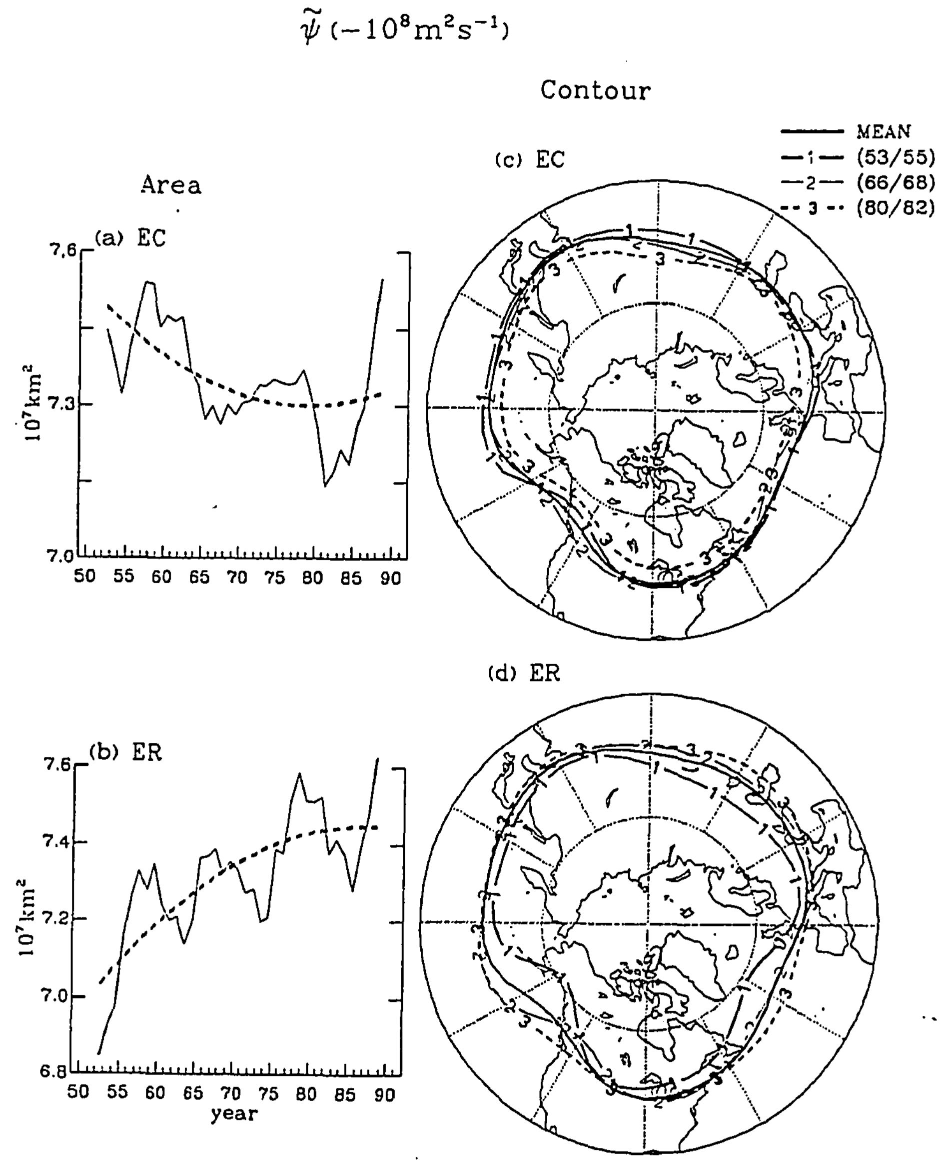

Figure 6. The time series of total circumpolar vortex area poleward of $\bar{\psi}(-10^8\ m^2s^{-1})$ contour (solid line) and its corresponding decadal trend (dashed line) for the (a) EC and (b) ER experiments. Also shown is the horizontal distribution of the circumpolar vortex lines from three different phases along with the multi-winter mean vortex line for the (c) EC and (d) ER experiments. The horizontal charts are plotted from the 30 °N poleward.

series exhibit a clear contrast: the EC circumpolar vortex tends to contract, while the ER vortex tends to expand. This contrast reveals that the interdecadal SST anomalies induce the expansion of the circumpolar vortex.

As pointed out by Burnett (1993), the vortex expansion interpreted from the increase in total vortex area does not indicate whether this expansion is characteristic of all parts of the vortex. In order to illustrate the horizontal variability of the circumpolar vortex, the $\Psi(-10^8\ m^2s^{-1})$ contours in the early (1953-55), middle (1966-68), and late (1980-82) stages of the simulation are plotted along with the climatology, i.e., $\overline{\Psi}(-10^8\ m^2s^{-1})$. To make the interdecadal variability of the circumpolar vortex more discernible, the displacement between the contours of different phases and that of the climatology has been enlarged by a factor of three.

In the EC case (Figure 6c), the contours at the early- and late-stages demonstrate that the vortex contraction takes place over the entire hemisphere. On the other hand, the vortex expansion in the ER experiment also seems to occur hemispherically (Figure 6d). The high zonality of the circumpolar vortex variability is consistent with the previous result that the interdecadal variability in high latitudes mainly results from the change of the zonal-mean flows.

In the ER experiment, major expansions of the circumpolar vortex occur in three locations: the North Pacific south of Alaska, the North Atlantic south of Greenland, and the central Russia. A comparison between Figures 6d and 1a reveals that the locations of the three major expansions in the circumpolar vortex are in the vicinity of the three climatological troughs. In other words, the major equatorward expansions of the circumpolar vortex are associated with the deepening of the three climatological troughs. In addition, locations of the major expansions of the circumpolar vortex also coincide with centers of RMS[$\Delta\Psi$(200 mb)] (Figure 3b) and of E1[Ψ(200 mb)] (Figure 5d). This spatial coherence implies that, in high latitudes, the major dynamic process responsible for the interdecadal variability in the ER experiment is the expansion of the circumpolar vortex. This expansion of the circumpolar vortex is apparently induced by the interdecadal SST anomalies.

The interdecadal variation of the circumpolar vortex at 850 mb is analyzed with the same procedures as that for 200 mb. The $\Psi(-3\times10^{6}\ m^{2}s^{-1})$ contour is selected in this case. The 850 mb vortex size time series (Figures 7a,b) show a similar result as their 200 mb counterparts: an expansion trend of circumpolar vortex in the ER simulation, and a contraction trend in the EC experiment. The horizonal variability of the circumpolar vortex from the early- to late-period of the

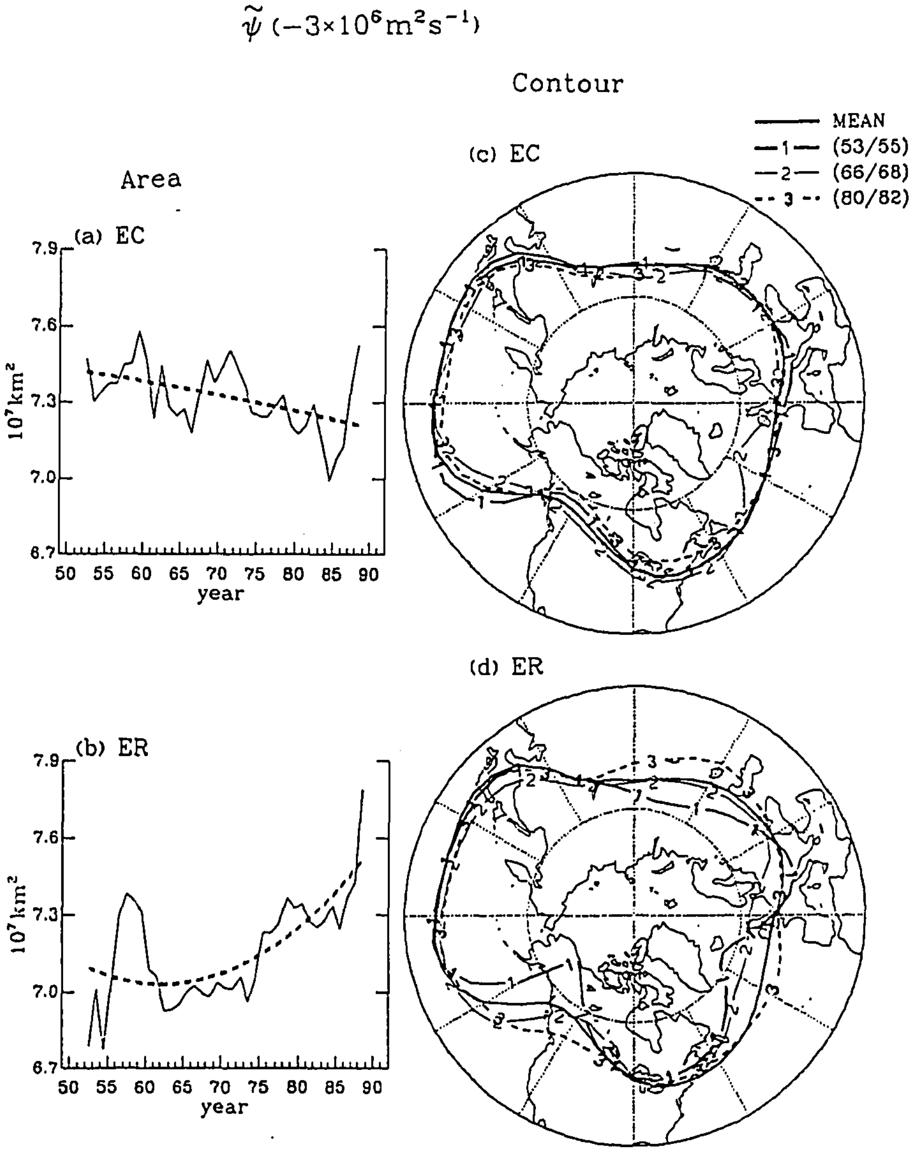

Figure 7. As in Figure 6, except for the $\Psi(-3\times10^{6}\ m^2s^{-1})$ contour at 850 mb.

model simulation is relatively zonal in both the EC (Figure 7c) and ER (Figure 7d) experiments. In the ER experiment, the vortex expansion at 850 mb is most significant at the same three locations as those found in the analysis of the 200 mb circumpolar vortex. The aforementioned results demonstrate clearly that the interdecadal variability of the circumpolar vortex at 200 mb and 850 mb are similar in many aspects. To some extent, this similarity reflects the nearly barotropic nature of the interdecadal circulation variability at high latitudes.

In this section, the analysis of the interdecadal variation of the total field revealed that the interdecadal SST anomalies can induce: (1) the equatorward expansion of the total circumpolar vortex, and (2) the deepening of the three climatological troughs. These results partially answer the first question raised in the Introduction. The analysis also reveals that the interdecadal variation of the total field is dominated by the zonal-mean flow, particularly over the high latitudes. In other words, the interdecadal variation of stationary eddies, to some degree, is obscured by that of zonal-mean flows in the analysis of the interdecadal total field variability. Therefore, we should specifically examine the interdecadal variability of stationary eddies.

3. Decadal variation of stationary eddies

Recently, Chen and Chen (1994) identified two different interdecadal modes from the observed stationary eddy field: Pacific and Atlantic modes. In view of Chen and Chen's result, we analyzed the interdecadal variability of model simulated stationary eddies, focusing on the identification of possible interdecadal variation modes.

In order to identify the interdecadal modes of model stationary eddies, the following diagnostic analyses have been performed.

(1) The spatial pattern of the interdecadal change of stationary eddies may be inferred from the horizontal distribution of $\Delta\Psi_E$(200 mb) variance. The RMS of Ψ_E(200 mb) was thus computed first.

(2) The $\Delta\Psi_E$(200 mb) time series at the RMS[$\Delta\Psi_E$(200 mb)] centers were used to illustrate the temporal properties of the interdecadal modes.

(3) To identify the spatial structure of the interdecadal modes, the pattern analysis of correlation coefficients between the NH Ψ_E(200 mb) field and the previously selected $\Delta\Psi_E$(200 mb) time series was conducted.

(4) In order to verify the interdecadal variation modes inferred from the time series and correlation coefficient analyses, an EOF analysis of Ψ_E(200 mb) was performed separately with the domains containing the Northern

Hemisphere, Pacific/North America, and Atlantic/Europe regions.

The results of the aforementioned four analyses are presented and discussed in the remainder of this section.

Shown in Figure 8 are the RMS[$\Delta\Psi_E$(200 mb)] field for the EC and ER experiments. The RMS[$\Delta\Psi_E$(200 mb)] values of both experiments are larger (smaller) to the north (south) of 60°N. In Figure 8a, the EC RMS centers in the North America/North Atlantic sector seem to overlap with the climatological troughs and ridges (see Figure 1c). This coincidence implies that the interdecadal variability of EC stationary eddies results from the intensification or weakening of stationary ridges and troughs. On the other hand, in Figure 8b the ER RMS centers over the PNA and NA regions are located in quadrature with mean stationary eddies shown in Figure 1c. This spatial quadrature relationship between the distributions of the ER RMS centers and the mean stationary eddies indicates that the interdecadal variability of stationary eddies induced by the SST anomalies is spatially in quadrature with the climatological stationary eddies.

It is also interesting to compare the horizontal distributions of RMS[$\Delta\Psi_E$(200 mb)] and RMS[$\Delta\Psi$(200 mb)] (Figure 3). In both experiments, the amplitude of RMS[$\Delta\Psi$(200 mb)] is larger overall than that of RMS[$\Delta\Psi_E$(200 mb)], particularly

(a) RMS[$\Delta\tilde{\psi}_E$(200mb)] EC

(b) RMS[$\Delta\tilde{\psi}_E$(200mb)] ER

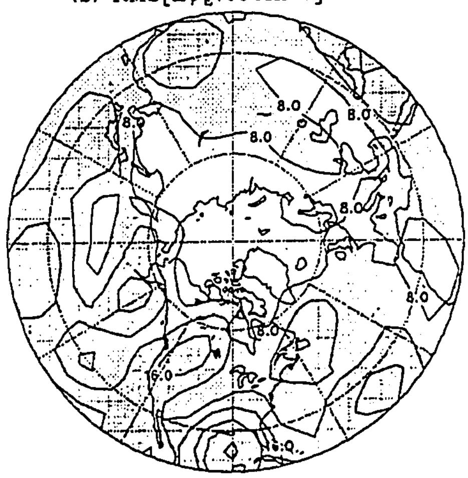

Figure 8. As in Figure 3, except for the 200 mb eddy streamfunction.

over the area north of 60°N. The aforementioned contrast between the amplitudes of RMS[$\Delta\Psi$(200 mb)] and RMS[$\Delta\Psi_E$(200 mb)] implies that the major contribution to the interdecadal variability of the model circulation over the polar region is due to zonal mean flows. On the other hand, the maximum RMS centers of the $\Delta\Psi$(200 mb) and $\Delta\Psi_E$(200 mb) fields to the south of 60°N are more or less coincident. This spatial agreement suggests that the contribution of the interdecadal variability of stationary eddies to the total interdecadal circulation change is important over the area south of 60°N.

To portray the temporal characteristics of the interdecadal variability of the stationary eddies, the $\Delta\Psi_E$(200 mb) time series at the EC and ER RMS centers are displayed in Figure 9. For the EC case, the variation of the $\Delta\Psi_E$ time series in Figure 9a is similar to its $\Delta\Psi$ counterparts in Figure 4b. In Figure 9b, the $\Delta\Psi_E$ time series from the downstream sector of the East Asian trough (solid line) and the North American trough (dashed line) oscillate coherently. These troughs deepened during the first two decades but filled in the 1970s and the early 1980s. In Figure 9c, the $\Delta\Psi_E$ time series located at the ridges off the southeast coast of the United States (solid line) and off the west coast of Europe (dashed line) change toward weaker intensity. The aforementioned variability of the ridges and troughs indicates that the stationary eddies become

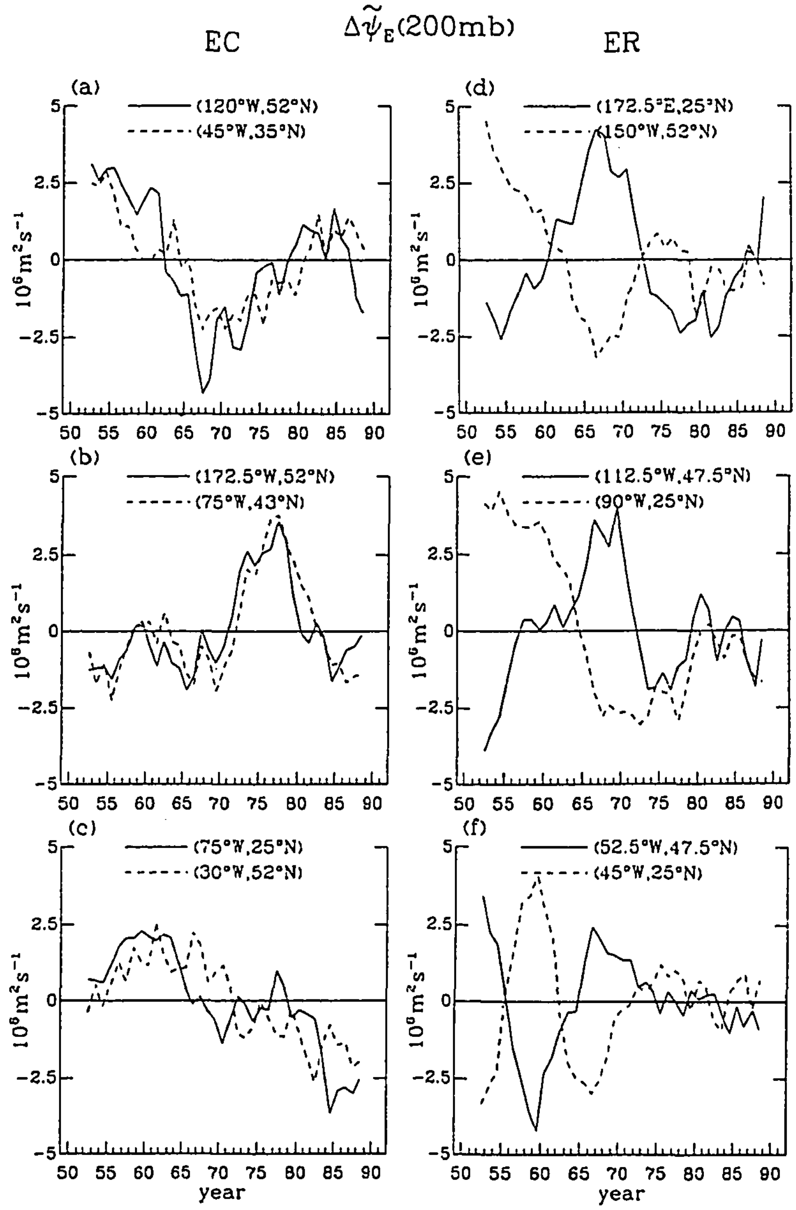

Figure 9. As in Figure 4, except for the 200 mb eddy streamfunction.

progressively more undersimulated as the EC integration proceeds.

For the ER case, The $\Delta\Psi_E$ time series at the RMS centers over the North Pacific and North America are illustrated in Figures 9d and 9e, respectively. These $\Delta\Psi_E$ time series, from consecutive RMS cells, oscillate consistently but oppositely in phase before the mid-1970s. After the mid-1970s, these $\Delta\Psi_E$ time series oscillate with a weaker amplitude and an irregular phase relationship. In the NA area, a north-south seesaw oscillation in the stationary eddies is evident from the $\Delta\Psi_E$ time series shown in Figure 9f. The oscillation is pronounced before the mid-1970s and nearly vanishes afterward. In addition, the NA $\Delta\Psi_E$ time series show an oscillation different from that which exists in the North Pacific and North America region.

The above $\Delta\Psi_E$(200 mb) time series analysis indicates that the interdecadal variability of stationary eddies in the EC experiment resulted from the undersimulation of model stationary eddies. The undersimulation of stationary eddies in the EC experiment is related to the NCAR CCM1's systematic error. On the other hand, the SST anomalies induce different types of temporal variations in the stationary eddies over the PNA and NA regions. This result implies the possible existence of two different interdecadal variation modes in the ER experiment. Hereafter, we shall focus on the identification of the interdecadal modes in the ER experiment.

In addition to the temporal characteristics, the spatial structure is another factor that can be used in the identification of interdecadal variation modes. To illustrate the spatial structure of the PNA interdecadal regime, the correlation coefficient pattern between the ER $\Delta\Psi_E$(200 mb) field and the $\Delta\Psi_E$(200 mb) time series at the RMS center over western North America is computed. This correlation pattern (Figure 10a; hereafter referred to as the PNA correlation pattern) exhibits a teleconnection pattern emanating from the subtropical Pacific east of the Date line, propagating through the Gulf of Alaska, North America, and turning back to near the southeast United States. The correlation coefficient pattern between the $\Delta\Psi_E$(200 mb) time series at the RMS center over Newfoundland and the $\Delta\Psi_E$(200 mb) field is used to depict the interdecadal NA regime. This correlation pattern (Figure 10b; hereafter referred to as the NA correlation pattern) contains a north-south triple-cell structure centered at Greenland, Newfoundland, and the central subtropical North Atlantic. Correlation maps obtained by the $\Delta\Psi_E$(200 mb) indices at other PNA RMS centers (not shown) display a structure similar to the PNA correlation pattern shown in Figure 10a. A NA correlation pattern with a spatial structure opposite to that shown in Figure 10b is

ER $\tilde{\psi}_E$(200mb) Auto-correlation

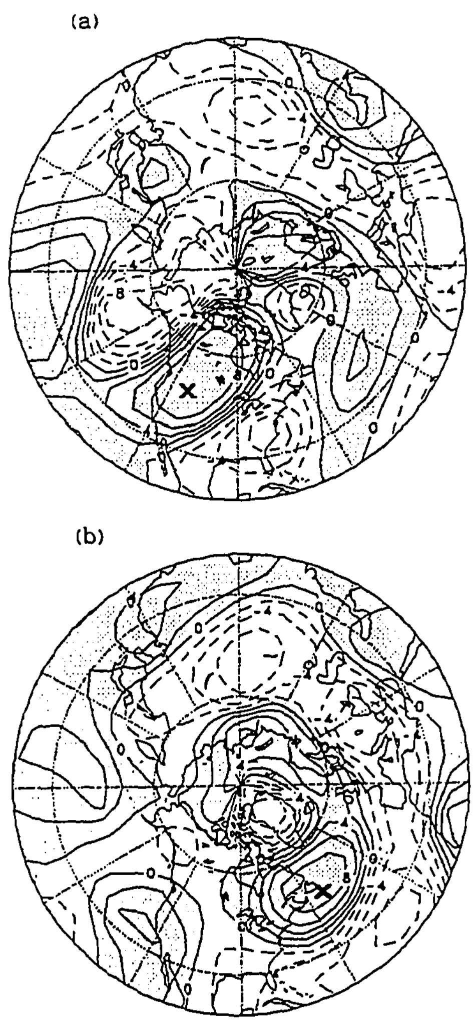

Figure 10. The correlation coefficient patterns between the time series of $\Delta\Psi_E$(200 mb) at each grid points and the $\Delta\Psi_E$(200 mb) time series at the RMS[$\Delta\Psi_E$(200 mb)] center (marked by X) in the (a) PNA and (b) NA regions. The contour is 0.2 and positive values are shaded.

obtained with the Ψ_E(200 mb) index at the other NA RMS center.

The above $\Delta\Psi_E$(200 mb) time series and correlation pattern analyses imply the existence of two independent interdecadal modes over the PNA and NA regions; namely, the PNA and NA modes. The temporal properties of these two modes can be inferred from the corresponding time series in Figure 9. The spatial structures of these two modes are then illustrated by the correlation maps in Figure 10.

In order to verify the existence of the PNA and NA modes, we performed an EOF analysis of the Ψ_E(200 mb) field with the domain of the northern hemisphere. Shown in Figure 11 are the first three eigencoefficient (denoted as C1, C2, and C3, respectively) timeseries and eigenvectors (denoted as E1, E2, and E3, respectively). These three modes account for 30%, 23%, and 15% of the total variance. The C1[Ψ_E(200 mb)] time series varies synchronously with the PNA $\Delta\Psi_E$(200 mb) indices in Figures 9d and 9e, and the E1[Ψ_E(200 mb)] field resembles the PNA correlation pattern in Figure 10a. Undoubtedly, The PNA mode revealed from the PNA correlation pattern is primarily represented by the first eigenmode of Ψ_E(200 mb).

For the second eigenmode, the C2[Ψ_E(200 mb)] series contains a positive phase before the 1970s and a negative phase afterward. The temporal variation of C2[Ψ_E(200 mb)] does not match either the PNA or NA $\Delta\Psi_E$(200 mb) indices in

Figure 11. The eigencoefficient time series/eigenvectors for the ER (a)/(b) first, (c)/(d) second, and (e)/(f) third Ψ_E(200 mb) eigenmodes with the domain poleward of 20 ^{o}N. The contour interval is 0.15 and the positive values are shaded.

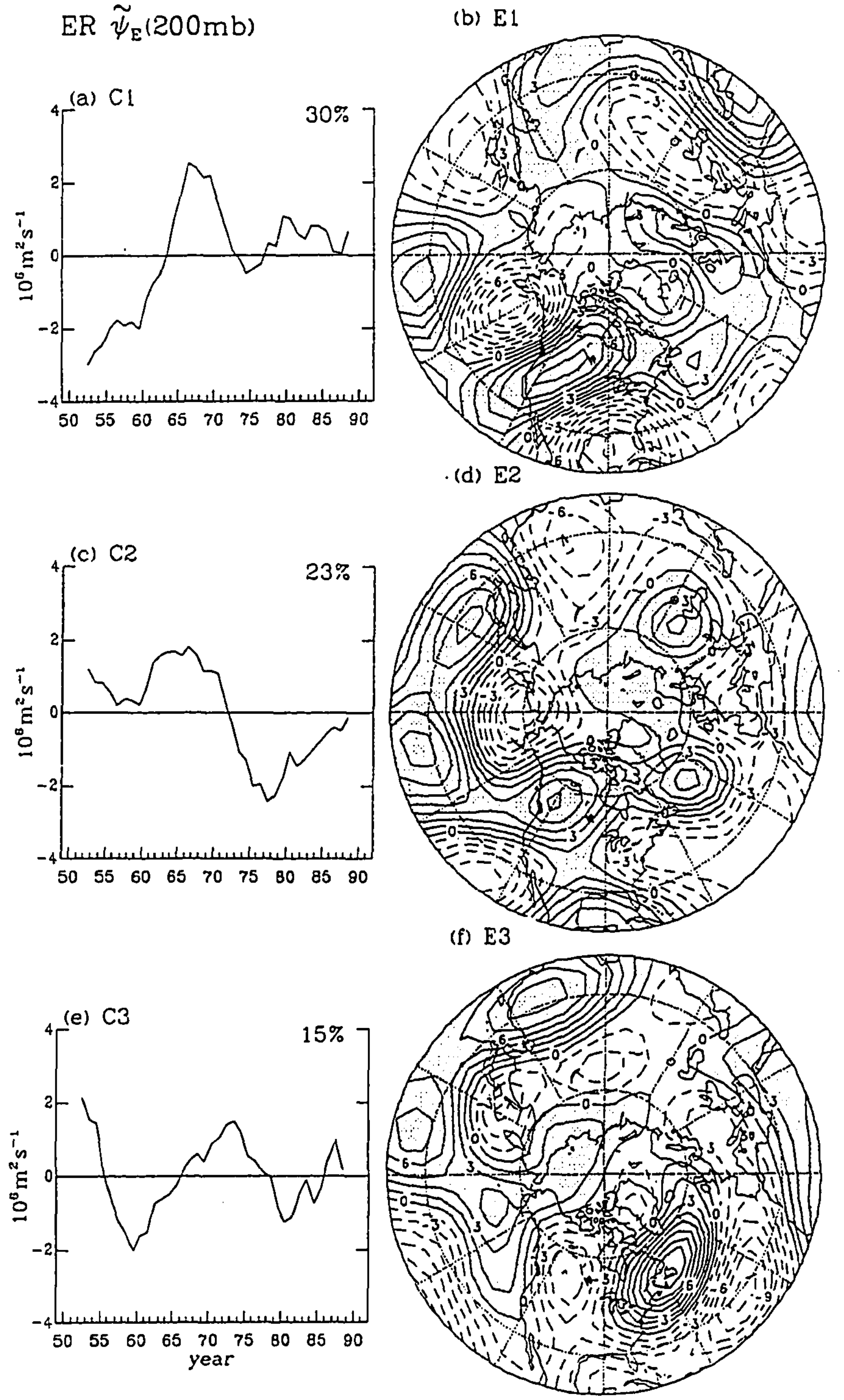
ER $\widetilde{\psi}_E$(200mb)
(a) C1
30%
(b) E1
(c) C2
23%
(d) E2
(e) C3
15%
(f) E3
$10^6 m^2 s^{-1}$
50 55 60 65 70 75 80 85 90
year

Figure 9. The salient feature of E2[Ψ_E(200 mb)] is the teleconnection pattern over the North Pacific region. This teleconnection pattern exhibits centers over the sea east of Japan, the Bering Sea, western Canada, and the subtropical eastern Pacific. This pattern seems to emerge from the western Pacific. Obviously, The E2[Ψ_E(200 mb)] field exhibits a spatial structure different from the PNA and NA correlation patterns in Figure 10. The existence of the second Ψ_E(200 mb) eigenmode indicates the existence of a third interdecadal mode in addition to the PNA and NA modes.

For the third eigenmode, the C3[Ψ_E(200 mb)] series oscillates coherently with the NA $\Delta\Psi_E$(200 mb) index (Figure 9f) only before the mid-1960s. After the mid-1960s, the phases of C3[Ψ_E(200 mb)] and the NA $\Delta\Psi_E$(200 mb) index become inconsistent. As for the spatial structure, the E3[Ψ_E(200 mb)] field exhibits a north-south triple-cell structure over the Greenland/North Atlantic region which is similar to the salient feature of the NA correlation pattern (Figure 10b). The aforementioned results indicate that the third Ψ_E(200 mb) eigenmode bears some similarity to the NA mode revealed from the NA correlation pattern, but does not truly represent the NA mode due to the inconsistency in the temporal variation.

The EOF analysis of NH Ψ_E(200 mb) can identify the PNA mode but not the NA mode. It is likely that the signal of the NA mode mixes with the signals of other modes and can not be clearly isolated by the EOF analysis. In order to circumvent this difficulty, we shall adjust the spatial domain of the EOF analysis to the region within which the NA mode dominates. Based upon this approach, the NA mode should be better isolated if the PNA area is not included in the EOF analysis, and vice versa. As revealed by the PNA and NA correlation patterns in Figure 10, the salient features of the PNA and NA modes are located within the domains of 120°E-60°W and 90°W-30°E, respectively. We thus shall conduct the EOF analyses of Ψ_E(200 mb) separately over the aforementioned two domains to isolate the PNA and NA modes. In addition to the PNA and NA modes, the third interdecadal mode (Figure 11d) also has its salient feature in the PNA region. Thus the characteristics of the third interdecadal mode should be more clearly depicted by the EOF analysis of Ψ_E(200 mb) with only the PNA domain. In this regard, we used the EOF analysis of the PNA region Ψ_E(200 mb) to examine the PNA and the third interdecadal mode. Therefore, the first two eigenmodes of PNA region Ψ_E(200 mb) and the first eigenmode of NA region Ψ_E(200 mb) are displayed in Figure 12 for discussion.

The first two Ψ_E(200 mb) eigenmodes from the PNA domain explain 39% and 25% of the total variance. The temporal variation of PNA region C1[Ψ_E(200 mb)] series (Figure 12a) is consistent with that of the PNA $\Delta\Psi_E$(200 mb) indices (Figures 9d-e). There is also a resemblance between the spatial

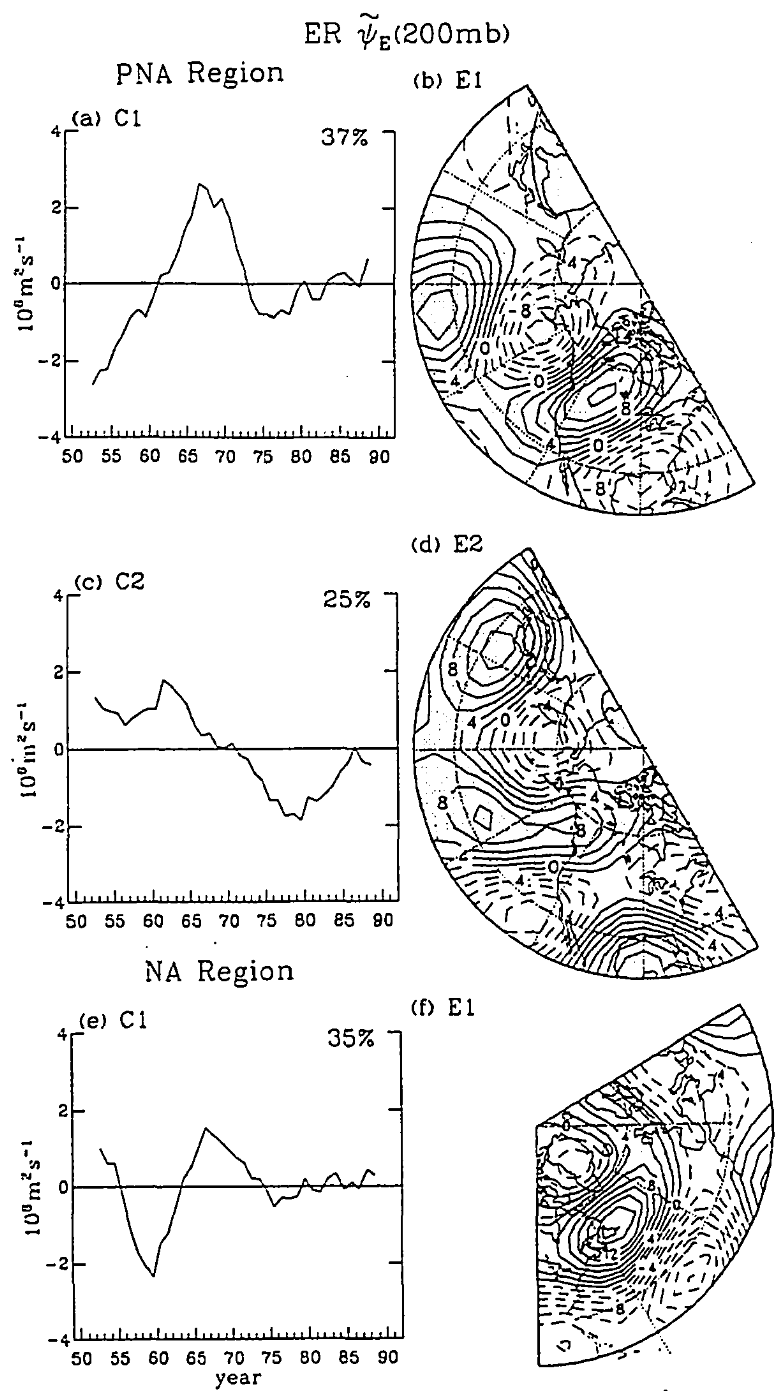

Figure 12. As in Figure 11, except for the first two Ψ_E(200 mb) eigenmodes with only the PNA domain (a-d) and the first Ψ_E(200 mb) eigenmode with only the NA domain (e-f). The contour interval of the eigenvectors is 0.2.

structure of the PNA region E1[Ψ_E(200 mb)] mode (Figure 12b) and the PNA correlation pattern (Figure 10b). The aforementioned results reveal clearly that the first eigenmode of the PNA region Ψ_E(200 mb) field represents the PNA mode previously identified.

The PNA region C2[Ψ_E(200 mb)] series (Figure 12c) exhibits a significant descending trend during the 1960s and 1970s and an ascending trend after 1980. The spatial structure of PNA region E2[Ψ_E(200 mb)] mode (Figure 12d) features a teleconnection pattern with the centers over the ocean east of Japan, the Bering Sea, south of the Gulf of Alaska, and west of Mexico. Since the second eigenmode of the PNA region Ψ_E(200 mb) field emanates from the western Pacific, we hereafter refer to this mode as the PNA west (PNAW) mode. Both the temporal and spatial characteristics of the PNAW mode bear some similarity with the second eigenmode of the NH Ψ_E(200 mb) field shown in Figure 11.

The first eigenmode of the NA region Ψ_E(200 mb) field explains 36% of the total variance. The NA region C1[Ψ_E(200 mb)] series (Figure 12e) oscillates coherently with the NA $\Delta\Psi_E$(200 mb) indices (Figure 9f). The NA region E1[Ψ_E(200 mb)] mode (Figure 12f) exhibits a north-south triple-cell structure along 45°W which resembles the salient feature of the NA correlation pattern (Figure 10b). Apparently, the first eigenmode of the NA region Ψ_E(200 mb) field represents the NA mode identified before.

The regional Ψ_E(200 mb) EOF analyses verify the existence of the PNA and NA modes which were revealed from the $\Delta\Psi_E$(200 mb) time series and correlation patterns. Moreover, a third interdecadal mode, i.e., PNAW mode, is shown in the EOF analysis of the PNA region Ψ_E(200 mb). Up to this point, the vertical structure of these interdecadal modes has not been examined. It was pointed out by Chen and Chen (1994) that the vertical structure of the observed interdecadal mode is nearly barotropic. In order to investigate the vertical structure of the model interdecadal modes, the EOF analyses of PNA region Ψ_E(850 mb) and NA region Ψ_E(850 mb) were performed and compared with their 200 mb counterparts. The results of the regional Ψ_E(850 mb) EOF analyses are illustrated in Figure 13.

The total variance explained by the second and third eigenmodes of the PNA region Ψ_E(850 mb) is 25% and 21%, respectively, while that explained by the first eigenmode of the NA region Ψ_E(850 mb) is 47%. The first eigenmode of the PNA region Ψ_E(850 mb) is not shown in Figure 13. This is because we can use the second and third eigenmodes of the PNA region Ψ_E(850 mb) to examine the vertical structure of the model interdecadal modes. Comparison between Figures 12 and 13 reveals that: (1) the temporal and spatial characteristics of the second (third) eigenmode of the PNA region Ψ_E(850 mb)

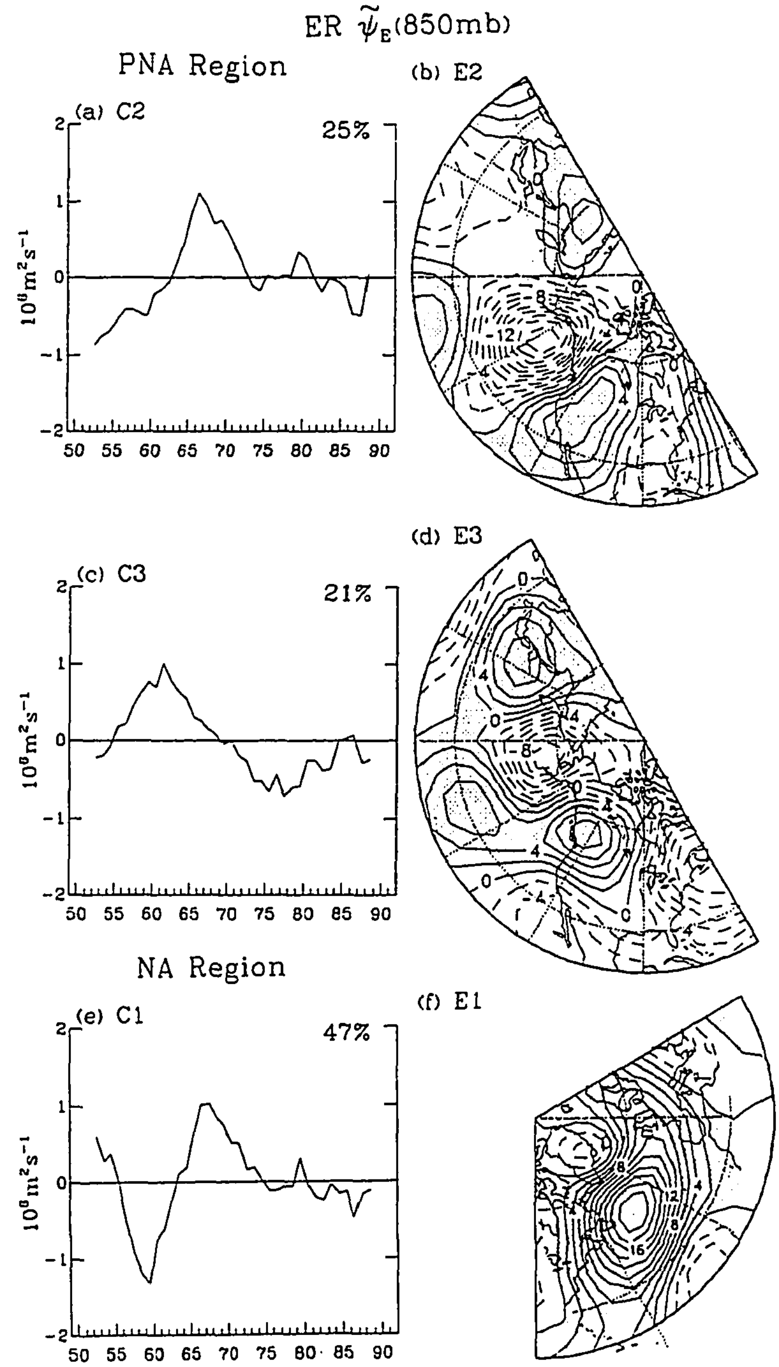

Figure 13. As in Figure 12, except for the Ψ_E(850 mb)

are in close agreement with the first (second) eigenmode of the PNA region Ψ_E(200 mb), and (2) the first eigenmodes of the NA region Ψ_E(850 mb) and Ψ_E(200 mb) exhibit similar temporal variations and spatial structures. Thus, the comparison between 200 mb and 850 mb EOFs clearly indicates that the model PNA, PNAW, and NA modes are all nearly barotropic.

In this section, the analysis of the interdecadal change of stationary eddies revealed that the interdecadal SST anomalies can induce three interdecadal modes in the stationary eddies: PNA, PNAW, and NA modes. This result can then be used to answer the first question mentioned in the Introduction. To answer the second question raised in the Introduction, the temporal and spatial characteristics of the PNA, PNAW, and NA modes are summarized as follows. The temporal variation of all three interdecadal modes primarily consists of a decadal trend plus low-frequency oscillations with periods of about 15~20 years. As for spatial structure, the PNA and PNAW modes exhibit a teleconnection pattern over the PNA region, while the NA mode possesses a north-south three-cell structure over the Greenland/North Atlantic area. Vertically, the PNA, PNAW, and NA modes are all equivalent barotropic.

It is also interesting to compare the EOFs from the Ψ(200 mb) and Ψ_E(200 mb) fields. The comparison between the first eigenmodes of Ψ(200 mb) (Figures 5c-d) and Ψ_E(200 mb) (Figures 11a-b) reveals the following results. (1) The C1[Ψ(200 mb)] series oscillates coherently with C1[Ψ_E(200 mb)], although the former has a more significant increasing trend than the latter. (2) The relative negative (positive) centers of E1[Ψ(200 mb)] coincide with the negative (positive) centers of E1[Ψ_E(200 mb)]. Over the regions south of Alaska, Greenland, and central Russia, the major expansions of the circumpolar vortex shown in E1(Ψ(200 mb)] are associated with the deepening of the stationary troughs shown in E1[Ψ_E(200 mb)]. (3) The teleconnection pattern of the interdecadal mode (i.e., PNA mode in this case) is more discernible in the stationary eddy field than in the total field. Thus, it is advantageous to use the stationary eddy field to identify the interdecadal modes which have the teleconnection pattern.

Another interesting result shown in this section is that the PNA and PNAW modes are the two most important modes in the interdecadal variation of stationary eddies at 200 mb, but become the second and third most important at 850 mb, respectively. This result may be due to the decrease in the intensity of the PNA-like teleconnection pattern from the upper- to lower-troposphere (Wallace and Gultzer 1981). It was demonstrated from the numerical studies that the PNA-like teleconnection pattern results from the response of the atmospheric circulation to the tropical heating (e.g., Hoskins and Karoly 1981 ; Simmons 1982). Therefore, the cause of the PNA and PNAW modes is possibly related to the change in tropical diabatic heating over the Pacific.

4. The possible effect of tropical heating on the stationary eddies

In the previous section, the analysis of the interdecadal variation of the stationary eddies revealed that the model atmospheric circulation responds to the SST anomalies and exhibits three interdecadal variation modes. However, it is not clear what atmospheric processes are involved in maintaining these modes. As discussed previously, the SST anomalies result in the variability of the tropical heating. In turn, the tropical heating anomalies induce changes in the midlatitude stationary eddies. The importance of the tropical heating anomalies to the interdecadal circulation variability can be inferred from the spatial structure of the model interdecadal variation modes. Both the PNA and PNAW modes exhibit a PNA-like teleconnection pattern which is considered to be the response of the atmospheric circulation to tropical heating (e.g., Hoskins and Karoly 1981). Therefore, we shall study the atmospheric processes involved in maintaining the model interdecadal variation modes by examining the possible effect of tropical heating on the stationary eddies.

The effect of tropical heating on the atmospheric circulation, which can be considered to be a chain event dynamic process, can be delineated by χ-maintenance and ψ-budget analyses (Chen and Yen 1991b). The dynamic processes depicted by the χ-maintenance and ψ-budget analyses are described as follows. The tropical heating maintains the planetary-scale divergent circulation. The divergent circulation interacts with the rotational circulation to generate the streamfunction tendency induced by the vorticity source (ψ_χ) and streamfunction tendency induced by the vorticity advection (ψ_{AV}). Both the ψ_χ and ψ_{AV} fields are spatially in quadrature with the stationary eddies; and the counterbalance of ψ_χ and ψ_{AV} is the primary mechanism for the maintenance/adjustment of the stationary eddies.

In order to illustrate the effect of the tropical heating anomalies on the interdecadal variation of the stationary eddies, the χ-maintenance and ψ-budget analyses were performed to analyze the maintenance of the PNA and PNAW modes. In the χ-maintenance analysis, the diabatic heating is analyzed in terms of the vertically-integrated diabatic heating (H_I) and its potential function ($\chi_H=\nabla^{-2}H_I$). The relationship between the interdecadal changes of the H_I, χ_H, and χ(200 mb) fields is examined by comparing the EOF analyses of $\tilde{H}_I$, $\tilde{\chi}_H$, and $\tilde{\chi}$(200 mb) in the domain (60°E-120°W, 45°S-60°N). Because the major heating source for the PNA-like teleconnection pattern is located within the tropical Pacific (e.g., Simmons et al. 1985; Geisler et al. 1985), the aforementioned domain of the EOF analyses is sufficient to cover the primary heating anomalies for the PNA and PNAW modes.

In the ψ-budget analysis, the ψ_χ(200 mb) and ψ_{AV}(200 mb) fields are computed from the 200 mb winter-averaged winds and vorticities following the formulation of the ψ-budget equation. Since the PNA and PNAW modes are identified from the stationary eddy field, the eddy components of ψ_χ(200 mb) and ψ_{AV}(200 mb), i.e., $\psi_{\chi E}$ and ψ_{AVE}, respectively, are selected in the ψ-budget analysis. To conduct the ψ-budget analysis on the decadal time scale, the EOF analyses of $\tilde{\psi}_{\chi E}$(200 mb) and $\tilde{\psi}_{AVE}$(200 mb) were performed with the same domain as the EOF analysis of the PNA region $\tilde{\psi}_E$(200 mb). The spatial relationship between the eigenmodes of the $\tilde{\psi}_{\chi E}$(200 mb), $\tilde{\psi}_{AVE}$(200 mb), and $\tilde{\psi}_E$(200 mb) fields will be considered in order to demonstrate the adjustment processes for the interdecadal variation of the rotational circulation. The results of the EOF analyses associated with the χ-maintenance and ψ-budget analyses are discussed in the following paragraph.

Shown in Figure 14 are the first $\tilde{H}_I$, second $\tilde{\chi}_H$, and second $\tilde{\chi}$(200 mb) eigenmodes. The total variance explained by the first $\tilde{H}_I$ eigenmode is 26% and that accounted for by the second eigenmodes of $\tilde{\chi}_H$ and $\tilde{\chi}$(200 mb) is 29% and 32%,

Figure 14. The EOF analyses associated with the χ-maintenance analysis of the PNA mode. The eigencoefficients/eigenvectors of the (a)/(b) first $\tilde{H}_I$, (c)/(d) second $\tilde{\chi}_H$, and (e)/(f) second $\tilde{\chi}$(200 mb) eigenmodes. The contour interval is 0.5 for E1[$\tilde{H}_I$] and 0.2 for E2[$\tilde{\chi}_H$] and E2[$\tilde{\chi}$(200 mb]. The E1[$\tilde{H}_I$] values larger (smaller) than 0.5 (-0.5) are heavily (lightly) shaded. The positive values of E2[$\tilde{\chi}_H$] and E2[$\tilde{\chi}$(200 mb)] are shaded.

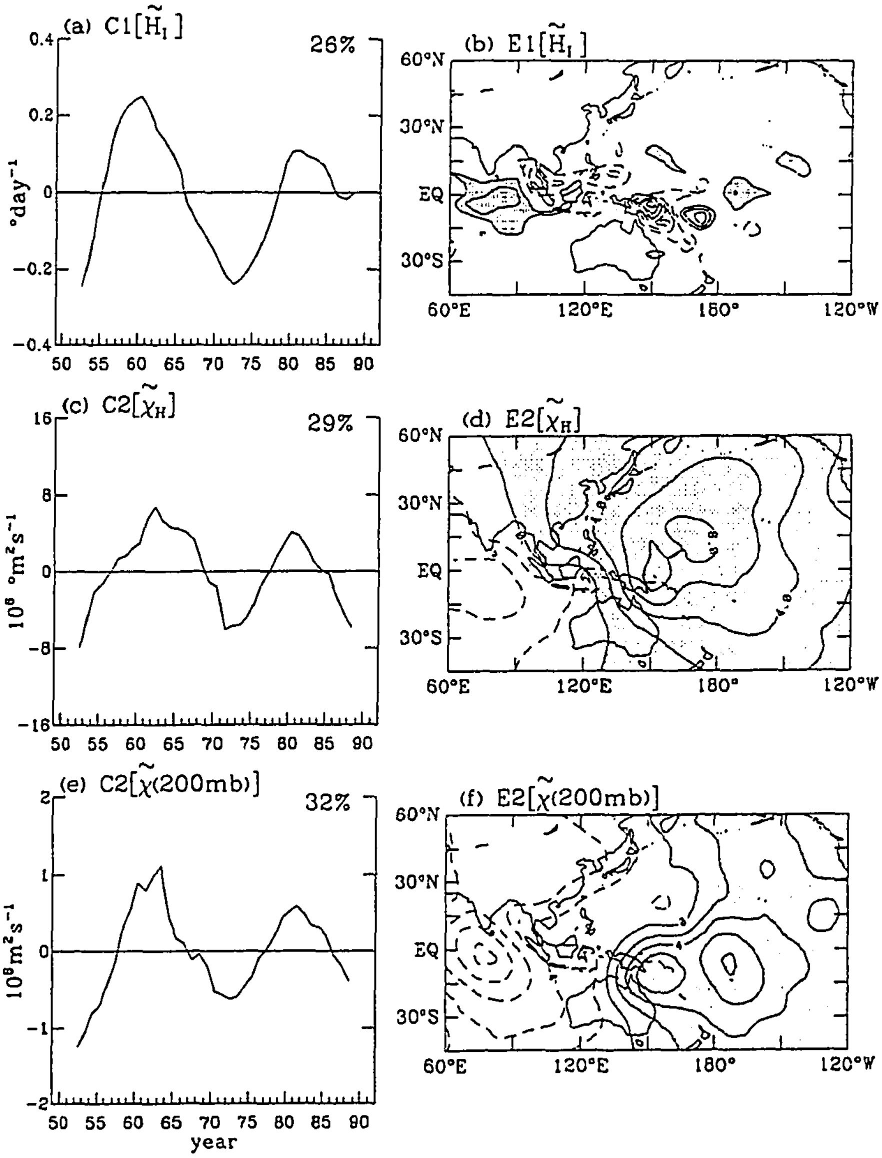

(a) C1[$\tilde{H}_I$]
26%
°day^{-1}
(b) E1[$\tilde{H}_I$]
(c) C2[$\tilde{\chi}_H$]
29%
10^6 °m^{2}s^{-1}
(d) E2[$\tilde{\chi}_H$]
(e) C2[$\tilde{\chi}$(200mb)]
32%
10^6m^{2}s^{-1}
(f) E2[$\tilde{\chi}$(200mb)]
60°N
30°N
EQ
30°S
60°E
120°E
180°
120°W
50 55 60 65 70 75 80 85 90
year

respectively. The temporal variations of the C1[$\tilde{H}_I$], C2[$\tilde{\chi}_H$], and C2[$\tilde{\chi}$(200 mb)] time series have similar characteristics as the time series of the PNA mode (Figure 12a): two cycles of low-frequency (15~20 year) oscillations with the second cycle starting from the mid-1970s. However, the time evolution of C1[$\tilde{H}_I$], C2[$\tilde{\chi}_H$], and C2[$\tilde{\chi}$(200 mb)] are not precisely coherent with the time evolution of the PNA mode. It is possible that, in the EOF analysis, the signals associated with the PNA mode in each of the $\tilde{H}_I$, $\tilde{\chi}_H$, and $\tilde{\chi}$(200 mb) fields are distorted by the signals from other interdecadal disturbances and thus cannot be clearly isolated. This difficulty is commonly encountered when one uses EOF analysis. Since the temporal property of the first $\tilde{H}_I$, second $\tilde{\chi}_H$, and second $\tilde{\chi}$(200 mb) are at least to some extent similar to the PNA mode, it seems plausible to use these eigenmodes to illustrate the χ-maintenance analysis for the PNA mode.

Because the C1[$\tilde{H}_I$], C2[$\tilde{\chi}_H$], and C2[$\tilde{\chi}$(200 mb)] series have a similar oscillation, the dynamic relationship between the $\tilde{H}_I$, $\tilde{\chi}_H$, and $\tilde{\chi}$(200 mb) fields can be revealed from the spatial structures of E1[$\tilde{H}_I$], E2[$\tilde{\chi}_H$], and E2[$\tilde{\chi}$(200 mb)]. As shown in the E1[$\tilde{H}_I$] (Figure 14b), changes in diabatic heating anomalies are most significant in the tropics and are hardly discernible in the extratropics. A major positive $\tilde{H}_I$ center is located over the Indian Ocean, while two major $\tilde{H}_I$ negative centers are located northeast of Australia and over the South

China Sea. Since the χ_H field is the inverse Laplacian of the H_I field, the χ_H center should be at the same location as the H_I center but with the opposite sign. Indeed, the E2[$\tilde{\chi}_H$] mode (Figure 14d) exhibits a positive center to the northeast of Australia and a negative center over the Indian Ocean.

As for the divergent circulation, the E2[$\tilde{\chi}$(200 mb)] mode (Figure 14f) exhibits the positive and negative maximum centers at the locations close to that of E2[$\tilde{\chi}_H$]. It has been demonstrated by Kasahara (1982) and by Chen and Baker (1986) that the tropical diabatic heating is counterbalanced by the upward transport of thermal energy (or diabatic cooling). The vertical motion is diagnostically related to the divergent circulation. Following the approximate tropical thermal relation demonstrated by Kasahara and Chen and Yen, the χ-maintenance equation suggests that the $\tilde{\chi}_H$ and $\tilde{\chi}$(200 mb) centers should coincide if the latter is maintained by the former. Therefore, the resemblance between the spatial patterns of E2[$\tilde{\chi}_H$] and E2[$\tilde{\chi}$(200 mb)] indicates that the interdecadal change of the divergent circulation is essentially maintained (or induced) by that of the tropical diabatic heating.

In response to the interdecadal variation of the divergent circulation, two types of $\tilde{\psi}_E$ tendency, i.e., $\tilde{\psi}_{\chi E}$ and $\tilde{\psi}_{AVE}$, are generated to adjust the rotational circulation. Shown in Figure 15 are the second eigenmodes of the $\tilde{\psi}_{\chi E}$(200

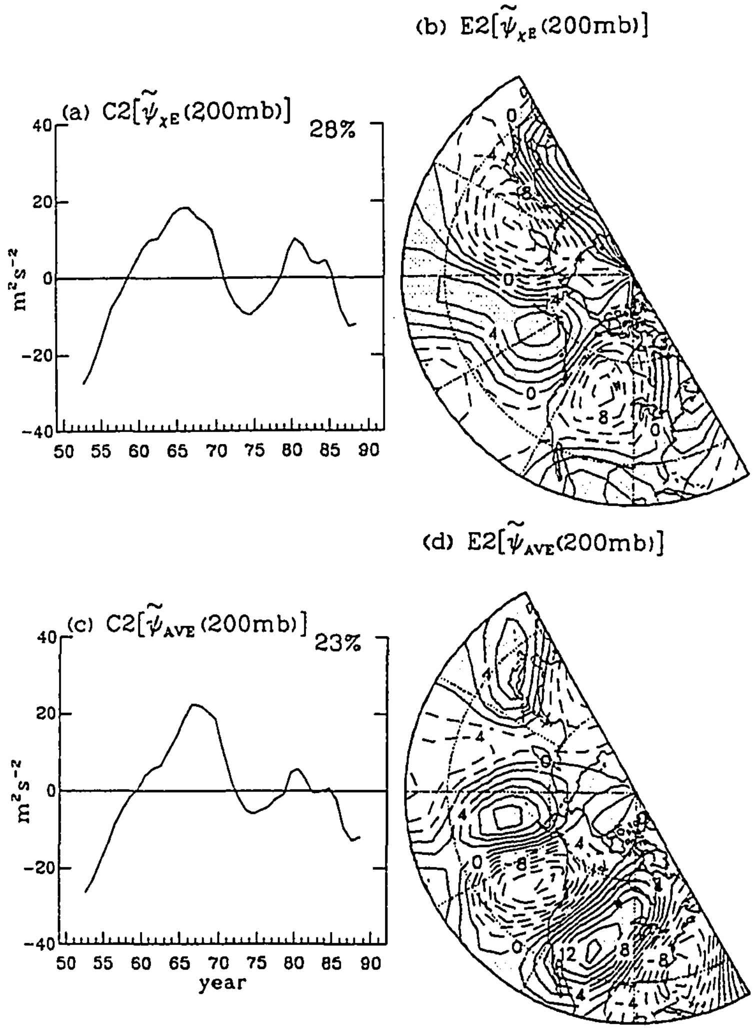

Figure 15. The EOF analysis associated with the ψ-budget analysis of the PNA mode. The eigencoefficients/ eigenvectores of the (a)/(b) second $\Psi_{\chi E}$(200 mb) and (c)/(d) second Ψ_{AVE}(200 mb) eigenmodes. The contour interval is 0.2 and the positive values are shaded.

mb) and Ψ_{AVE}(200 mb) fields. The total variance explained by the second $\Psi_{\chi E}$(200 mb) and Ψ_{AVE}(200 mb) eigenmodes is 28% and 23%, respectively. Both C2[$\Psi_{\chi E}$(200 mb)] and C2[Ψ_{AVE}(200 mb)] exhibit two approximate 20 year oscillations with the second oscillation beginning in the mid-1970s. Apparently, the aforementioned temporal characteristics are consistent with that of the eigenmodes used in the χ-maintenance analysis (Figure 14) and the PNA mode (Figure 12a). Thus, it should be legitimate to use the second eigenmodes of $\Psi_{\chi E}$(200 mb) and Ψ_{AVE}(200 mb) to illustrate the adjustment processes associated with the ψ-budget analysis for the PNA mode.

As demonstrated by E2[$\Psi_{\chi E}$(200 mb)] (Figure 15b) and E2[Ψ_{AVE}(200 mb)] (Figure 15d), the changes of $\Psi_{\chi E}$ and Ψ_{AVE} are to some extent counterbalanced and are spatially in quadrature with the Ψ_E anomaly associated with the PNA mode (Figure 12b). The adjustment processes for the rotational circulation, as interpreted from the ψ-budget analysis, can be illustrated by the spatial relationship between $\Psi_{\chi E}$, Ψ_{AVE}, and Ψ_E(200 mb). The maintenance of the anomalous low over south of Alaska (see figure 12b) is used to illustrate the aforementioned adjustment processes. According to the quasi-geostrophic model (e.g., Holton 1992), the eastward vorticity advection by atmospheric flows from regions west of long wave troughs to those west of long wave ridges should be caused by vortex stretching over the former regions and consumed in the latter regions. As shown by $E2[\Psi_{\chi E}(200\ mb)]$ (Figure 15b), the supply of positive vorticity over east of Japan induces negative Ψ_E tendency and the consumption of positive vorticity over west coast of North America induces positive Ψ_E tendency. As shown by $E2[\Psi_{AVE}(200\ mb)]$ (Figure 15d), to counterbalance the Ψ_E tendency induced by the vorticity source, the depletion (accumulation) of positive vorticity by the advection of rotational flow induces a positive (negative) Ψ_E tendency over the area east of Japan (west coast of North America). The two physical processes, $\Psi_{\chi E}$ and Ψ_{AVE}, counterbalance each other to maintain/adjust the Ψ_E anomaly. Conversely, the opposite situation can apply to the maintenance of the anomalous high.

Based upon the χ-maintenance and ψ-budget analyses described above, the PNA mode is regarded as a result of the chain relation: $\tilde{H}_I \rightarrow \tilde{\chi}_H \rightarrow \tilde{\chi}(200\ mb) \rightarrow \Psi_{\chi E}(200\ mb) \rightarrow \Psi_{AVE}(200\ mb) \rightarrow \Psi_E(200\ mb)$. As mentioned previously, the $C1[\tilde{H}_I]$ time series undergoes a low-frequency oscillation and the $E1[\tilde{H}_I]$ mode exhibits a positive center over the Indian Ocean and a negative center over the western tropical Pacific. The aforementioned results indicate that there is a seesaw oscillation of $\tilde{H}_I$ anomalies between the Indian Ocean and the tropical western Pacific. Therefore, the PNA mode in the model is induced by the seesaw oscillation of interdecadal diabatic heating anomalies between the Indian Ocean and tropical western Pacific.

The χ-maintenance analysis associated with the PNAW mode is illustrated by the second eigenmode of $\tilde{H}_I$ and the first eigenmodes of $\tilde{\chi}_H$ and $\tilde{\chi}$(200 mb) (Figure 16). The total variance accounted for by the second $\tilde{H}_I$, first $\tilde{\chi}_H$, and first $\tilde{\chi}$(200 mb) eigenmodes is 21%, 52%, and 47%, respectively. For the temporal variation of these eigenmodes, the C2[$\tilde{H}_I$], C1[$\tilde{\chi}_H$], and C1[$\tilde{\chi}$(200 mb)] series in Figure 15 all show a descending trend before the mid-1970s and an ascending trend afterward. The aforementioned temporal characteristics are similar to those of the PNAW mode (Figure 12c). As argued previously, the temporal variation of C2[$\tilde{H}_I$], C1[$\tilde{\chi}_H$], and C1[$\tilde{\chi}$(200 mb)] may not be precisely the same as that of the PNAW mode because the EOF analysis can not perfectly isolate the interdecadal modes as we would like. Since the C2[$\tilde{H}_I$], C1[$\tilde{\chi}_H$], and C1[$\tilde{\chi}$(200 mb)] series have characteristics similar to the PNAW mode, it should be acceptable to use the second eigenmode of $\tilde{H}_I$ and the first eigenmodes of $\tilde{\chi}_H$ and $\tilde{\chi}$(200 mb) to delineate the χ-maintenance for the PNAW mode.

As for the spatial structure, E2[$\tilde{H}_I$] (Figure 16b) exhibits its centers around the tropics: a major positive center over the tropical central Pacific and a major negative center north of Australia. The extratropical heating anomalies are not discernible in the E2[$\tilde{H}_I$] pattern. In association with the E2[$\tilde{H}_I$] distribution, both E1[$\tilde{\chi}_H$] (Figure

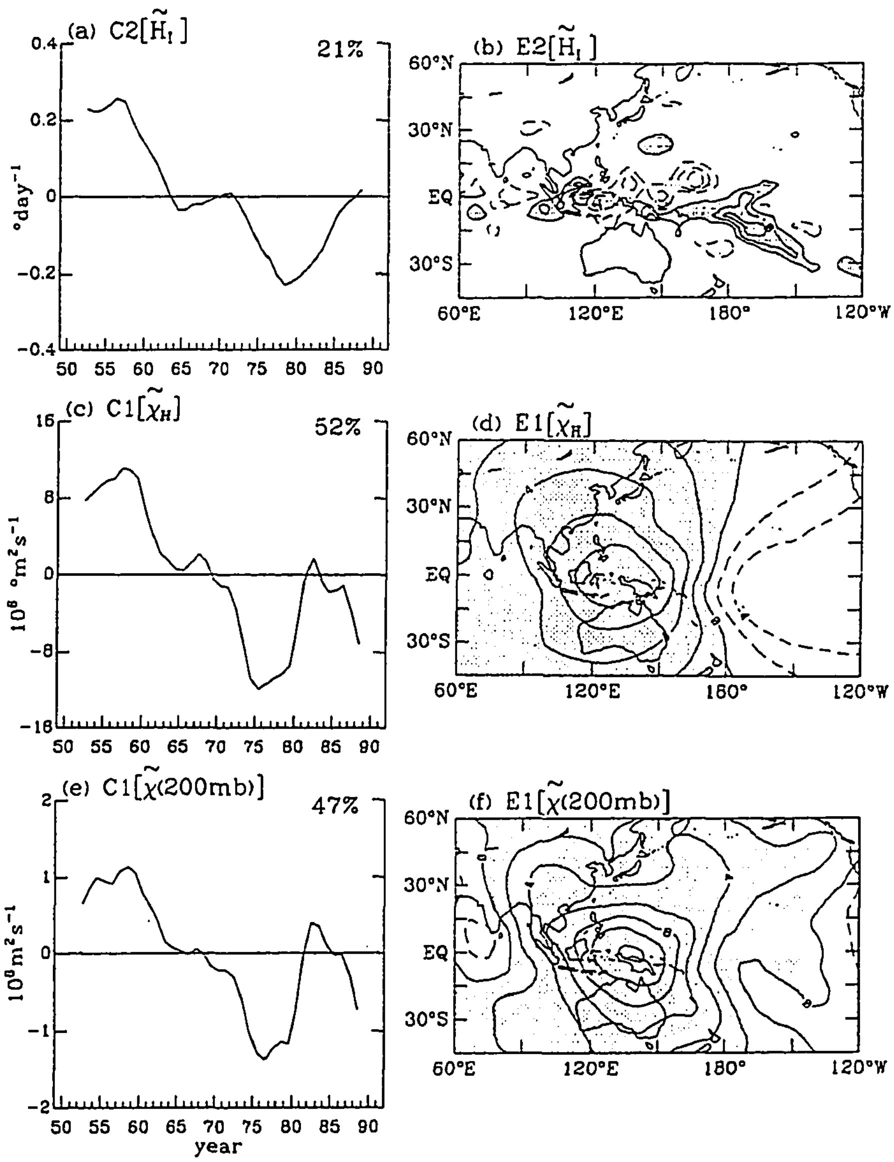

Figure 16. As in Figure 14, except for the EOF analyses associated with the χ-maintenance analysis of the PNAW mode. Shown here are the (a)-(b) second $\tilde{H}_I$, (c)-(d) first $\tilde{\chi}_H$, and (e)-(f) first $\tilde{\chi}$(200 mb) eigenmodes.

16d) and E2[$\tilde{\chi}$(200 mb)] (Figure 16f) have a positive center north of Australia and negative anomalies over the eastern Pacific. The similarity between the patterns of E2[$\tilde{\chi}_H$] and E2[$\tilde{\chi}$(200 mb)] demonstrates that the first eigenmode of $\tilde{\chi}$(200 mb) is primarily maintained by the first eigenmode of $\tilde{\chi}_H$ or the second eigenmode of $\tilde{H}_I$.

To illustrate the ψ-budget analysis associated with the PNAW mode, the first eigenmodes of $\tilde{\Psi}_{\chi E}$(200 mb) and $\tilde{\Psi}_{AVE}$(200 mb) are displayed in Figure 17. The total variance explained by the first $\tilde{\Psi}_{\chi E}$(200 mb) and $\tilde{\Psi}_{AVE}$(200 mb) eigenmodes is 45% and 53%, respectively. The temporal variation of C1[$\tilde{\Psi}_{\chi E}$(200 mb)] and C1[$\tilde{\Psi}_{AVE}$(200 mb)] is characterized by a descending trend during the 1960s and the 1970s and an ascending trend during the 1980s. Obviously, the first eigenmodes of $\tilde{\Psi}_{\chi E}$(200 mb) and $\tilde{\Psi}_{AVE}$(200 mb) have the key temporal property of the PNAW mode (Figure 12c) as well as the eigenmodes used in the χ-maintenance analysis of the PNAW mode (Figure 16). It thus seems appropriate to use the first eigenmodes of $\tilde{\Psi}_{\chi E}$(200 mb) and $\tilde{\Psi}_{AVE}$(200 mb) to depict the ψ-budget analysis for the PNAW mode.

As for the spatial structure, E1[$\tilde{\Psi}_{\chi E}$(200 mb)] (Figure 17b) and E1[$\tilde{\Psi}_{AVE}$(200 mb)] (Figure 17d) are more or less opposite to each other and spatially in quadrature with the PNAW mode which is represented by the PNA region E2[$\tilde{\Psi}_E$(200 mb)] (Figure 12d). The spatial relationship between E1[$\tilde{\Psi}_{\chi E}$(200 mb)],

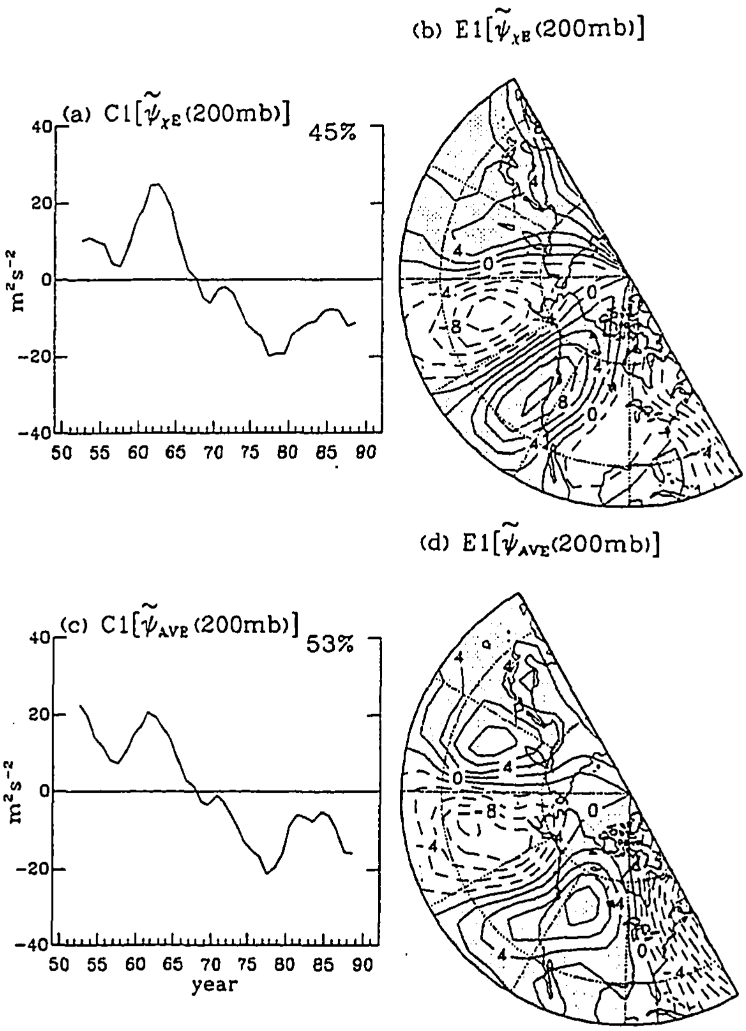

Figure 17. As in Figure 15, except for the EOF analyses associated with the ψ-budget analysis of the PNAW mode. Shown here are the (a)-(b) first $\Psi_{\chi E}$(200 mb) and (c)/(d) first Ψ_{AVE}(200 mb) eigenmodes.

$E1[\Psi_{AVE}(200\ mb)]$, and the PNA region $E2[\Psi_E(200\ mb)]$ demonstrates clearly that the PNAW mode is primarily maintained by the mutual adjustment processes between $E1[\Psi_{\chi E}(200\ mb)]$ and $E1[\Psi_{AVE}(200\ mb)]$.

Combining the results from the χ-maintenance and ψ-budget analyses associated with the PNAW mode, it is clear that the PNAW mode owes its existence to the interdecadal change of tropical diabatic heating. The interdecadal diabatic heating anomalies associated with the PNAW mode are represented by the second $\tilde{H}_I$ eigenmode in Figure 16. The $C2[\tilde{H}_I]$ series exhibits a descending trend from the 1950s to the 1980s. The $E2[\tilde{H}_I]$ mode has a positive center over the tropical central Pacific and a negative center over the tropical western Pacific. As the simulation proceeds from the 1950s to the 1980s, the heating anomaly over the tropical western (central) Pacific becomes positive (negative). In other words, the positive heating anomaly shifts from the tropical central Pacific to the tropical western Pacific as the simulation progresses from the early to the late stages. Therefore, the PNAW mode in the model can be considered to result from the westward displacement of the tropical heating anomalies from the central to western Pacific.

In this section, the dynamic processes associated with the maintenance of the PNA and PNAW modes were illustrated by the χ-maintenance and ψ-budget analyses. Results of these two analyses suggest that the interdecadal change of tropical diabatic heating maintains that of the divergent circulation. The anomalous divergent circulation interacts with the anomalous rotational circulation to result in the interdecadal change of the atmospheric circulation. Moreover, the analyses also suggest that (1) the PNA mode is maintained by the seesaw oscillation of the interdecadal tropical heating anomalies between the India Ocean and western tropical Pacific and (2) the PNAW mode is likely induced by the westward shift of the interdecadal tropical heating anomalies from the central Pacific to the western Pacific. The aforementioned results answer the third question proposed in the Introduction.

5. Response of general circulation statistics

In this section, the general circulation statistics are analyzed in terms of transient heat flux for the thermal field and cyclone activity for the dynamic field.

a. *Transient heat flux*

As discussed previously, the transient heat flux is examined in terms of $\chi_{HF} = \nabla^{-2}[-\nabla\cdot\overline{(V''T'')}]$. The double prime indicates the 2.5-6 day bandpass filter field, while the overbar denotes the winter mean. It was shown by observational study (e.g., Lau and Wallace 1979) that the winter-averaged transient heat flux in the lower troposphere is mainly composed of divergent components and is directed poleward from high to low mean temperatures. Since the divergent circulation in the lower troposphere reaches its maximum at 850 mb, we thus analyzed the χ_{HF} at this level. The relationship between the interdecadal changes of transient heat flux and the temperature field were analyzed in two aspects: horizontal structure and zonal-mean component. Results of the analyses are presented in the following subsections.

i. Horizontal structure

In order to be sure that the GCM experiment could generate the appropriate transient heat flux and temperature field, we first examined the winter climatologies of χ_{HF}(850 mb) and T(850 mb) simulated in the ER experiment. Shown in Figures 18a and 18c are the multi-winter (1950-92) means of T(850 mb) and χ_{HF}(850 mb) from the ER experiment, respectively. The $\nabla\overline{\chi}_{HF}$ vectors are superimposed on $\overline{\chi}_{HF}$ contours to depict the direction of the transient heat transport. As shown in Figure 18a, $\overline{T}$(850 mb) decreases poleward. In association with this distribution, the $\overline{\chi}_{HF}$(850 mb) field diverges from low latitudes and converges toward the polar cap. The aforementioned results indicate that the winter mean thermal structure is to some extent maintained by the

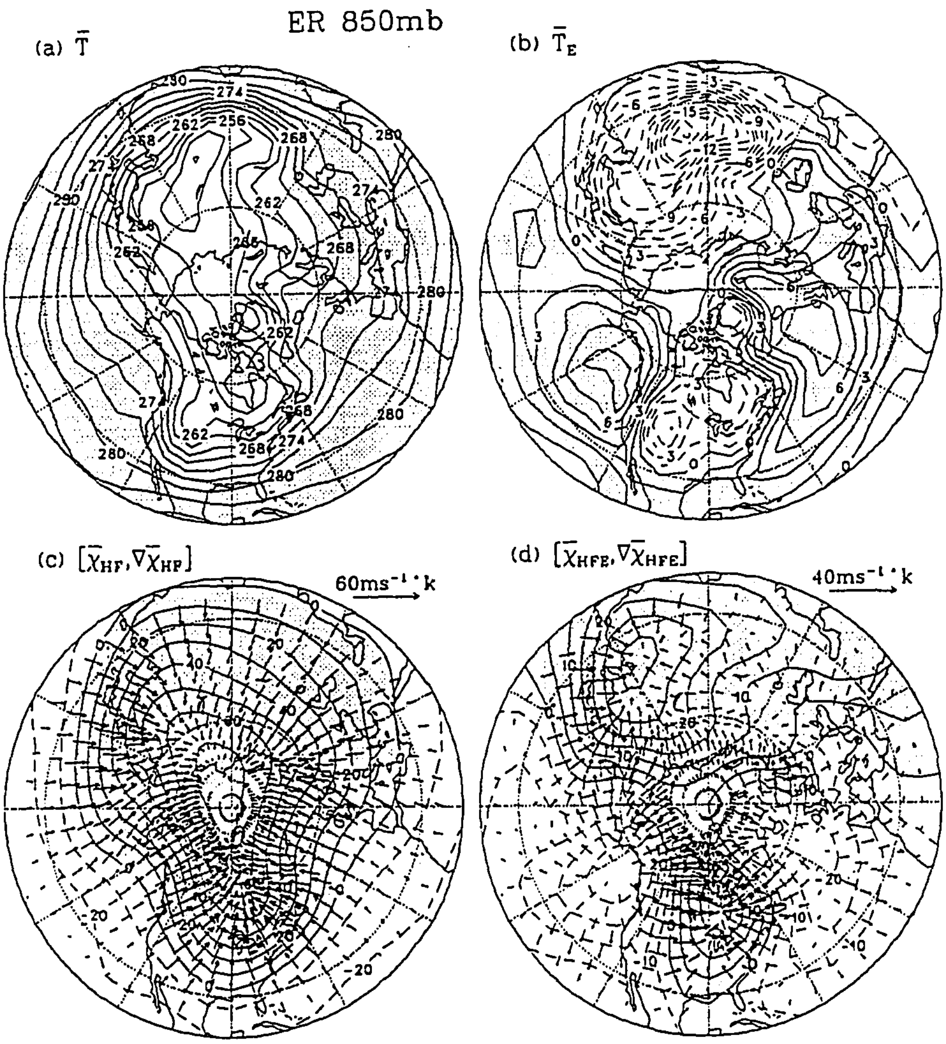

Figure 18. The multiple (1950-92) winter-mean (a) total temperature ($\bar{T}$), (b) eddy temperature ($\bar{T}_E$), (c) total transient heat flux ($\bar{\chi}_{HF}$), and (d) eddy transient heat flux ($\bar{\chi}_{HFE}$) for the ER 850 mb circulation. The vectors derived from the $\nabla\bar{\chi}_{HF}$ and $\nabla\bar{\chi}_{HFE}$ are superimposed on (c) and (d), respectively, to delineate the transport of transient heat flux. Contour intervals: (a) 3 °K, (b) 1.5 °K, (c) 10^7 m^2s^{-1} °K, and (d) 5×10^6 m^2s^{-1} °K. $\bar{T} \geq 265$ °K is shaded in (a) and the positive value are shaded in (b)-(d).

poleward transport of the winter-averaged transient heat flux. Both $\overline{\chi}_{HF}$(850 mb) and $\overline{T}$(850 mb) exhibit characteristics consistent with the observed (e.g. see Lau and Wallace 1979, Figure 3; Lau et al. 1981, Figure II.C.3.e). As for the amplitude of the transient heat flux, a careful comparison between the result of our ER experiment (Figure 18c) and that compiled by Lau et al. (1981, Figure II.C.3.e) based upon 1966-76 NMC analyses reveals that the transient heat flux simulated in the ER experiment is about 70~80% in amplitude as the observation. Except the amplitude is underestimated, the 850 mb transient heat flux in the ER experiment can be considered to be simulated closely to the observation.

In order to illustrate the relationship between the eddy components of the temperature field and transient heat flux, $\overline{T}_E$(850 mb) and $\overline{\chi}_{HFE}$(850 mb) are displayed in Figures 18b and 18d, respectively. The comparison between $\overline{T}_E$(850 mb) and $\overline{\chi}_{HFE}$(850 mb) reveals that the transient heat diverges from thermal ridges over the eastern Pacific and North Atlantic to thermal troughs over central Asia and North America. The above results describe the dynamic relationship between $\overline{T}_E$(850 mb) and $\overline{\chi}_{HFE}$(850 mb) as follows: the positive (negative) temperature anomaly induces the divergence (convergence) of the transient heat flux.

In addition to the multi-winter mean analysis, the interdecadal variations of the temperature field and transient heat flux are examined. The horizontal structure of the interdecadal variations in the T(850 mb) and χ_{HF}(850 mb) fields may be inferred from the $\Delta\tilde{T}$(850 mb) and $\Delta\tilde{\chi}_{HF}$(850 mb) variances, respectively. Both RMS[$\Delta\tilde{T}$(850 mb)] and RMS[$\Delta\tilde{\chi}_{HF}$(850 mb)] charts are shown in Figure 19. The RMS[$\Delta\tilde{T}$(850 mb)] values are larger in the high latitudes and smaller in the low latitudes. The contrast between the RMS[$\Delta\tilde{T}$(850 mb)] values in the high- and low- latitudes indicates that the $\tilde{T}$(850 mb) field has more interdecadal variability in the high latitudes. Two major RMS[$\Delta\tilde{T}$(850 mb)] centers are located over eastern Siberia and North America, while two other RMS[$\Delta\tilde{T}$(850 mb)] centers are situated near Newfoundland and northern Russia.

As shown in Figure 19b, the RMS[$\Delta\tilde{\chi}_{HF}$(850 mb)] is greatest in both the high- and mid-latitudes. This distribution indicates that the interdecadal variation of transient heat flux in the midlatitudes is as significant as that in the high latitudes. Four RMS[$\Delta\tilde{\chi}_{HF}$] centers are located over northern Russia, eastern Siberia/North Pacific, central Canada, and Greenland/North Atlantic. These RMS[$\Delta\tilde{\chi}_{HF}$(850 mb)] centers, to some extent, coincide with the RMS[$\Delta\tilde{T}$(850 mb)] centers shown in Figure 18a. The spatial coherence between the RMS[$\Delta\tilde{T}$(850 mb)] and RMS[$\Delta\tilde{\chi}_{HF}$(850 mb)] centers implies that the interdecadal variations of the temperature field and the transient heat flux might have a similar spatial pattern.

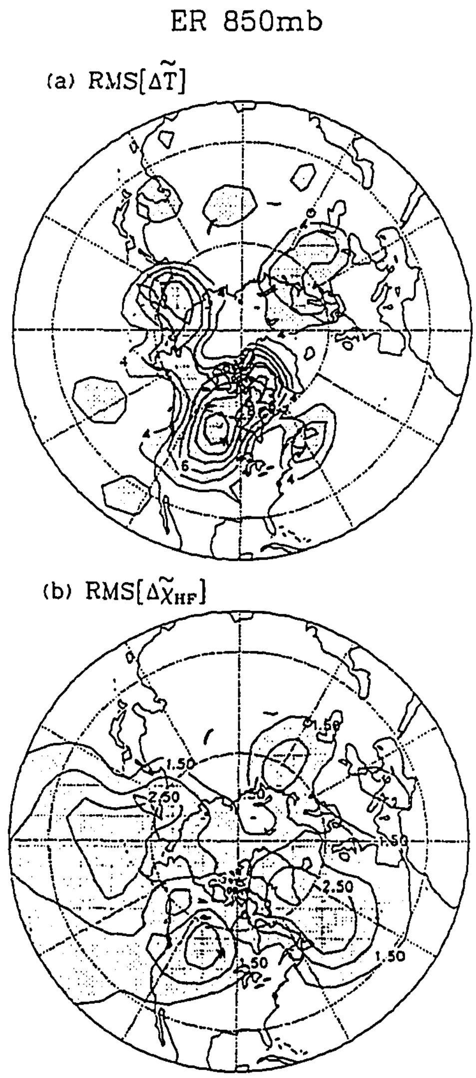

Figure 19. The RMS distributions of the (a) $\Delta\tilde{T}$(850 mb) and (b) $\Delta\tilde{\chi}_{HF}$(850 mb) of the ER experiment. Contour intervals: (a) 0.1°K and (b) 0.5×10^{6} m^2s^{-1} °K. In (a), the RMS values larger than 0.5°K are heavily shaded and those between the 0.5 and 0.4 °K are lightly shaded. In (b), the RMS values larger than 2×10^{6} m^2s^{-1} °K are heavily shaded and those between the 1.5×10^{6} and 2×10^{6} m^2s^{-1} °K are lightly shaded.

In order to further examine the dynamic relationship between the interdecadal variability of the temperature field and the transient heat flux, EOF analyses of $\tilde{T}$(850 mb) and $\tilde{\chi}_{HFE}$(850 mb) were performed. The reason using the EOF analysis of $\tilde{\chi}_{HFE}$(850 mb) instead of $\tilde{\chi}_{HF}$(850 mb) is simply due to the fact that the EOFs of $\tilde{\chi}_{HFE}$(850 mb) can more closely match those of $\tilde{T}$(850 mb). Consequently, physical interpretations can be made by comparing the EOF analysis of $\tilde{T}$(850 mb) and $\tilde{\chi}_{HFE}$(850 mb).

The first two eigenmodes of $\tilde{T}$(850 mb) and $\tilde{\chi}_{HFE}$(850 mb) are plotted in Figure 20. The total variance accounted for by the two leading eigenmodes are 32% and 23% for $\tilde{T}$(850 mb), and 53% and 22% for $\tilde{\chi}_{HFE}$(850 mb). In the following discussion, the first (second) eigenmode of $\tilde{T}$(850 mb) is compared with the second (first) eigenmode of $\tilde{\chi}_{HFE}$(850 mb).

As shown in Figure 20a, C1[$\tilde{T}$(850 mb)] and C2[$\tilde{\chi}_{HFE}$(850 mb] exhibit a coherent oscillation. The spatial structures of E1[$\tilde{T}$(850 mb)] (Figure 20c) and E2[$\tilde{\chi}_{HFE}$(850 mb)] (Figure 20e) are more or less opposite. It is illustrated by the $\overline{\chi}_{HFE}$(850 mb) field (Figure 18d) that the negative χ_{HF} anomalies represent the divergence of transient heat flux. The spatial relationship between E1[$\tilde{T}$(850 mb)] and E2[$\tilde{\chi}_{HFE}$(850 mb)] indicates that on the decadal time scale, the transient heat flux diverges out of warm anomalies and converges toward cold anomalies.

Figure 20. The first two eigenmodes of the interdecadal-change temperature and eddy transient heat flux from the ER 850 mb winter circulation. The C1($\tilde{T}$) and C2($\tilde{\chi}_{HFE}$) series are plotted in (a) and C2($\tilde{T}$) and C1($\tilde{\chi}_{HFE}$) series are shown in (b). The contour intervals for (c) E1($\tilde{T}$), (d) E2($\tilde{T}$), (e) E2($\tilde{\chi}_{HFE}$), and (f) E1($\tilde{\chi}_{HFE}$) are 0.15. The positive values of the eigenvectors are shaded.

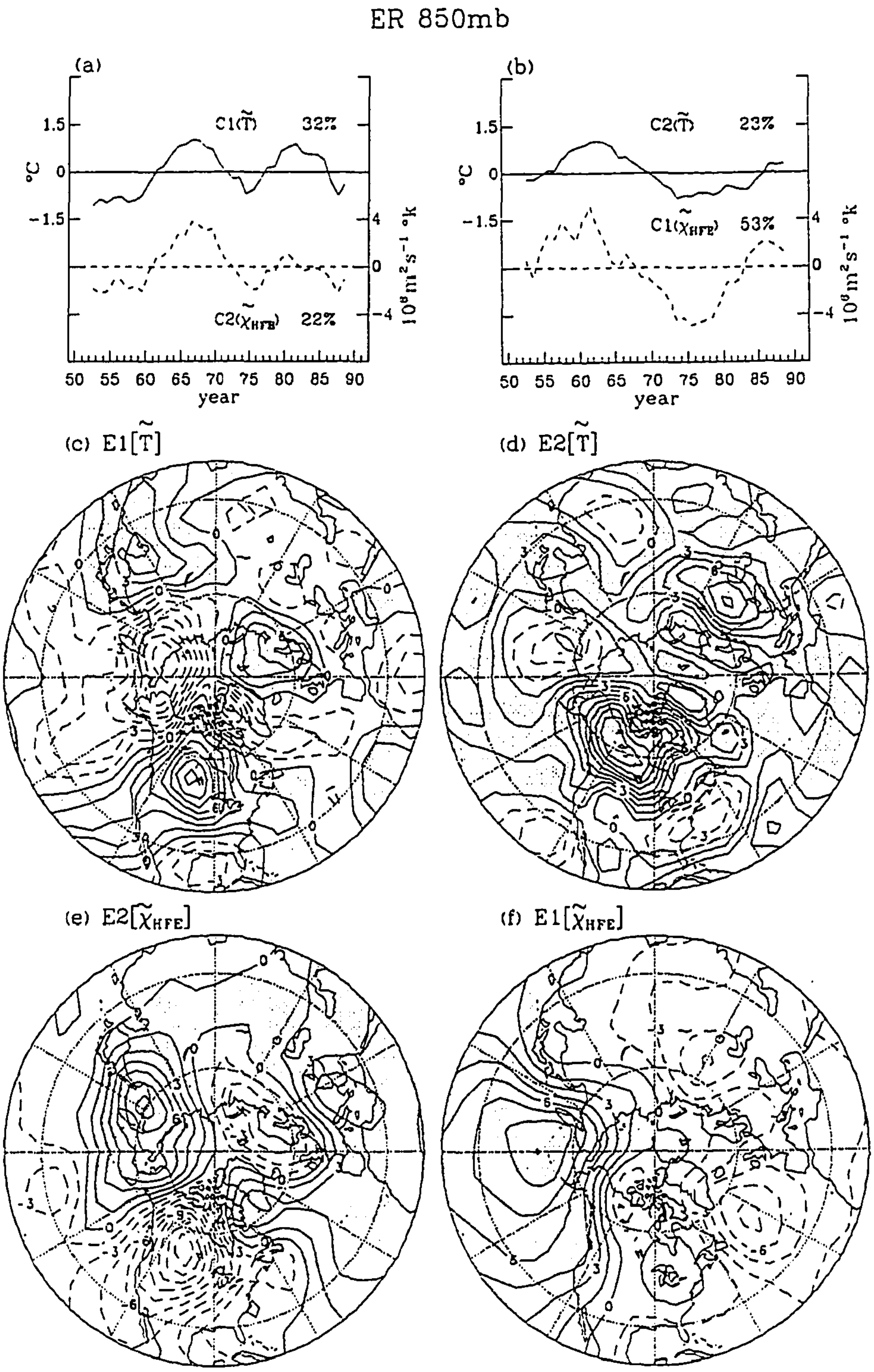
ER 850mb
(a)
C1($\tilde{T}$) 32%
C2($\tilde{\chi}_{HFE}$) 22%
°C
$10^6 m^2 s^{-1}$ °K
year
(b)
C2($\tilde{T}$) 23%
C1($\tilde{\chi}_{HFE}$) 53%
°C
$10^6 m^2 s^{-1}$ °K
year
(c) E1[$\tilde{T}$]
(d) E2[$\tilde{T}$]
(e) E2[$\tilde{\chi}_{HFE}$]
(f) E1[$\tilde{\chi}_{HFE}$]

As for the other pair of eigenmodes, Figure 20b shows that the C2[$\tilde{T}$(850 mb)] and C1[$\tilde{\chi}_{HFE}$(850 mb)] series oscillate coherently. The E1[$\tilde{\chi}_{HFE}$(850 mb)] mode (Figure 20f) shows a major negative anomaly across the entire Pacific and positive anomalies over the North Atlantic and Eurasia. In the temperature field, the E2[$\tilde{T}$(850 mb)] mode (Figure 20d) exhibits a positive anomaly in the northern Pacific and negative anomalies over the North Atlantic and Eurasia. The spatial relationship between E1[$\tilde{\chi}_{HFE}$(850 mb)] and E2[$\tilde{T}$(850 mb)] indicates that a cross hemisphere transport of the transient heat is regulated by the seesaw oscillation of temperature anomalies between the northern Pacific and the North Atlantic/Eurasia region.

Since the interdecadal variation of the thermal field is analyzed in this section, it is also interesting to examine the dynamic relationship between the interdecadal changes of the thermal and dynamic fields. Thus, the EOF analyses of $\tilde{\psi}$(200 mb), $\tilde{\psi}_E$(200 mb) and $\tilde{T}$(850 mb) are compared. As for the temporal variation, C1[$\tilde{\psi}$(200 mb)] (Figure 5a), C1[$\tilde{\psi}_E$(200 mb)] (figure 11a), and C1[$\tilde{T}$(850 mb)] (Figure 20a) exhibit a coherent oscillation. Spatially, the negative centers of E1[$\tilde{\psi}$(200 mb)] (Figure 5d) south of Alaska, Greenland, and central Russia coincide with the negative centers of E1[$\tilde{T}$(850 mb)]. It was discussed previously that the expansion of the circumpolar vortex (or the deepening of climatological troughs) is most significant at the negative centers of E1[$\bar{\Psi}$(200 mb)]. The spatial coherence between the negative centers of E1[$\tilde{T}$(200 mb)] and E1[$\tilde{T}$(850 mb)] indicates that the deepening of the three climatological troughs is induced by the anomalous cooling in the respective regions. In view of the above relationship, we may further infer that the positive centers of E1[$\tilde{T}$(850 mb)] over central Asia and North America can amplify the climatological ridges. This argument is supported by the results that E1[$\tilde{T}$(850 mb) exhibits a pattern similar to the 850 mb mean stationary eddies (i.e., $\bar{\Psi}_E$ field in Figure 1d), while C1[$\tilde{T}$(850 mb)] contains an increasing trend. Therefore, the first $\tilde{T}$(850 mb) eigenmode can induce the enhancement of the stationary eddies.

The E1[$\tilde{T}$(850 mb)] and E1[$\tilde{\Psi}_E$(200 mb)] (Figure 11b) modes exhibit a similar spatial pattern, particularly over the PNA region. Note that C1[$\tilde{T}$(850 mb)] and C1[$\tilde{\Psi}_E$(200 mb)] have a coherent oscillation. Thus, we can consider the first $\tilde{T}$(850 mb) eigenmode as the corresponding PNA mode of the thermal field. However, the teleconnection pattern in the thermal field is not as well organized as that in the dynamic field.

As for the second eigenmodes of $\tilde{\Psi}_E$(200 mb) (in Figure 11) and $\tilde{T}$(850 mb) (in Figure 20), the temporal and spatial properties of these two modes are similar to some extent. Therefore, the second $\tilde{T}$(850 mb) eigenmode can be considered as the corresponding PNAW mode of the thermal field.

Obviously, the teleconnection pattern is more discernible in E2[Ψ_E(200 mb)] (Figure 11d) than in E2[$\tilde{T}$(850 mb)] (Figure 20d).

The comparison between the EOF analyses of Ψ(200 mb), Ψ_E(200 mb), and $\tilde{T}$(850 mb) reveals that: (1) the deepening (amplification) of climatological troughs (ridges) is possibly maintained by anomalous cooling (warming), and (2) the thermal field exhibits the interdecadal modes corresponding to those of the dynamic field.

ii. Zonal-mean component

It is well understood that the eddy sensible heat transport serves to maintain the zonal flow. Commonly, the eddy sensible heat transport is subdivided into its standing and transient components. Chen (1982) demonstrated that both standing and transient waves play important roles in the total eddy sensible heat transport. Previous studies (e.g., Rogers and Raphael 1992) also showed that the standing component of eddy sensible heat transport primarily circulates around the stationary eddies. Therefore, the effect of standing eddy sensible heat transport on the zonal flow cannot be examined from the horizontal structure. An alternative way to examine the relationship between the standing eddy sensible heat transport and zonal flow is to compare their zonal-mean components. For this reason, we analyzed the zonal-mean heat flux in terms of the stationary and transient (2.5-6 days) components of the meridional eddy sensible heat transport, i.e., $(\bar{v}_E\bar{T}_E)_Z$ and $(\overline{v''_E T''_E})_Z$, respectively, and compare them with the zonal-mean temperature field. It was demonstrated by Williamson and Williamson (1987) that the transient component of meridional sensible heat transport at 850 mb simulated in the CCM1 of R15 resolution exhibits a spatial pattern similar to that of the NMC analysis compiled by Lau et al. (1981). However, the amplitude of transient meridional sensible heat transport in the CCM1 is about 80% as large as that of the NMC analysis.

One way to depict the temporal variation of the zonal-mean variable is to use the latitude-time (y-t) diagram. The y-t diagrams of the interdecadal-change zonal-mean temperature field, stationary, and transient meridional eddy heat transports are illustrated in Figure 21. The interdecadal change of the temperature field (Figure 21a) is prominent at high latitudes. Over the area north of 60°N, a major warming spans from the late-1950s to the early-1960s, and a substantial cooling occurs from the late-1970s to the mid-1980s. On the other hand, the $\Delta\tilde{T}_Z$(850 mb) anomalies at low latitudes seem to oscillate oppositely in an opposite manner: a relatively cold anomaly during the 1950s and 1960s and a warm anomaly during the 1980s. The aforementioned change of $\Delta\tilde{T}_Z$(850 mb) anomalies between high and low

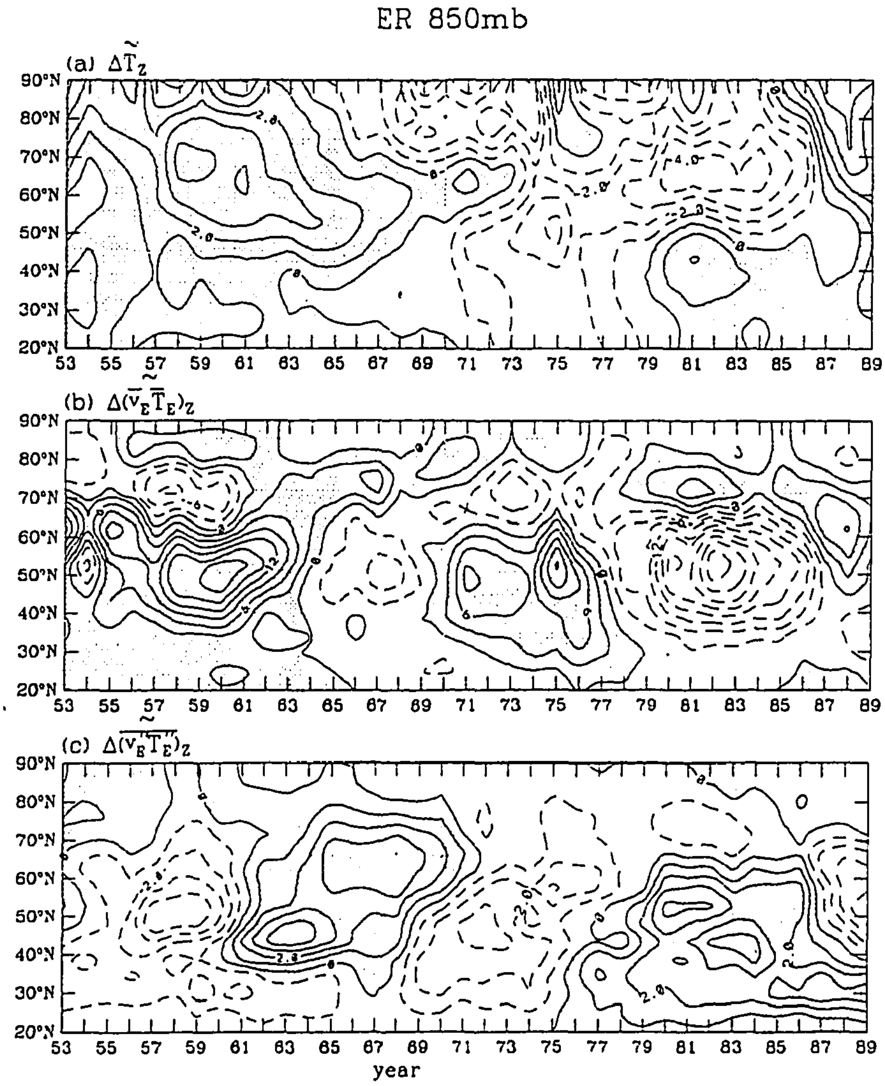

Figure 21. The y-t diagrams of interdecadal anomalies of (a) temperature, (b) standing component of meridional eddy sensible heat transport, and (c) transient component of meridional eddy sensible heat transport for the ER 850 mb winter circulation. Contour intervals are (a) 0.1 °K, (b) 0.3 ms^{-1} °K, and (c) 0.1 ms^{-1} °K. The positive values are shaded.

latitudes reveals that: (1) before the mid-1980s, the temperature over the polar cap exhibited a cooling trend, and (2) in association with the polar cooling, the north-south temperature gradient or north-south differential heating changes. As discussed previously, the three major expansions of the circumpolar vortex are induced by the regionalized anomalous cooling. In view of this relationship, one can also infer that the equatorward expansion of the circumpolar vortex is possibly induced by cooling over the polar cap. This argument is supported by the result that there is a similar decadal trend between the cooling over the polar cap (as revealed in Figure 21a) and the increase of the total circumpolar vortex size (as revealed in Figure 6a).

In conjunction with the temperature change, the stationary meridional sensible heat transport (Figure 21b) moves poleward (equatorward) south (north) of 65°N during the major warming phase around the late 1950s. An opposite situation exists during the major cooling phase around the 1980s. A dynamic relationship can be derived from the aforementioned results: on the decadal time scale, the anomalous warming (cooling) is maintained by the convergence (divergence) of the stationary (transient) meridional eddy heat transport. This relationship is consistent with that found in the observational study by van Loon and Williamson (1976). However, this relationship is only valid during the major warming and cooling phases and it does not apply well during the transition period between the 1960s and the 1970s when the changes of temperature at high latitudes are weaker.

As shown in Figure 21c, the transient component of meridional eddy heat transport is more or less opposite to its stationary counterpart, but its magnitudes are much smaller. The divergence (convergence) of transient meridional eddy heat transport occurs during the anomalous warming (cooling) phase. The contrasts in terms of the amplitude and phase between Figure 21b and 21c imply that: (1) the standing waves are the major agent for the meridional eddy sensible heat transport on the decadal time scale, and (2) the contribution of the standing waves to the total meridional eddy sensible heat transport is offset by that of the transient waves. The sign reversal between the stationary and transient components of the meridional eddy heat transport is consistent with the observational result obtained by Rogers and Raphael (1992).

b. *Cyclone activity*

Blackmon et al. (1977) demonstrated that the cyclone activity near the storm track regions can be illustrated by the RMS statistics of the 2.5-6 day filtered geopotential height. Williamson and Williamson (1987) reported that the winter RMS distribution of the 2.5-6 day filtered 300 mb geopotential height simulated in the CCM1 of R15 resolution exhibits a pattern similar to the observation as compiled by Lau et al. (1981) based upon the 1966-76 NMC data. However, the amplitude of the RMS statistics in the CCM1 is about 70~80% as much as that of the NMC analysis. Adopting Blackmon et al.'s (1977) approach, we analyzed the cyclone activity in terms of winter RMS statistics of the bandpass (2.5-6 days) filtered short-wave (wavenumbers 5-15) ψ(200 mb) field (i.e., RMS(ψ'')). To depict the characteristics of the cyclone activity simulated in the ER experiment, the multi-winter mean RMS(ψ'') are plotted in Figure 22a (shaded regions) together with the $\overline{\psi}$(200 mb) contours. The climatology of the cyclone activity is characterized by two elongated centers (heavily shaded areas) across much of the Pacific and North Atlantic. These two centers coincide with sites of observed Pacific and North Atlantic storm tracks (e.g., Blackmon et al. 1977; Lau 1979, 1988), where they are downstream and poleward of the East Asian and North American subtropical jet stream maxima, respectively. To examine the variation of cyclone activity on the decadal time scale, the RMS of ΔRM$\tilde{S}$(ψ'') was computed and plotted in Figure 22b. As revealed from the RMS chart, the interdecadal variability of cyclone activity is most significant over the eastern Pacific/North America and eastern Atlantic. These two regions are on the downstream side of the two major storm tracks.

ER 200mb

(a) $[\bar{\psi}, \overline{\mathrm{RMS}(\psi'')}]$

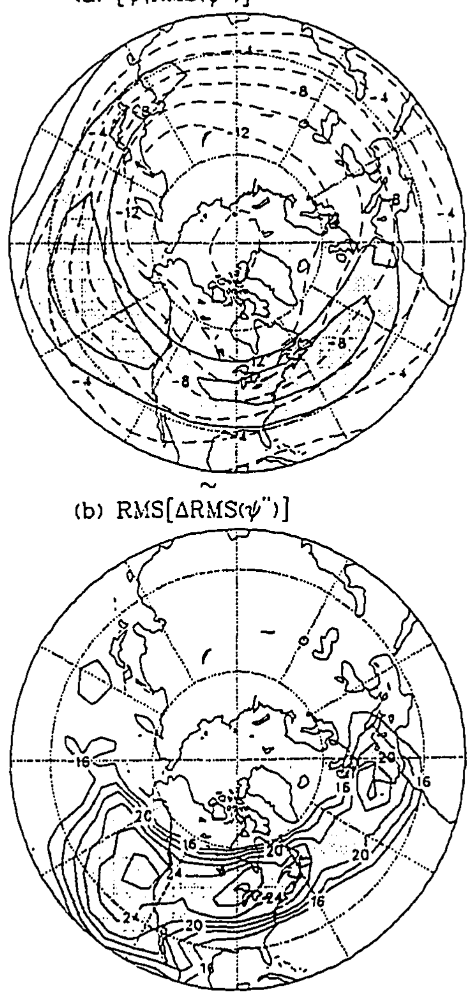

Figure 22. (a) The winter climatology (1950-92) of storm track activity [RMS(ψ''), shaded area] is superimposed on the climatological total streamfunction contours which are in units of $2\text{x}10^7\ m^2s^{-1}$. The RMS(ψ'') values between $3\text{x}10^6\ m^2s^{-1}$ and $3.5\text{x}10^6\ m^2s^{-1}$ are lightly shaded, and those greater than $3.5\text{x}10^6\ m^2s^{-1}$ are heavily shaded. (b) The RMS of the interdecadal-change RMS(ψ'') in units of $2\text{x}10^4\ m^2s^{-1}$. The RMS values larger than $2.2\text{x}10^5\ m^2s^{-1}$ are heavily shaded, and those between $2.2\text{x}10^5\ m^2s^{-1}$ and $1.6\text{x}10^5\ m^2s^{-1}$ are lightly shaded.

It was pointed out by Blackmon et al. (1977) that the locations of the storm tracks are related to those of the subtropical jet streams. There should thus be a connection between the interdecadal variability of cyclone activity and zonal wind. To examine the dynamic relationship between the interdecadal variability of cyclone activity and zonal wind, EOF analyses of $RM\tilde{S}(\psi'')$ and $\tilde{U}(200\ mb)$ were performed and their first eigenmodes are displayed in Figure 23.

The total variance explained by the first eigenmodes of $RM\tilde{S}(\psi'')$ and $\tilde{U}(200\ mb)$ is 55% and 32%, respectively. As revealed from the $C1[RMS(\psi'')]$ (Figure 23a) and $C1[\tilde{U}(200\ mb)]$ series (Figure 23c), the cyclone activity and zonal flow undergo a coherent interdecadal variation. As for the spatial structure, $E1[RMS(\psi'')]$ (Figure 23b) exhibits a pattern similar to the $RMS[\Delta RM\tilde{S}(\psi'')]$ field (see Figure 22b). The $E1[\tilde{U}(200\ mb)]$ pattern is characterized by flows with opposite direction between the high and low latitudes. The comparison between $E1[RMS(\psi'')]$ and $E1[\tilde{U}(200\ mb)]$ reveals that the significant variability of cyclone activity over the eastern Pacific, North America, and North Atlantic occurs at locations sandwiched by the opposite zonal wind to the north and south sides. In other words, the cyclone activity enhances in association with the increase of the north-south wind shear.

The zonal wind is related to the gradient of

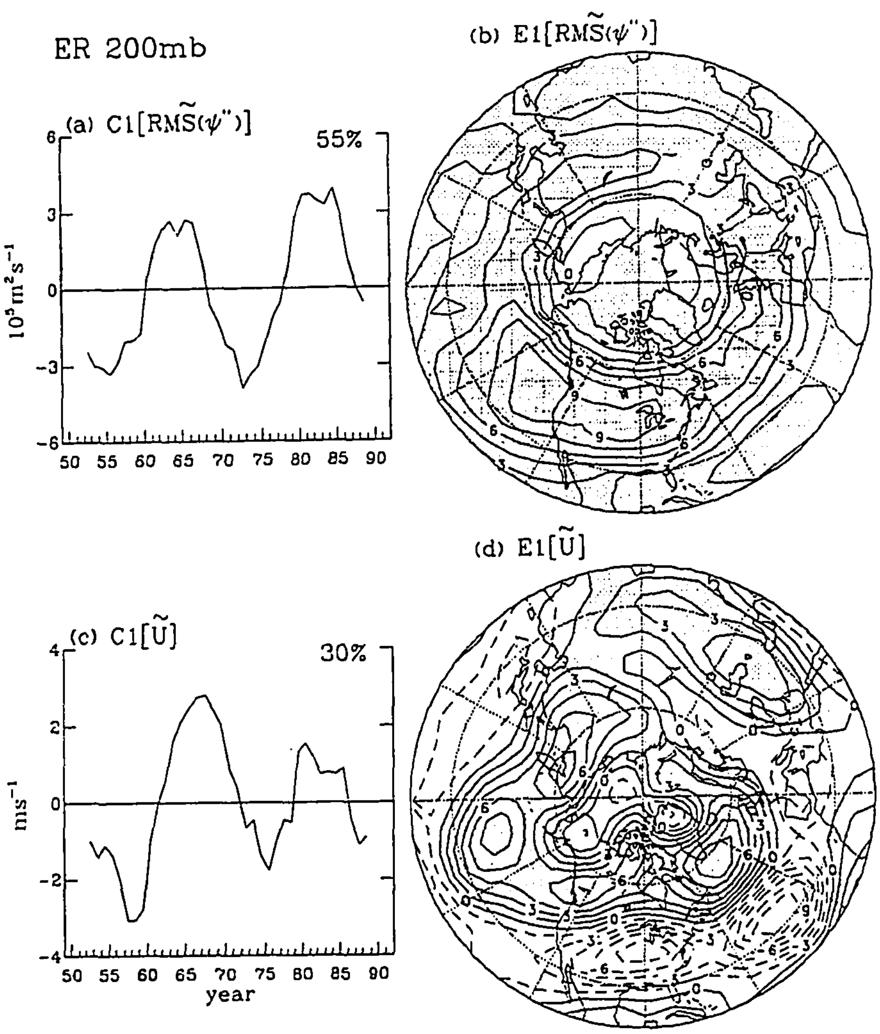

Figure 23. The first eigencoefficient time series/eigenvectors of the interdecadal-change (a)/(b) storm track activity [RMS̃(ψ")] and (c)/(d) zonal wind (Ũ) at 200 mb of the ER experiment. The contour interval of the eigenvector is 0.15. The positive values are lightly shaded and the values larger than 0.45 in (b) are heavily shaded.

streamfunction. Changes in $\tilde{U}$(200 mb) are thus connected to changes in $\tilde{\Psi}$(200 mb). We therefore should compare the EOF analyses of $\tilde{U}$(200 mb) and $\tilde{\Psi}$(200 mb). The temporal variation of C1[$\tilde{U}$(200 mb)] exhibits a coherent oscillation with C1[$\tilde{\Psi}$(200 mb)] (Figure 5a). The maximum centers of E1[$\tilde{U}$(200 mb)] exist at the locations where E1[$\tilde{\Psi}$(200 mb)] (Figure 5b) has the largest north-south gradient. Since the most significant interdecadal change represented by the first eigenmode of $\tilde{\Psi}$(200 mb) is the expansion of the circumpolar vortex, we thus infer that the equatorward expansion of the circumpolar vortex induces changes in the north-south wind shear over the storm track region and consequently induces the variability of the cyclone activity. Therefore, the interdecadal change of the cyclone activity is regulated by the interdecadal change of the atmospheric circulation.

Since the interdecadal changes of transient heat flux and cyclone activity have been analyzed, it is also interesting to examine the relationship between these two interdecadal change fields. The EOF analyses of RM$\tilde{S}$(ψ'') and $\tilde{\chi}_{HFE}$(850 mb) are thus compared. The temporal variations of C1[RM$\tilde{S}$(ψ'')] (Figure 23a) and C2[$\tilde{\chi}_{HFE}$(850 mb)] (Figure 20a) are relatively consistent. As for the spatial pattern, the major positive center of E1[RM$\tilde{S}$(ψ'')] (Figure 23b) over the eastern Pacific/North America coincides with the negative center of E2[$\tilde{\chi}_{HFE}$] (Figure 20c). The comparison between the EOF analyses of $RM\tilde{S}(\psi'')$ and $\tilde{\chi}_{HFE}$ fields reveals that the cyclone activity enhances when the divergence of transient heat flux increases. Since the divergence of transient heat flux is associated with the warm anomaly, one can further infer that the interdecadal variability of the cyclone activity is strengthened by the anomalous warming.

Based upon the analyses of the interdecadal variations of transient heat flux and cyclone activity, it is clear that the interdecadal change of the general circulation statistics is regulated by that of the atmospheric circulation. In the thermal field, the transient heat flux diverges from the warm anomalies into the cold anomalies. In the dynamic field, the cyclone activity over midlatitude storm track regions is affected by the variability of north-south wind shears which are induced by the equatorward expansion of the circumpolar vortex. The aforementioned results answer the fourth questioned proposed in the Introduction.

F. Summary and Discussion

It is hypothesized in this GCM study that the interdecadal SST change is one of the possible mechanisms responsible for the interdecadal variation of the NH winter circulation. In order to test this hypothesis, we performed two multi-decade (1946-92) GCM simulations: the control experiment (EC) using 12 calendar month climatological SSTs over all oceans, and the real-time experiment (ER) incorporating the global real-time SSTs. The GCM used to perform the simulation is the NCAR CCM1 with R15 truncation.

Contrasts between the results of the EC and ER experiments reveal that the interdecadal SST anomalies can induce systematic changes in the NH winter circulation. The most noteworthy systematic changes are: (1) the equatorward expansion of the total circumpolar vortex over the past four decades, (2) the deepening of three climatological troughs, and (3) the existence of three independent interdecadal-variation modes in the stationary eddy field (PNA, PNAW, and NA modes). The aforementioned findings substantiate the claim that the interdecadal SST change is one possible mechanism for the interdecadal variation of the NH winter circulation.

Both the temporal and spatial characteristics of the model interdecadal circulation variability were emphasized in this study. In the ER experiment, the major equatorward expansions of the circumpolar vortex occur over three regions: North Pacific south of Alaska, North Atlantic south of Greenland, and Central Russia. These expansions are accompanied by the deepening of the stationary troughs which is associated with the regionalized anomalous cooling. As for the stationary eddy field, the PNA, PNAW, and NA modes exhibit an equivalent barotropic structure. Horizontally, both the PNA and PNAW modes possess a PNA-like teleconnection pattern over the Pacific and North America region, while the NA mode shows a north-south three-cell structure over the Greenland and North Atlantic region. The temporal variations of the PNA, PNAW, and NA modes consist of a decadal trend and low-frequency (15~20 years) oscillations.

Also of concern to this study are the atmospheric processes involved in maintaining the interdecadal circulation variability. For the total flow field, the equatorward expansion of the total circumpolar vortex was found to possibly result from the cooling over the polar cap which is accompanied by the changes in the north-south differential heating. As for the stationary eddy field, the maintenance of the PNA and PNAW modes were analyzed by the χ-maintenance and ψ-budget analyses. The results from these two analyses demonstrated that the PNA and PNAW modes may result from the following chain processes: (1) the tropical heating anomalies induce the interdecadal change of the divergent circulation, (2) the anomalous divergent circulation interacts with the rotational circulation anomalies to generate two types of $\dot{\psi}_E$ tendency, i.e., $\dot{\psi}_{\chi E}$ and $\dot{\psi}_{AVE}$, and (3) the counterbalance between $\dot{\psi}_{\chi E}$ and $\dot{\psi}_{AVE}$ is the primary mechanism of maintaining/adjusting the ψ_E anomalies. A careful examination of the heating anomalies revealed that the PNA mode may be caused by a seesaw oscillation of the interdecadal diabatic heating anomalies between the Indian Ocean and tropical western Pacific. The cause for the PNAW mode may come from the westward shifting of the positive heating anomalies from the tropical central Pacific to the tropical western Pacific. On the other hand, the extratropical heating anomalies are not important to the maintenance of the PNA and PNAW modes.

In response to the interdecadal change of the atmospheric circulation, the general circulation statistics also exhibit interdecadal variability. In the two-dimension (horizontal) thermal field, the transient heat flux diverges out of the warm anomalies and converges toward the cold anomalies. In the zonal-mean thermal field, the warm anomalies are accompanied by the convergence (divergence) of the standing (transient) component of the meridional eddy sensible heat transport. The opposite situation occurs with the cold anomalies. Moreover, the standing waves are the major agent for the meridional eddy sensible heat transport on the decadal time scale. In the dynamic field, the equatorward expansion of the circumpolar vortex enhances the north-south wind shear around the mid-latitude storm track regions and thus induces the variability of the cyclone activity. In summary, both the interdecadal variations of the transient heat flux and cyclone activity are regulated by the interdecadal change of the atmospheric circulation.

The aforementioned results of the GCM simulations offer a convincing test for the hypothesis that the interdecadal SST change is one possible mechanism for the NH interdecadal circulation variability. Moreover, four major findings were obtained in the GCM study:

(1) The equatorward expansion of the circumpolar vortex is possibly induced by the cooling over the polar cap. This cooling is associated with the change of the north-south differential heating.

(2) Major expansions of the circumpolar vortex are associated with the deepening of the three climatological troughs.

(3) The interdecadal change of the NH winter circulation is primarily induced by the tropical diabatic heating anomalies.

(4) The interdecadal variability of the transient activity is regulated by the interdecadal variation of the atmospheric circulation.

In addition to the dynamic processes involved in the interdecadal variation of the ocean-atmosphere system, other interesting results were found in this study. The total circumpolar vortex shows a tendency for expansion in the ER experiment, but contraction in the EC experiment. As found in the ER experiment, the major equatorward expansion of the circumpolar vortex is related to the deepening of the anomalous lows. In other words, the expansion of the circumpolar vortex is associated with the amplification of the stationary eddies. Conceivably, the contraction of the circumpolar vortex in the EC experiment is possibly related to the weakening of the stationary eddies. One of the known systematic errors in CCM1 is the undersimulation of the stationary eddies. This type of systematic error is also commonly found in the forecast models (e.g., Hollingworth et al. 1980; Arpe and Klinker 1986). As discussed previously, the stationary eddies in the EC experiment become weaker as the simulation proceeds. Thus, the undersimulation of the stationary eddies could result in the contraction of the circumpolar vortex in the EC experiment.

The expansion (contraction) of the circumpolar vortex in the ER (EC) experiment is relatively zonal. One possible explanation for the excessive zonality in the horizontal variation of the circumpolar vortex is the undersimulation of the stationary eddies in the model. This explanation is supported by the results that the model interdecadal circulation variability in the high latitudes is primarily attributable to the zonal-mean flows. In addition to GCM systematic errors such as the undersimulation of the stationary eddies, the external forcing is another factor which affects the simulation results. It was pointed out in observational studies (e.g., Chen and Chen 1994) that the contraction of the circumpolar vortex in the past four decades is most significant over two regions: northern North America and northern Asia. The surface temperature over these two regions exhibit a warming trend which is related to the decrease of arctic sea ice extent (Chapman and Walsh 1994). Combining the results of the above two studies, one can infer that the contraction of the circumpolar vortex is connected to the retreat of the arctic sea ice. In the CCM1, the sea ice is prescribed with its 12 calendar month climatological means. The lack of sea ice variability over the Arctic may cause a failure in the simulation of the contraction of the circumpolar vortex over northern lands in the ER experiment.

As for the interdecadal variation of stationary eddies, Graham et al. (1994) compared three parallel 18-year (1970-88) GCM experiments incorporating the SST changes over (1) tropics only, (2) midlatitudes only, and (3) entire globe. They interpreted the model results as suggesting that the circulation changes over the North Pacific are primarily a response to changes in the tropical SSTs. Their interpretation is consistent with the findings in this study that the PNA and PNAW modes may result from the response of the atmospheric circulation to the interdecadal change in the tropical heating. By conducting a real-time SST experiment for the years 1969-1990, Kitoh (1991) reported a GCM's systematic bias on the simulated interdecadal changes as an overreaction to the SST changes surrounding Indonesia. This systematic bias seems to be a possible mechanism for the PNAW mode found in the ER experiment. This is because: (1) the PNAW mode is possibly induced by the westward shift of the tropical heating anomalies from the central Pacific to the vicinity of Indonesia, and (2) the PNA and NA modes exist in both the model and in observations, but the PNAW mode is only detected in the model.

As for the transient eddy activity, the interdecadal variation of the cyclone activity is significant in three regions: eastern Pacific, North America, and eastern Atlantic. Over these three regions, The variability of the cyclone activity is related to the changes of the north-south wind shear. Chen and Chen (1994) analyzed the observational data and found that the interdecadal variability of the cyclone activity exhibits a southward shift thus following the equatorward migration of the North Pacific jet streams. Apparently, the interdecadal changes of cyclone activity in the model and in the observations are generated from different mechanisms. One possible factor which may affect the cyclone activity simulated in the model is the model resolution. In other words, the R15 horizontal resolution could be too coarse for the CCM1 to properly simulate the real cyclone activity.

IV. LINEARIZED MODEL EXPERIMENT

A. Introduction

It was demonstrated in the GCM study that the interdecadal SST changes can possibly induce the interdecadal change of the NH winter circulation. As far as the dynamic processes related to the interdecadal circulation variability are concerned, there were three major findings in the GCM study. *First*, the equatorward expansion of the total circumpolar vortex is possibly induced by the cooling over the polar cap. In association with the polar cooling, the north-south differential heating changes. *Second*, the interdecadal variation of the stationary eddies is primarily induced by the tropical heating anomalies, while the extratropical heating anomalies do not seem to be important. *Third*, the interdecadal change of general circulation statistics is the response, not the cause, of the interdecadal variation of the atmospheric circulation. From the third finding, one can infer that the transient forcing anomalies are not vital to the interdecadal circulation variability. Based upon the three findings obtained from the GCM studies, three implications are derived:

(A) The interdecadal heating anomalies are more important than the interdecadal transient forcing anomalies to the maintenance of the interdecadal change of the NH winter circulation (hereafter referred to as Finding A).

(B) The interdecadal tropical heating anomalies are more important than the interdecadal extratropical heating anomalies to the maintenance of the interdecadal change of the NH winter circulation (hereafter referred to as Finding B).

(C) Changes in north-south differential heating (or polar cooling) is one possible mechanism for the NH interdecadal climate change (hereafter referred to as Finding C).

However, these three dynamic processes need to be verified. One way to test the dynamic processes inferred from the GCM experiment is to conduct a linearized model experiment. By examining the response of the linearized model to a particular component of the anomalous forcings obtained from the GCM experiment, one can distinguish the relative contribution of different individual processes to the total GCM response. This model diagnostic technique has been successfully implemented to diagnose climatological stationary waves (Nigam et al. 1986,1988), as well as the forced low-frequency circulation anomalies (e.g., Branstator 1992; Ting and Lau 1993). In order to verify the dynamic processes revealed in Findings A, B, and C, we performed the present linearized model study.

There were four experiments in the linearized model study. The first experiment, i.e., control run, was used to examine the performance of the linearized model in order to establish confidence in the model's ability to reasonably simulate the atmosphere climate. The steady-state response of the model circulation to the multi-winter (1950-92) mean heating forcing was investigated in this experiment.

Finding A was used as the hypothesis and thus tested in the second experiment, i.e., diabatic heating versus transient forcing. In this experiment, the interdecadal changes of the model circulation induced by the diabatic heating anomalies and transient eddy forcing anomalies were compared. With this comparison, the relative roles of diabatic heating anomalies and transient forcing anomalies to the interdecadal circulation variability were evaluated.

Finding B was used as the hypothesis in the third experiment, i.e., tropical heating versus extratropical heating. The relative importance of the tropical heating anomalies and extratropical heating anomalies to the interdecadal change of the atmospheric circulation was examined from the response of the model circulation to these two heating anomalies.

In view of the Finding C, we designed the fourth experiment, i.e., north-south differential heating, to examine the effect of the polar cooling on the NH winter circulation variability. The effect of the polar cooling was interpreted from the response of the model circulation to an ideal zonal-mean heating anomaly.

The overall plan for the linearized model study is outlined as follows. Section B gives a description of the linearized model used in the study. The designs and purposes of the different experiments and the forcings used in these experiments are documented in section C. Illustrated in section D are the results of the linearized model experiments. The summary and discussion of this study are contained in section E.

B. The Model

A nine-level σ-coordinate primitive-equation (PE) model, which was originally formulated by Branstator (1990) and later modified by Tzeng and Chen (1990), was adopted to perform the designated experiments. Its formulation is derived from the R15 resolution CCM1. Tzeng and Chen linearized this model in time and allowed it to explicitly forecast the perturbation (anomalous) mode. There is one advantage to use this linearized model in the present study. The effect of discretization need not be of concern because the linearized model's numerics are identical to those of the

CCM1. On the other hand, the linearized model has a deficiency. The feedback processes between the mean state and transient activity can not be simulated in the model because the model is linearized in time. The governing equations of the modified PE model are:

(a) the transient vorticity equation

$$\frac{\partial \zeta'}{\partial t} = \frac{1}{a(1-\mu^2)} \times \frac{\partial M_v}{\partial \lambda} - \frac{1}{a} \times \frac{\partial M_u}{\partial \mu} - \alpha_\zeta \zeta' + K_H \nabla^2 \zeta' + K_v \frac{\partial^2 \zeta'}{\partial \sigma^2} + R_\zeta,$$

(b) the transient divergence equation

$$\frac{\partial \delta'}{\partial t} = \frac{1}{a(1-\mu^2)} \times \frac{\partial M_u}{\partial \lambda} + \frac{1}{a} \times \frac{\partial M_v}{\partial \mu} - \alpha_\delta \delta' + K_H \nabla^2 \delta' + K_v \frac{\partial^2 \delta'}{\partial \sigma^2}$$

$$-\nabla^2 (\Phi' + R\overline{T}_0 q' + E') + R_\delta,$$

(c) the transient thermodynamic equation

$$\frac{\partial T_1'}{\partial t} = \frac{-1}{a \cdot \cos\phi} \times \frac{\partial}{\partial \lambda} (\overline{u} T_1' + u' \overline{T}_1) - \frac{\cos\phi}{a} \times \frac{\partial}{\partial \mu} (\overline{v} T_1' + v' \overline{T}_1)$$

$$+\delta' \overline{T}_1 + \overline{\delta} T_1 - \overline{\sigma} \frac{\partial T_1'}{\partial \sigma} - \dot{\sigma}' \frac{\partial \overline{T}_1}{\partial \sigma} - \dot{\sigma}' \frac{\partial \overline{T}_0}{\partial \sigma} - \alpha_T T_1' + \frac{\dot{q}}{C_p}$$

$$+\kappa T_1' \left(\frac{\overline{\omega}}{p}\right) + \kappa \overline{T}_1 \left(\frac{\omega}{p}\right)' + \kappa \overline{T}_0 \left(\frac{\omega}{p}\right)' + K_T \nabla^2 T_1' + \frac{K_v}{\sigma^2} \nabla^2 \left(\frac{T_1'}{\sigma^k}\right) + R_T,$$

(d) the transient continuity equation

$$\frac{\partial q'}{\partial t}=-\delta'\overline{q}-\hat{V}'\cdot\nabla\overline{q}-\overline{V}\cdot\nabla q'+R_{q'}$$

(e) the transient hydrostatic equation

$$\Phi'=-\int_1^\sigma R\frac{T_1'}{\sigma}\,d\sigma\,,$$

where

μ=sinϕ, ϕ=latitude, λ=longitude, a=radius of earth,

q=ln P_s,

$$\dot{\sigma}=\sigma\int_0^1(\delta+V\cdot\nabla q)\,d\sigma-\int_0^\sigma(\delta+V\cdot\nabla q)\,d\sigma\,,$$

$$\frac{\omega}{p}=V\cdot\nabla q-\frac{1}{\sigma}\int_0^\sigma(\delta+V\cdot\nabla q)\,d\sigma\,,$$

$$T_1(\lambda,\mu,\delta,t)=T(\lambda,\mu,\delta,t)-T_0(\sigma)\,,$$

$$M_u=[\zeta'\overline{v}+(\overline{\zeta}+f)\,v'-\frac{R}{a\cdot\cos\phi}\,(\overline{T}_1\frac{\partial q'}{\partial\lambda}-T_1'\frac{\partial\overline{q}}{\partial\lambda})-\overline{\dot{\sigma}}\frac{\partial u'}{\partial\sigma}-\dot{\sigma}'\frac{\partial\overline{u}}{\partial\sigma}]\cos\phi\,,$$

$$M_v=[-\zeta'\overline{u}+(\overline{\zeta}+f)\,u'-\frac{R}{a}\,(\overline{T}_1\frac{\partial q'}{\partial\phi}-T_1'\frac{\partial\overline{q}}{\partial\phi}-\overline{\dot{\sigma}}\frac{\partial v'}{\partial\sigma}-\dot{\sigma}'\frac{\partial\overline{v}}{\partial\sigma}]\cos\phi\,,$$

$$\kappa=\frac{R}{C_p}\,,$$

$\hat{x}=\int_0^1 x d\sigma,$

$\hat{x}^{\sigma}=\int_0^{\sigma} x d\sigma,$

$\alpha_\zeta, \alpha_\delta, \alpha_T, \alpha_q$ = dissipative terms,

( ) = ($\bar{\ }$) + ( )', ($\bar{\ }$) = time mean, ( )' = deviation from time mean;

the notations used here are conventional.

The residual (anomalous perturbation covariance) terms (R_ζ, R_δ, R_T, R_q) are expressed as follows:

$$R_\zeta=-\frac{1}{a(1-\mu^2)}\frac{\partial}{\partial\lambda}[-\overline{\zeta'u'}-\frac{R}{a}\overline{T_1'\frac{\partial q'}{\partial\phi}}-\overline{\dot{\sigma}'\frac{\partial v'}{\partial\sigma}}]\cos\phi$$

$$+\frac{1}{a}\frac{\partial}{\partial\mu}[\overline{\zeta'v'}-\frac{R}{a\cos\phi}\overline{T_1'\frac{\partial q'}{\partial\lambda}}-\overline{\dot{\sigma}'\frac{\partial u'}{\partial\sigma}}]\cos\phi,$$

$$R_\delta=\frac{-1}{a(1-\mu^2)}\frac{\partial}{\partial\lambda}[\overline{\zeta'v'}-\frac{R}{a\cos\phi}\overline{T_1'\frac{\partial q'}{\partial\lambda}}-\overline{\dot{\sigma}'\frac{\partial u'}{\partial\sigma}}]\cos\phi$$

$$-\frac{1}{a}\frac{\partial}{\partial\mu}[-\overline{\zeta'u'}-\frac{R}{a}\overline{T_1'\frac{\partial q'}{\partial\phi}}-\overline{\dot{\sigma}'\frac{\partial v'}{\partial\sigma}}]\cos\phi,$$

$$R_T=\frac{1}{a\cos\phi}\frac{\partial}{\partial\lambda}\overline{u'T'}+\frac{\partial}{a\partial\mu}(\overline{v'T'}\cos\phi)$$

$$-\overline{T_1'\delta'}+\overline{\dot{\sigma}'\frac{\partial T'}{\partial\sigma}}-\kappa\overline{T_1'(\frac{\omega}{p})'},$$

$$R_q=\overline{\hat{V}'\cdot\nabla q'}.$$

In this study, the linearized model incorporates two types of forcings: diabatic heating and transient forcing. Both the diabatic heating and transient forcing are obtained from the ER experiment. The transient forcings are expressed in terms of the four anomalous perturbation covariance terms (R_ζ, R_δ, R_T, R_q). The Rayleigh friction (α_R) and Newtonian damping (α_N) along with the diffusion coefficients in the horizonal (K_H) and in the vertical (K_V) at different σ-level are listed in Table 1. For a more detailed description of this model, readers are referred to Tzeng and Chen (1990).

C. Experiments and Forcings

In order to verify Findings A, B, and C inferred from the GCM study, we conducted four linearized model experiments. The purpose, hypothesis, and design of these experiments, as well as the forcing anomalies used in these experiments, are discussed as follows.

Table 1. The horizonal and vertical diffusion coefficient at σ-level

	σ	α_R	e^{-1} time of α_R	α_N	e^{-1} time of α_N	K_H	K_V
		(10^{-7})	(days)	(10^{-7})	(days)	(10^{5})	(10^{-9})
1	.009	30	4	15	8	4.5	3.5
2	.060	30	4	15	8	4.5	3.5
3	.165	10	12	15	8	3.5	3.5
4	.355	10	12	15	8	7	8
5	.500	10	12	15	8	7	8
6	.664	10	12	15	8	7	8
7	.811	10	12	30	4	10	12
8	.926	30	4	60	2	10	12
9	.991	60	2	60	2	12	16

units of α_R, α_N, and K_V are s^{-1}; and K_H is m^2s^{-1}.

1. Control run

The purpose of this experiment was to ensure that the linearized model could appropriately simulate the atmosphere climate. To perform the control run, the linearized model was forced by the multi-winter (1950-92) mean diabatic heating extracted from the ER experiment. The horizontal structure of this heating forcing is illustrated by the vertically-integrated mean heating ($\overline{H}_I$) in Figure 24a. As shown by the $\overline{H}_I$ field, the major heating centers are located in the tropics over the three tropical continents, the Intertropical Convergence Zone, and the South Pacific Convergence Zone. In the midlatitudes, the heating centers are located in the two storm track regions. The $\overline{H}_I$ field exhibits a spatial structure consistent with the observational winter mean heating field computed by Chen and Baker (1986). To depict the vertical structure of the heating forcing, the longitude-height distribution of the tropical heating averaged between the 16°S-2°S is shown in Figure 24b. The tropical heating exhibits a cold bias below 850 mb. Its amplitude reaches a maximum in the middle troposphere with the center at about 500 mb. The heating maxima over equatorial Africa, the central Pacific, and South America are associated with the three upward branches of the east-west Walker circulation as discussed by Chen et al. (1993).

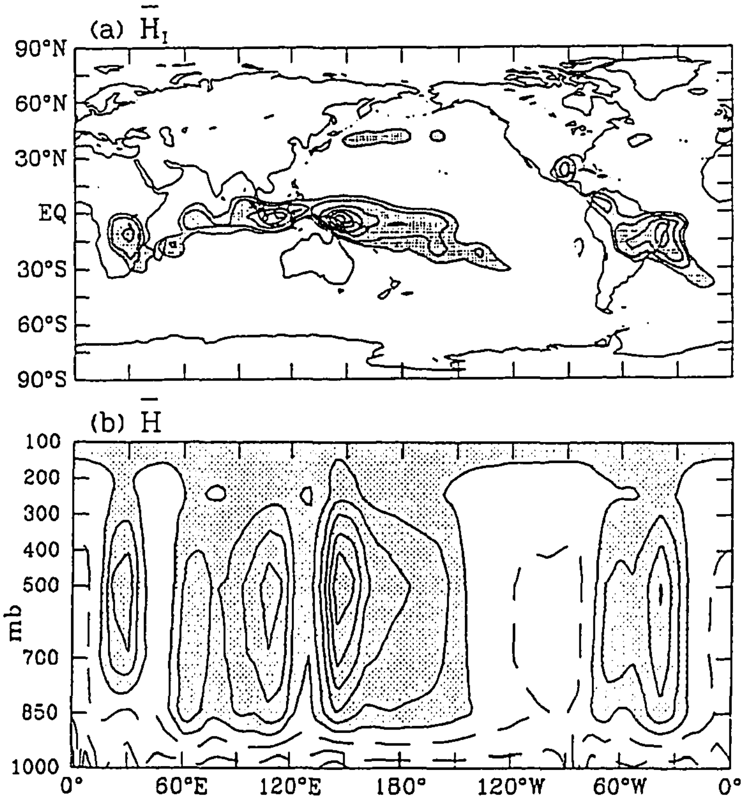

Figure 24. The heating forcing used to perform the climate simulation experiment. This heating forcing is obtained from the multi-winter (1950-92) mean heating field of the ER experiment. Its horizontal structure is depicted by its vertically-integrated component in (a). Its vertical structure is portrayed by the vertical distribution of the tropical heating centers averaged between 16°S-2°S in (b). In (a), the contours are ..... -3, -2, -1, -0.5, 0, 0.5, 1, 2, 3, 4, ... °day^{-1} and the values larger than 0.5 °day^{-1} are shaded. In (b), the contour interval is 1 °day^{-1} and the positive values are shaded.

2. Diabatic heating versus transient forcing

The purpose of this experiment was to test the hypothesis that the interdecadal diabatic heating anomalies are more important than the interdecadal transient forcing anomalies in the maintenance of the interdecadal change of the NH winter circulation. In order to test this hypothesis, the forcing anomalies averaged from winters 1950-59 (1980-89) were imposed on the control run to conduct a 1950s (1980s) perpetual simulation. The difference between the simulated circulation of the 1950s and 1980s perpetual simulations is interpreted as the interdecadal climate change induced by the forcing anomalies used in these simulations. By comparing the interdecadal variability of the model circulation generated by the diabatic heating and transient forcing anomalies, we can test the hypothesis of this experiment. The above approach of analyzing the interdecadal circulation variability by conducting the perpetual simulations is adopted from Chen et al.'s (1992) study. The perpetual simulations forced by the diabatic heating (transient forcing) anomalies are hereafter referred to as the diabatic heating (transient forcing) experiment.

The diabatic heating and transient forcing anomalies were obtained from the following procedures. For the diabatic heating field, the entire 43-year (1950-92) monthly-mean fields were subjected to least-square-fit analysis to extract out their decadal trend component. After removing the decadal trend component, the remainder of the anomalous fields were bandpass (7-43 year) filtered to isolate the low-frequency component. The combination of the decadal trend and low-frequency components forms the interdecadal variation component. The 1950s (1980s) anomalous forcings were obtained from the averages of the interdecadal variation components for the winters 1950-59 (1980-89).

The transient forcing anomalies, which are referred to as the anomalous perturbation covariance terms (R_ζ, R_δ, R_T, R_q) derived from this model's transient PE system, were obtained with a process slightly different from that for the diabatic heating anomalies. We computed the transient forcing with the GCM daily data and then calculated the time-average to obtain the transient forcing in each season. The seasonal-mean transient forcing field was then subjected to the least-square-fit and bandpass filter analyses to obtain the transient forcing anomalies in the same way as that described in the procedure of deriving the diabatic heating anomalies.

The 1950s- and 1980s- diabatic heating anomalies obtained and processed according to the above procedures from the ER experiment are shown in Figure 25. The horizontal structure of the 1950s H_I anomaly (figure 25a) exhibits centers of heating maxima over the tropics. The positive centers are over equatorial western Africa, equatorial central Pacific,

Figure 25. As in Figure 24, except for the heating anomalies used to perform the diabatic heating experiment. The heating anomalies are obtained from the departures of the 1950-59 [(a)-(b)] and 1980-89 [(c)-(d)] winter averaged heating field from the multi-winter mean heating field. In (a) and (c), the contour interval is 0.1 $^{\circ}day^{-1}$ and the values larger (smaller) than 0.1 (-0.1) $^{\circ}day^{-1}$ are heavily (lightly) shaded. In (b) and (d), the contour interval is 0.1 $^{\circ}day^{-1}$ and the positive values are shaded.

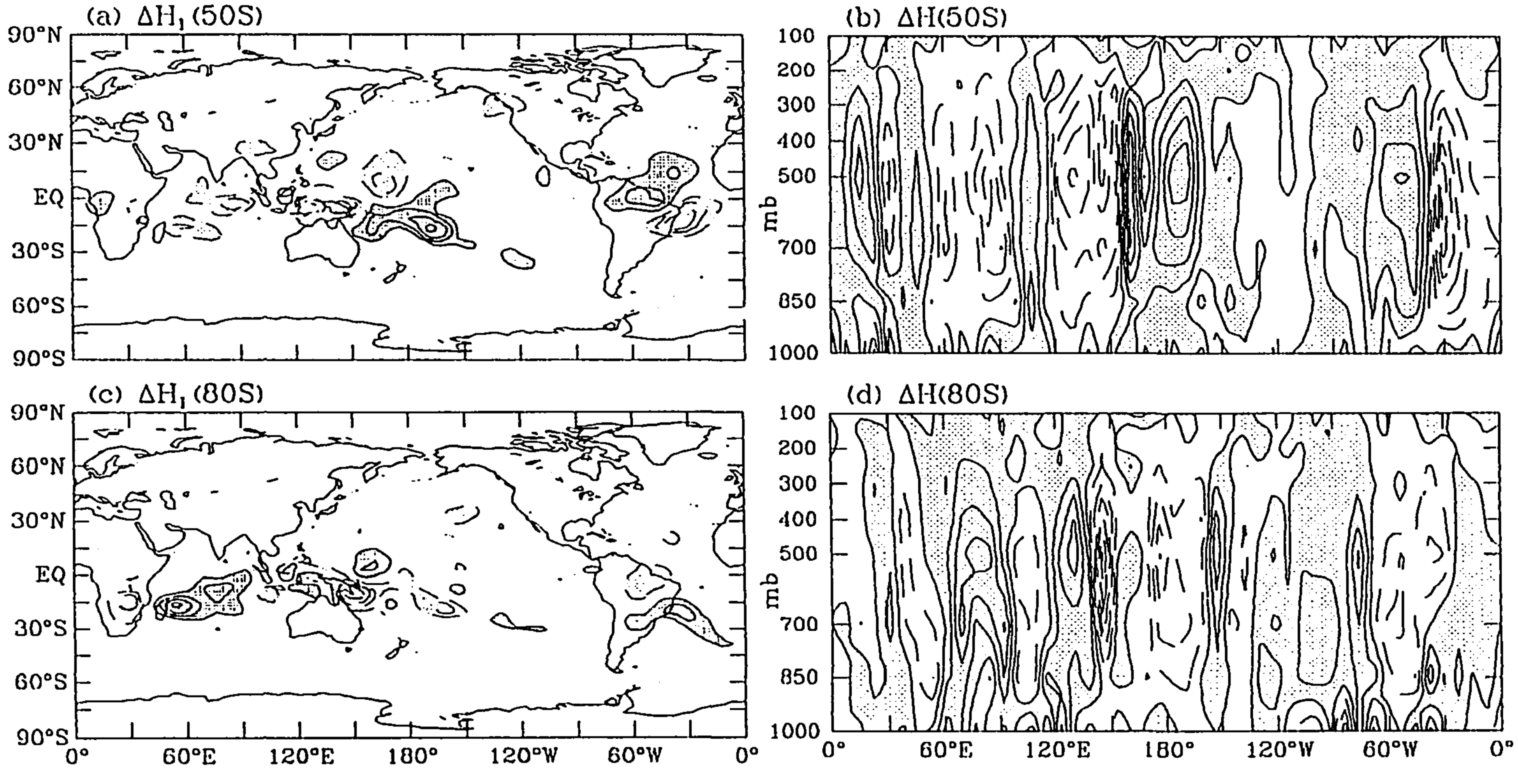
(a) ΔH_1(50S)
(b) ΔH(50S)
(c) ΔH_1(80S)
(d) ΔH(80S)
90°N
60°N
30°N
EQ
30°S
60°S
90°S
0°
60°E
120°E
180°
120°W
60°W
0°
100
200
300
400
500
700
850
1000
mb

and the Amazon Basin. The negative centers are located over the Indian Ocean, equatorial western Pacific, and east of Brazil. The vertical structure of the tropical heating centers for the 1950s H_I anomaly is illustrated in Figure 25b. It is clear that the maxima of the 1950s tropical heating anomaly occur in the middle troposphere around 400 mb and 500 mb. To a great extent, the horizontal and vertical structures of the 1980s heating anomaly (Figures 25c-d) are opposite to those of the 1950s heating anomaly.

As for the transient forcing anomalies, the 1950s anomalies of R_ζ(850 mb), R_δ(850 mb), R_T(850 mb), and R_q are displayed in Figure 26. In contrast to the diabatic heating anomalies, the transient forcing anomalies exhibit major centers in the mid- and high-latitudes. Although the horizontal structures of the transient forcing anomalies are somewhat noisy, a dynamic relationship between these four transient forcing anomalies still can be found. For example, in the vicinity of Alaska, the R_ζ and R_δ anomalies exhibit positive centers, while the R_T and R_q anomalies show negative centers. This relationship implies that: a warming tendency ($R_T > 0$) causes the air mass to ascend and results in the horizontal convergence of air mass ($R_\delta < 0$) as well as the decrease of the pressure ($R_q < 0$); the decrease of the pressure induces the deepening of the anomalous low so as to generate the positive vorticity tendency ($R_\zeta > 0$). However,

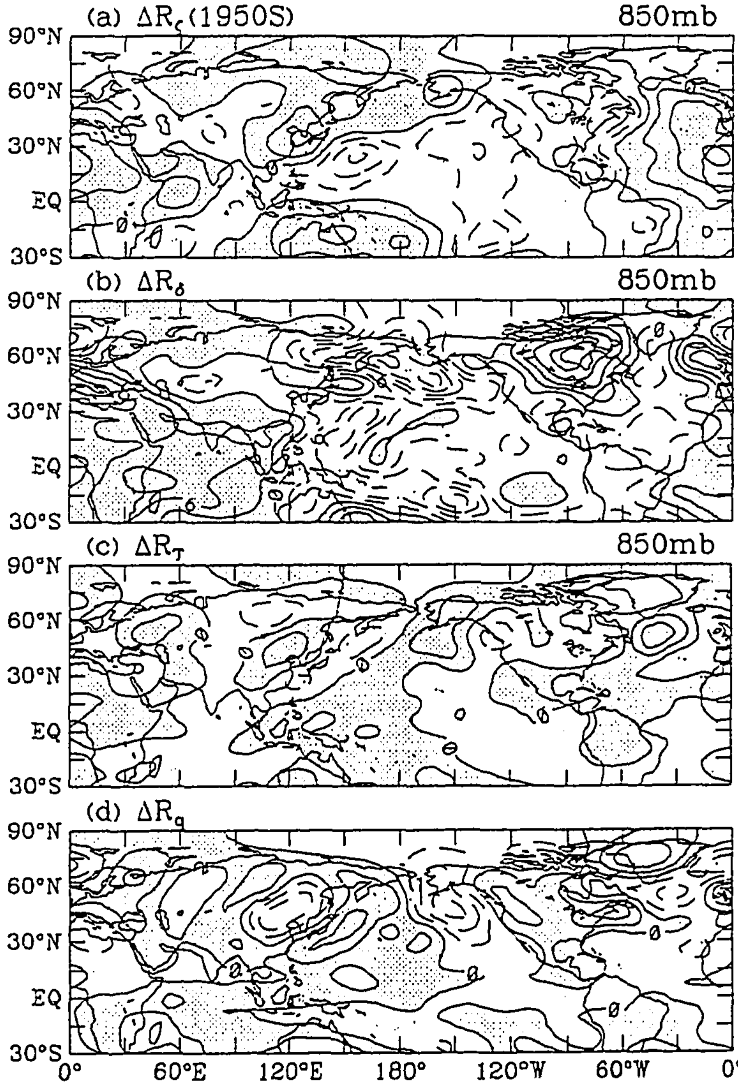

Figure 26. The 1950s transient forcing anomalies used to perform the transient forcing experiment. The contour intervals are 0.3 s^{-2} for (a) R_ζ(850 mb), 0.3 s^{-2} for (b) R_δ(850 mb), 0.03 $^oKs^{-1}$ for (c) R_T(850 mb), and $5x10^{-10}$ mbs^{-1} for (d) R_q. The positive values are shaded.

the aforementioned dynamic relationship does not apply well to every anomalous center. The 1950s transient forcing anomalies at 200 mb (Figure 27) also exhibit a noisy pattern. It seems that there is no clear systematic relationship between the 850 mb and 200 mb transient forcing anomalies. The 1980s transient forcing anomalies at 200 mb and 850 mb are to a great extent opposite to their 1950s counterparts and thus are not shown here.

3. Tropical heating versus extratropical heating

This experiment was designed to test the hypothesis that the interdecadal tropical heating anomalies are more important than the interdecadal extratropical heating anomalies to the interdecadal variation of the NH winter circulation. Using a similar approach as that described in the second experiment, the effect of the tropical and extratropical heating anomalies on the NH interdecadal circulation variability was examined in terms of the difference between the perpetual simulations forced by the 1950s and 1980s heating anomalies. Both tropical and extratropical heating anomalies used in this experiment (not shown) are modified from the diabatic heating anomalies used in the diabatic heating experiment (Figure 25) by doubling the amplitudes of the latter field's tropical (30°S-30°N) and extratropical (north of 30°N) centers, respectively. The

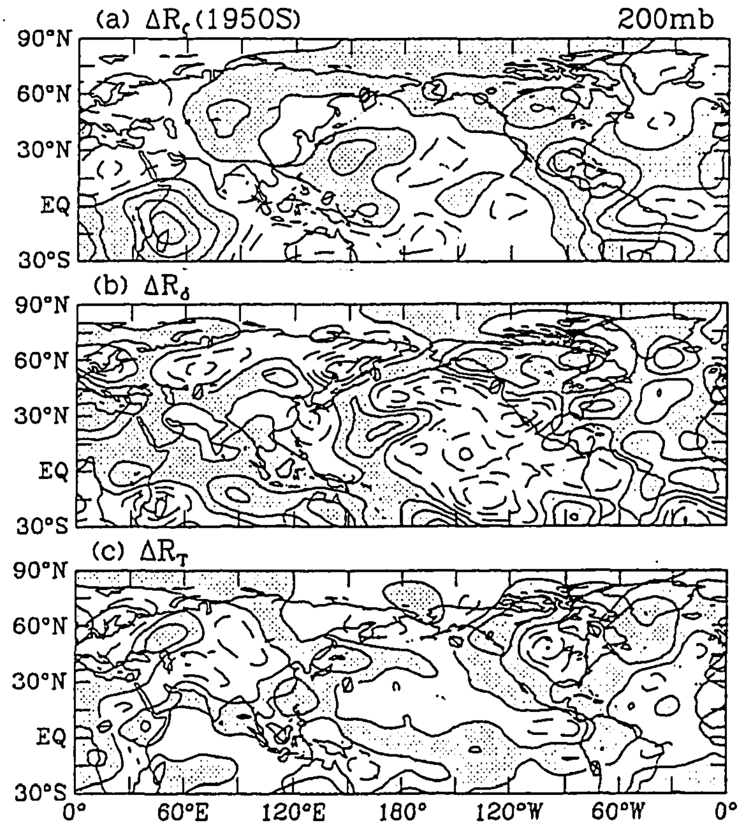

Figure 27. The 1950s transient forcing anomalies at 200 mb used to perform the transient forcing experiment. The contour intervals are 1 s^{-2} for (a) R_ζ, 1 s^{-2} for (b) R_δ, and 0.03 $^{\circ}Ks^{-1}$ for (c) R_T. The positive values are shaded.

locations of the tropical and extratropical centers referred to in this section were chosen as the centers of RMS[$\Delta\tilde{H}_I$] (not shown). The RMS[$\Delta\tilde{H}_I$] field has tropical centers from Africa to the central Pacific and over South America within the 30°S-30°N band, and extratropical centers over the two midlatitude storm tracks. The perpetual simulations forced by the aforementioned tropical (extratropical) heating anomalies are hereafter referred to as the tropical (extratropical) heating experiment.

4. North-south differential heating

It was shown in the GCM study that the equatorward expansion of the circumpolar vortex is possibly induced by polar cooling which is accompanied by the changes in north-south differential heating. We thus designed this experiment to examine the effect of polar cooling on the interdecadal climate variability. The polar cooling simulated in the GCM was revealed from the change of vertically-integrated zonal-mean heating from the 1950s to the 1980s, which is about 0.1°day^{-1} at the equator and -0.1°day^{-1} at the North Pole (Figure 28a). We then doubled the GCM's decadal heating change and construct an ideal horizontal zonal-mean heating anomaly with the value of 0.2°day^{-1} at the equator and -0.2° day^{-1} at 90°N. The values at the remaining NH latitudes were obtained from linear interpolation. To the south of the

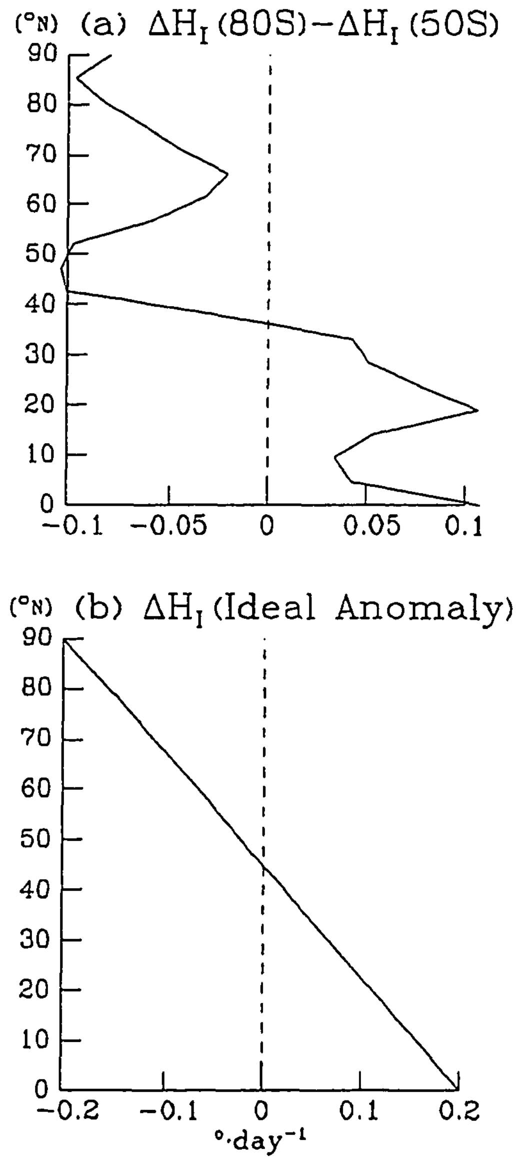

Figure 28. (a) The interdecadal change of the vertically-integrated zonal-mean heating (1980s-1950s) of the ER experiment. (b) The ideal zonal-mean heating anomalies used in the north-south differential heating experiment. This ideal heating anomaly is designed to mimic the polar cooling.

equator, the ideal heating anomaly is zero. The vertical structure of this ideal heating anomaly is a sinusoidal function with the maximum of 1 at 500 mb and minima of 0 at the top and bottom of the model atmosphere. This ideal heating anomaly and one with the opposite sign were added to the 1980s and 1950s diabatic heating anomalies used in the diabatic heating experiment, respectively. After the summation, the new diabatic heating anomalies were imposed on the control run to perform two perpetual simulations. The difference of these two simulations can reveal the effect of the ideal zonal-mean heating anomalies as well as the polar cooling on the interdecadal climate change.

In the above four experiments, the basic state of the linearized model was specified from the zonal-mean components of the climatological winter circulations of the ER experiment. The multi-winter mean total surface pressure field was prescribed in the model to represent the function of the topography. Every simulation began with an infinitesimal perturbation specified as 1/1000 of the basic state and the integration interval was one hour.

Before the linearized model can be employed to perform the experiments, we should examine the basic characteristics of the model. For example, (1) can baroclinic instability occur in the model with the basic states derived from the GCM climatologies? In addition, (2) is the specification of climatological total surface pressure field an appropriate way to represent the function of the orography in the model? To answer the first question, we perturbed the model zonal-mean basic states with the random eddy perturbations in an inviscid condition. After integrating for several days, the model circulation (not shown) exhibited a short-wave train (consisting primarily of wavenumbers 7-8) along 40°N. This short-wave train proceeded to amplify and propagate eastward. The aforementioned results suggest the occurrence of baroclinic instability in the model.

In order to examine the second question listed above, we conducted a perpetual experiment similar to that used to test the occurrence of baroclinic instability with the exception that: (1) the zonal-mean surface pressure field was replaced by the total surface pressure field, and (2) the dissipation and diffusion effects were included in the model. After integrating for 20 days, the model eddy streamfunction field at 200 mb (not shown) exhibited a large-scale pattern somewhat similar to that of the climatological stationary eddies, with the exception that the amplitude of the former was only 15~20% as large as that of the latter. This weak amplitude of orographically forced waves has been reported in Held's (1982) linearized model study relative to the maintenance of stationary eddies. Thus, based upon the similarity of the large-scale pattern between the forced waves in the present simulation and the climatological stationary eddies at 200 mb, we feel that we are justified in representing orography in our linearized model by specifying the total surface pressure field.

D. Results

In order to evaluate the results of the linearized model simulations, we need to compare them with the results of the GCM study. It was shown in the GCM study that the interdecadal change of stationary eddies can be effectively used to illustrate the interdecadal variation of the NH winter circulation. For this reason, we use the interdecadal change of stationary eddies to verify the linearized model simulations. To depict the interdecadal change of stationary eddies simulated in the GCM, the change of ψ_E field in the ER experiment from the 1950s mean to the 1980s mean, i.e., $\Delta\psi_E$(80s-50s), at 200 and 850 mb are displayed in Figure 29. By using the GCM $\Delta\psi_E$(80s-50s) fields shown in Figure 29 as the standard-of-comparison, we thus can evaluate the interdecadal change of stationary eddies simulated by the linearized model experiments.

GCM(ER)

(a) $\Delta\psi_E$(200mb)(80S−50S)

(b) $\Delta\psi_E$(850mb)(80S−50S)

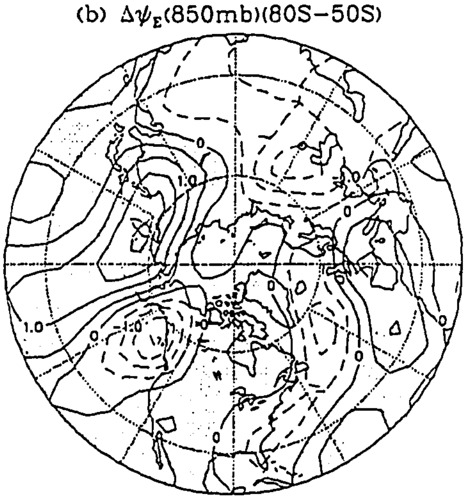

Figure 29. The interdecadal change (1980s-1950s) of eddy streamfunction at (a) 200 mb and (b) 850 mb of the GCM(ER) experiment. The contour intervals are 10^6 m^2s^{-1} for (a) and $5x10^5$ m^2s^{-1} for (b). The positive values are shaded.

1. Control run

In order to examine the model's performance in simulating the atmospheric climate, a 40-day perpetual run was conducted with the forcing of the multi-winter (1950-92) mean diabatic heating. One may question whether the 40-day simulation is too short to test the model's performance. However, as revealed by the temporal variation of this climate simulation's global-averaged kinetic energy over the entire atmospheric column (Figure 30a), the linearized model has reached equilibrium after about day 25. In fact, we also conducted a 90-day perpetual run with the same mean heating forcing and found that the model remains in equilibrium after day 25. In addition, the simulated circulation averaged from the last 10 days of the 40-day run does not differ noticeably from that averaged over the last 60 days of the 90-day run. Thus, the 40-day perpetual run should be sufficient to examine the model's performance. The model climate is represented by the 200 and 850 mb stationary eddies obtained from the last 10-day mean fields of the present simulation (Figure 30). Hereafter, all of the linearized model simulations discussed here were integrated for 40 days. The model circulation obtained from the last 10-day mean field of the simulation was then used for the diagnostic analyses.

To verify the atmospheric climate simulated by the linearized model, we compare the ψ_E(200 mb) and ψ_E(850 mb)

Control run

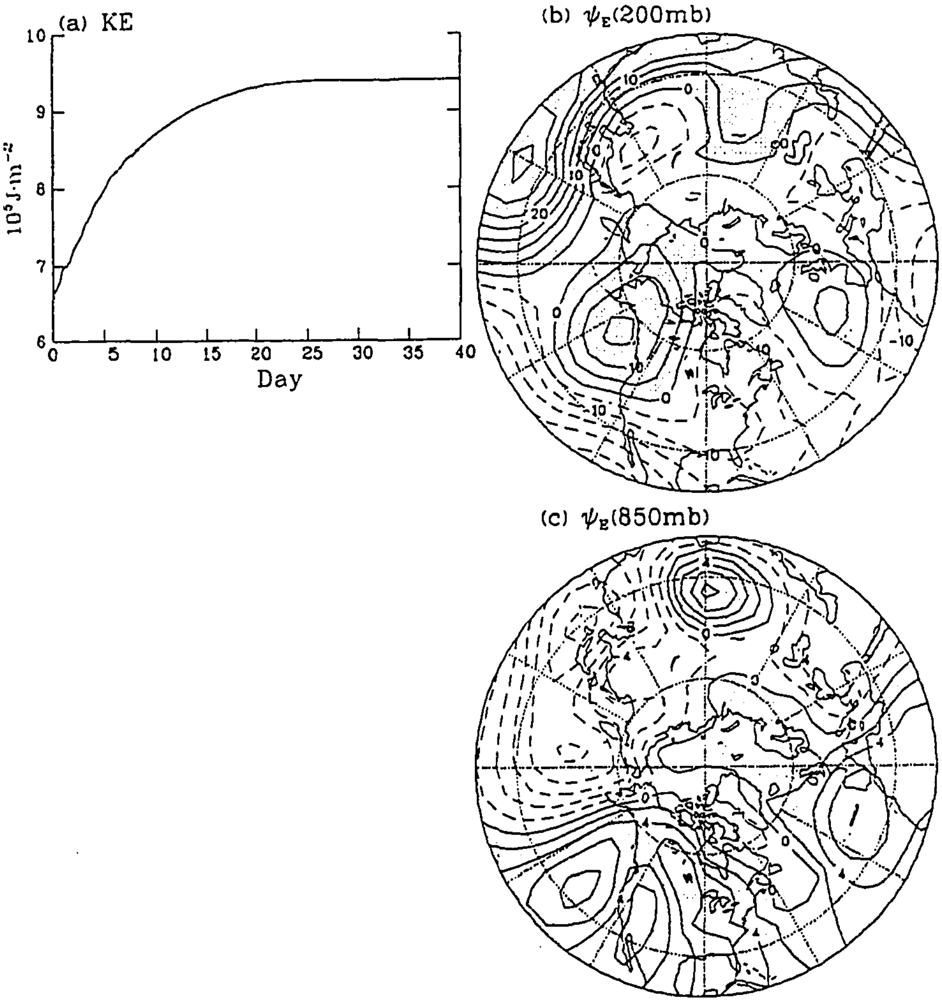

Figure 30. The results of the control run: (a) The temporal variation of the global average kinetic energy, the steady states of the (b) 200 mb eddy streamfunction, and (c) 850 mb eddy streamfunction. The contour intervals are (b) $5 \times 10^6\ m^2 s^{-1}$ and (c) $2 \times 10^6\ m^2 s^{-1}$. The positive values in (b) and (c) are shaded.

fields generated by the control run in Figure 30 with the $\overline{\Psi}_E$(200 mb) and $\overline{\Psi}_E$(850 mb) fields from the ER experiment in Figure 1, respectively. In the upper troposphere, the major ridges and troughs at high latitudes are well reproduced at the proper locations by the linearized model. At low latitudes, the linearized model simulation fails to capture the subtropical ridge southeast of North America. This result is relevant to the undersimulation of the ridge over the eastern Atlantic and the overexpansion of the trough over the east coast of North America. In the lower troposphere, the salient features of climatologic stationary eddies are adequately simulated by the linearized model. However, the Siberian high is oversimulated on the south side of its climatological location, and the ridge over the west coast of North America splits into several cellular structures.

To objectively assess the model performance, we calculated the spatial correlation coefficient between the mean stationary eddies simulated in the GCM (Figure 1) and in the control run with the domain poleward of 20°N. The correlation is 0.70 for the lower-tropospheric circulation and 0.81 for the upper-tropospheric circulation. Apparently, the upper circulation can be simulated better by the linearized model. Since the heating is one of several possible mechanisms for maintaining the NH winter stationary eddies (e.g., Nigam et al. 1986, 1988), the correlation coefficients of 0.70 and 0.81 provide convincing evidence which demonstrates that: (1) the linear model can appropriately simulate the stationary eddies, and (2) the winter stationary eddies are primarily maintained by the heating field.

It is shown in Figure 24a that the primary contribution to the winter mean diabatic heating is from its tropical components. Thus, the tropical heating should be the primary mechanism for the maintenance of the NH winter stationary eddies. This conclusion is consistent with that obtained by Simmons (1982) from the response of an idealized model to the tropical diabatic heating. However, Jacqmin and Lindzen (1985) studied the cause of the NH winter stationary waves and found that the extratropical forced component is a major part of the total stationary eddy pattern. In the studies of Nigam et al. (1986) and Valdes and Hoskins (1989), both the tropical and extratropical heating are important to the maintenance of the NH winter stationary eddies. The relative importance of the tropical and extratropical heating to the maintenance of the NH winter stationary eddies has been long debated in studies related to this issue.

2. Diabatic heating versus transient forcing

In the linearized model experiment, the interdecadal change of the atmospheric circulation was analyzed in terms of the difference between the stationary eddies modeled in the 1950s and 1980s perpetual simulations, that is, $\Delta\psi_E$(80s-50s). Shown in Figure 31 are the $\Delta\psi_E$(80s-50s) fields at 200 mb and 850 mb as simulated in the diabatic heating and transient forcing experiments. To examine the relative roles of diabatic heating and transient forcing in the interdecadal circulation variability, the $\Delta\psi_E$(80s-50s) fields simulated in the diabatic heating and transient forcing experiments (Figure 31) are compared with the $\Delta\psi_E$(80s-50s) fields of the GCM experiment (Figure 29). The comparison between Figures 31 and 29 reveals that, as far as the amplitude and spatial structure are concerned, the $\Delta\psi_E$(80s-50s) fields simulated in the diabatic heating experiment at both levels are in agreement with the GCM's. However, the $\Delta\psi_E$(80s-50s) fields from the transient forcing experiment are not well organized and are too weak in their amplitude to compare with the GCM's. Obviously, the diabatic heating anomalies play a more important role than the transient forcing anomalies in maintaining the interdecadal climate change.

Statistically, the spatial correlation coefficient between the $\Delta\psi_E$(80s-50s) fields simulated by the GCM and by the diabatic heating (transient forcing) experiment is 0.70 (0.19) at 200 mb and 0.77 (0.02) at 850 mb. These spatial correlation coefficients are obtained by correlating the 200/850 mb $\Delta\psi_E$(80s-50s) fields shown in Figure 31 with the

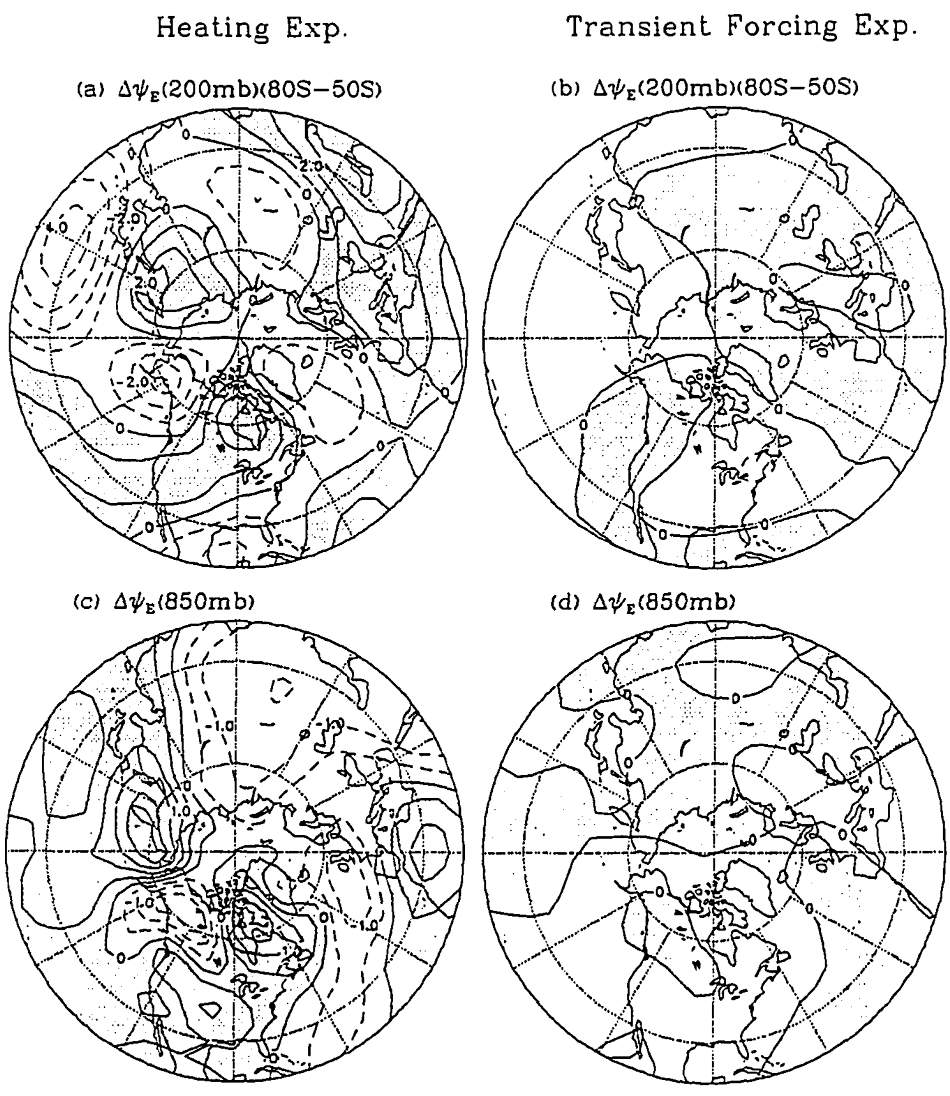

Figure 31. The interdecadal change (1980s-1950s) of 200 mb/ 850 mb eddy streamfunction simulated by the linearized model in the (a)/(c) diabatic heating and (b)/(d) transient forcing experiments. The contour intervals are 10^6 m^2s^{-1} for (a) and (b), and $5x10^5$ m^2s^{-1} for (c) and (d). The positive values are shaded.

200/850 mb $\Delta\psi_E$(80s-50s) fields shown in Figure 29. The above statistical results support the conclusion obtained from the pattern analysis that the diabatic heating anomalies are a vital factor in the GCM's interdecadal climate change. On the other hand, the role of transient forcing anomalies is less important. This result in turn supports the finding from the GCM study that the interdecadal change of transient eddy activity is likely the response, not the cause, of the interdecadal variability of the atmospheric circulation.

Based upon the above pattern and statistical analyses between the GCM (i.e., ER experiment) and the linearized model experiments, we obtain a positive test for the hypothesis: the interdecadal change of diabatic heating is more important than that of transient forcing to the maintenance of the interdecadal climate change.

Although the transient forcing anomalies are less important to the interdecadal climate change, they do exhibit some systematic effect on the interdecadal circulation variability. As show in Figures 31a and 31b, the $\Delta\psi_E$(200 mb)(80s-50s) fields from the diabatic heating and transient forcing experiments have more or less an opposite pattern st high latitudes. For example, over the areas south of Alaska, south of Greenland, and Russia, there are negative centers in Figure 31a but positive anomalies in Figure 31b. The spatial relationship between the $\Delta\psi_E$(80s-50s) fields of the diabatic heating and transient forcing experiments indicates that the transient forcing anomalies exert a dissipative effect on the interdecadal change of the climate system, even if it is very minor. The dissipative effect exerted by the transient eddy activity on the interdecadal circulation variability was also found in the GCM study. In the ER experiment, the function of the transient heat flux is to transport the sensible heat from the warm anomalies to the cold anomalies. With this type of sensible heat transport, the horizontal temperature gradient decreases and the anomalous thermal structure is thus dissipated.

In the diabatic heating experiment, the $\Delta\psi_E$(80s-50s) field at 200 mb (Figure 31a) exhibits three anomalous low centers over the areas south of Alaska, south of Greenland, and Russia. Over these three regions, the equatorward expansions of the circumpolar vortex in the GCM (ER) experiment are most significant. Moreover, these vortex expansions are accompanied by the deepening of stationary troughs. In view of the geographic coincidence between the anomalous low centers in the diabatic heating experiment and the vortex expansions in the ER experiment, one may infer that the major equatorward expansions of the circumpolar vortex can be affected by the diabatic heating anomalies.

The importance of the heating anomalies to the interdecadal change of the atmospheric circulation has been addressed in observational (Falland and Parker 1989; Deser and Blackmon 1993; Chen and Chen 1994) and numerical (e.g., Chen et al. 1992, Graham et al. 1994) studies. However, the role of transient forcing anomalies in the interdecadal circulation variability has not been studied numerically. It is revealed from our linearized model experiment that the transient forcing anomalies exert only minor, but dissipative, effect on the climate system's interdecadal variability.

3. Tropical heating versus extratropical heating

The tropical (extratropical) heating anomalies used in the tropical (extratropical) heating experiment are the same as the diabatic heating anomalies used in the diabatic heating experiment, except the amplitudes of the anomalous tropical (extratropical) centers in the former field are twice as large as those in the latter field. In order to specifically examine the effect of the enhanced tropical (extratropical) heating anomalies on the interdecadal climate change, the $\Delta\psi_E$(80s-50s) field simulated in the diabatic heating experiment is subtracted from that simulated in the tropical (extratropical) heating experiment. After the subtraction, the anomalous patterns induced by the enhanced tropical or extratropical heating anomalies are shown in Figure 32.

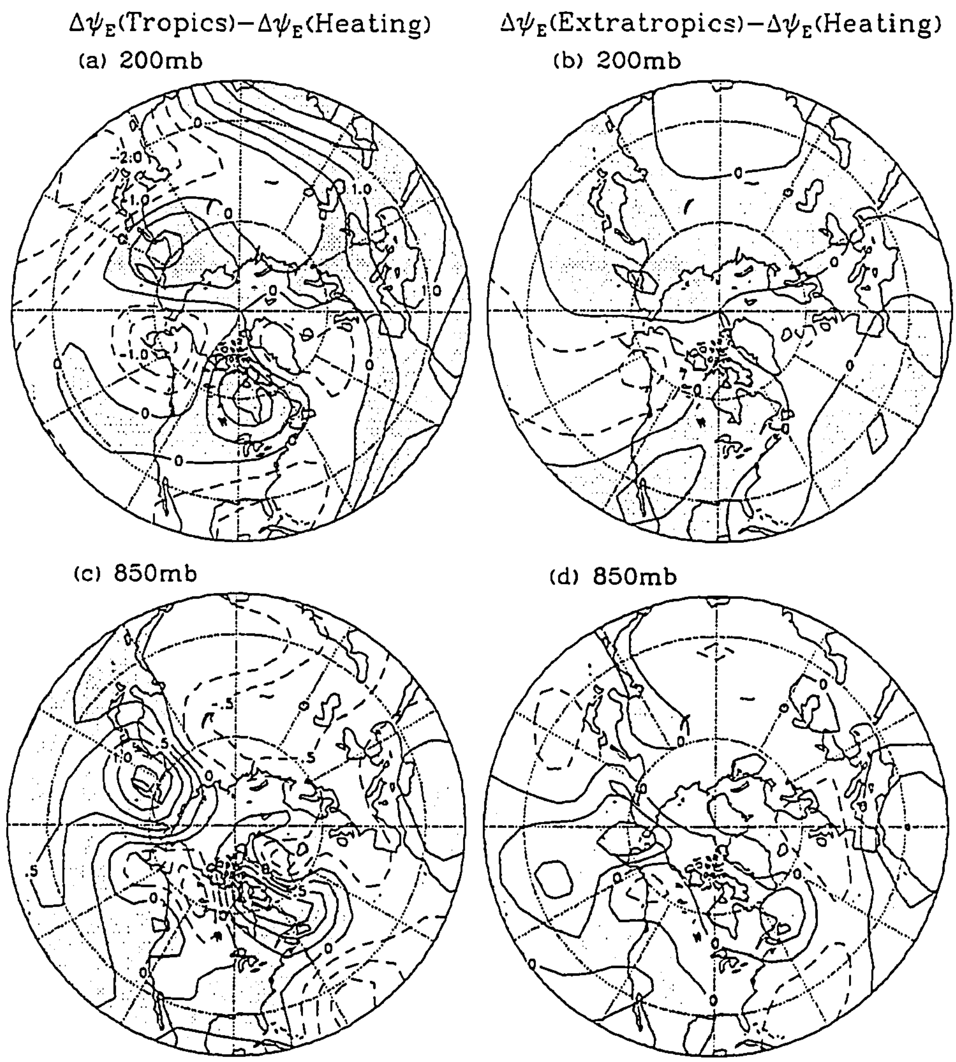

Figure 32. The difference between the interdecadal changes (1980s-1950s) of 200 mb/850 mb eddy streamfunction simulated by the (a)/(c) tropical heating and diabatic heating experiments and (b)/(d) extratropical heating and diabatic heating experiments. The contour intervals are 5×10^5 $m^2 s^{-1}$ for (a) and (b) and 2.5×10^5 $m^2 s^{-1}$ for (c) and (d).

To evaluate the effect of the enhanced heating anomalies on the interdecadal climate change, we compare the anomalous patterns shown in Figure 32 with the $\Delta\psi_E$(80s-50s) fields derived from the GCM study in the Figure 29. The comparison between Figures 32 and 29 reveals that: (1) for the spatial structure, the interdecadal change of stationary eddies generated by the enhanced tropical (extratropical) heating anomalies is similar to the $\Delta\psi_E$(80s-50s) fields from the GCM study at all (only mid- and high-) latitudes, (2) the amplitude of the interdecadal circulation variability induced by the tropical heating anomalies is larger than that induced by the extratropical heating anomalies at all latitudes. These results indicate that both the tropical and extratropical heating anomalies contribute to the interdecadal climate change. However, the contribution of the tropical heating anomalies is more important at all latitudes. The major response of the atmospheric circulation to the interdecadal extratropical heating anomalies is primarily in the mid- and high-latitudes.

In order to quantitatively measure the interdecadal circulation variability induced by the tropical and extratropical heating anomalies, we computed the spatial variance for the anomalous patterns shown in Figure 32. For the tropical hearing experiment, the spatial variances are 7.38×10^{11} m^4s^{-2} at 200 mb and 1.80×10^{11} m^4s^{-2} at 850 mb. For the extratropical heating experiment, the variances are 1.42×10^{11} m^4s^{-2} at 200 mb and 0.45×10^{11} m^4s^{-2} at 850 mb. The intensity of the interdecadal change of stationary eddies generated in the tropical and extratropical heating experiments is about 4~5 to 1.

Based upon the above pattern analysis between the linearized model and GCM experiments and the simple statistical analyses, it is clear that the tropical heating anomalies are more important than the extratropical heating anomalies for inducing the interdecadal change of the NH winter circulation. This result substantiates the hypothesis of this experiment. The importance of tropical heating anomalies to the maintenance of the interdecadal variation modes, as inferred from the χ-maintenance and ψ-budget analyses in the GCM study, has also been verified.

The relative importance of tropical and extratropical heating anomalies to the variability of the NH winter circulation has been long debated in the literature. Namias (1972, 1974) suggested that anomalous NP SSTs are an important forcing mechanism for circulation anomalies over the midlatitude oceans and downstream. This argument was later supported by observational (e.g., Wallace et al 1990) and numerical (e.g., Pitcher et al. 1988; Lau and Nath 1990) studies concerned with the relationship between the atmospheric variability and the NP SSTs. On the other hand, the vitality of tropical heating anomalies to the variability of midlatitude circulations is concluded from observational analyses (e.g., Rowntree 1972; Horel and Wallace 1981), linearized model simulations (e.g., Simmons 1982; Hoskins and Karoly 1981), atmospheric GCM experiments (e.g., Lau and Nath 1994), and coupled ocean-atmosphere model studies (e.g., Alexander 1992a,b).

Recently, Graham et al. (1994) conducted three parallel GCM experiments to examine the effect of tropical and extratropical SST anomalies on the interdecadal variability of the NH circulation. They concluded that the major interdecadal change of the NP winter circulation during the mid-1970s resulted from the changes in tropical SSTs. This result is consistent with the conclusion of our linearized model simulation that the tropical heating anomalies are the primary mechanism for the interdecadal change of the NH winter circulation. Graham et al. also pointed out that the midlatitude SST anomalies are important to the variability of midlatitude circulation over the North Atlantic and western Europe. In our linearized model simulations, the comparison between the NA circulation anomalies in Figures 32a and 32b reveals that the tropical heating anomalies still play a more important role in maintaining the interdecadal circulation variability over the North Atlantic region. The results of our linearized model simulations do not agree with Graham et al.'s in the issue related to the maintenance of the interdecadal circulation variability over the NA region.

4. North-south differential heating

The purpose of this experiment was to examine the effect of changes in north-south differential heating, which is associated with the polar cooling, on the interdecadal circulation variability. The heating anomalies used in the experiment were the summation of the diabatic heating anomalies used in the diabatic heating experiment (Figure 25) and the ideal zonal-mean heating anomalies shown in Figure 28b). In order to specifically examine the effect of the ideal zonal-mean heating anomalies on the interdecadal circulation variability, the difference between the $\Delta\psi_E$(80s-50s) fields simulated in the diabatic heating experiment and the present experiment (the latter minus the former) were used for the analysis (Figure 33).

As shown in Figure 33a, the anomalous pattern at 200 mb induced by the ideal zonal-mean heating anomalies exhibits anomalous lows over the east coasts of the Asian and North American continents and anomalous highs over the west coasts of North America and Europe. This pattern resembles the salient feature of the climatological stationary eddies (Figure 1c). At 850 mb, the anomalous pattern generated by the ideal zonal-mean heating anomalies (Figure 33b) exhibit a

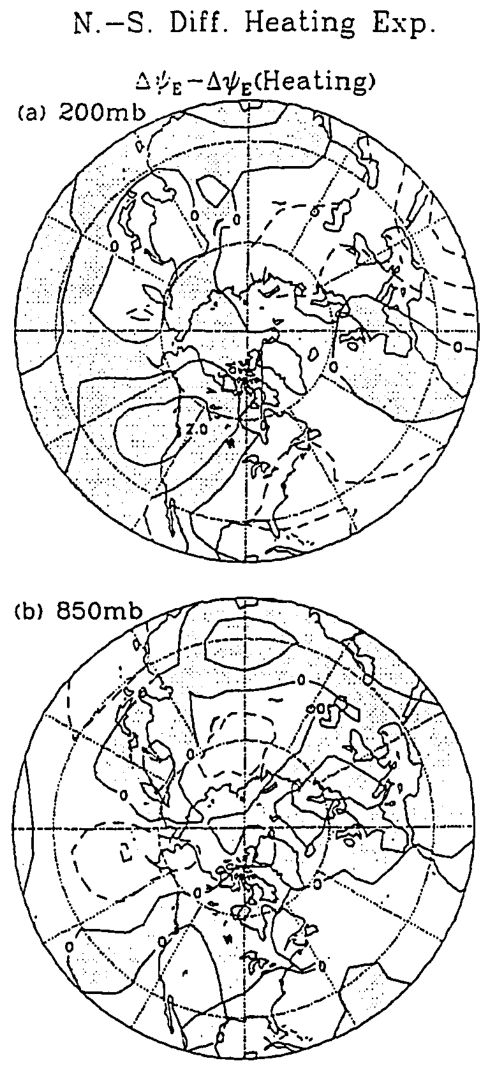

Figure 33. As in Figures 32, except for the difference between the north-south differential heating and diabatic heating experiments. The contour intervals are 10^6 m^2s^{-1} for (a) and $5x10^5$ m^2s^{-1} for (b).

spatial pattern somewhat similar to the mean stationary eddies of the control run in Figure 30c. Based upon the aforementioned results, we suggest that the effect of the ideal zonal-mean heating used in the present experiment is to intensify the stationary eddies. In other words, the polar cooling can cause the amplification of the stationary eddies.

One possible explanation for how the polar cooling can amplify the stationary eddies is provided here. Numerous studies of the atmospheric general circulation have shown that the north-south differential heating is maintained by meridional sensible heat transport (e.g., Wiin-Nielsen and Chen 1993). The major agent for the meridional sensible heat transport is the stationary eddies (e.g., Chen 1982). Given the cooling over the polar cap, more sensible heat should be transported poleward in order to maintain the thermal equilibrium of the NH climate system. In order to satisfy the required enhancement of sensible heat transport, the stationary eddies thus amplify.

E. Summary and Discussion

In order to verify the dynamic processes inferred from the GCM study, the linearized model study was performed. Among the GCM dynamic processes, the relative roles of the diabatic heating anomalies as well as their tropical and extratropical components, transient forcing anomalies, and north-south differential heating anomalies to the interdecadal circulation variability were examined. As far as the interdecadal variability of the NH winter circulation is concerned, the linearized model simulations revealed the following results: (1) the diabatic heating anomalies are more important than the transient forcing anomalies and the effect of the transient forcing anomalies is dissipative and relatively minor; (2) the tropical heating anomalies dominates over the extratropical heating anomalies as the major mechanism for the interdecadal change of the NH winter circulation; (3) the north-south differential heating anomalies, which are designed from an ideal case to represent the polar cooling, causes the amplification of the stationary eddies. The aforementioned three results from the linearized model experiments answer the fifth question raised in the Introduction.

It was demonstrated by our linearized model experiments that diabatic heating anomalies are more important than transient forcing anomalies in the maintenance of the low-frequency modes generated in a GCM with SST anomalies. However, Branstator (1992) and Ting and Lau (1993) demonstrated that transient forcings are more important than the diabatic heating in the maintenance of the atmospheric anomalies generated from a GCM without the anomalous SST forcing. In such a GCM simulation, the low-frequency anomalies may result from internal atmospheric processes such as the barotropic instability (e.g., Simmons et al. 1983). The impact of the barotropic instability on the atmospheric anomalies should be largely reflected by the transient forcings. Therefore, the transient forcing anomalies become the major mechanism maintaining the model low-frequency modes. On the other hand, in a GCM simulation with the anomalous SST forcing, the SST anomalies result in the variability of the diabatic heating which, in turn, induces the variations of the model circulation. The diabatic heating anomalies thus become the vital factor in the maintenance of the model low-frequency variability.

V. CONCLUDING REMARKS AND FUTURE STUDY

A. Concluding Remarks

Previous studies suggest that one of the possible mechanisms responsible for the interdecadal variation of the atmospheric circulation is the interdecadal SST anomalies. It is thus hypothesized in this study that the interdecadal SST change is a possible mechanism for the interdecadal variation of the NH winter circulation. To test this hypothesis, the NCAR CCM1 with R15 resolution was adopted to perform two multi-decade (1946-92) climate simulations with different boundary conditions: a control experiment (EC) incorporating the 12 calendar month climatological SSTs over all oceans and a real-time experiment (ER) using the global real-time SSTs. The effect of the SST anomalies on the interdecadal change of the NH winter circulation was studied by contrasting the results of the EC and ER experiments. The dynamic processes inferred from the GCM study were further verified by linearized model experiments. The linearized model used in our study was derived from the CCM1. The major findings of the GCM and linearized model studies are summarized as follows.

(1) The most significant aspects of the effect exerted by SST anomalies on the interdecadal NH circulation variability are: (a) in the total field, the equatorward expansion of the

circumpolar vortex and the deepening of three climatological troughs and (b) the existence of three interdecadal variation modes in the stationary eddies (PNA, PNAW, and NA).

(2) As for horizontal structure of the interdecadal modes, both the PNA and PNAW modes are characterized by a teleconnection pattern in the Pacific/North America region. The teleconnection pattern of the PNA mode emanates from the tropical central Pacific, but that of the PNAW mode emerges from the tropical western Pacific. The salient feature of the NA mode is a north-south three-cell structure over the Greenland/North Atlantic region. The vertical structure of these three interdecadal modes are all equivalent barotropic. As for the temporal characteristics, the time evolution of these three modes consists of a decadal trend plus low-frequency (15~20 years) oscillations.

(3) As suggested by the χ-maintenance and ψ-budget analyses, the possible physical processes associated with the maintenance of the interdecadal variation modes are: (a) the tropical heating anomalies maintain the interdecadal change of the divergent circulation, and (b) the divergent circulation anomalies in turn interact with the anomalous rotational circulation so as to induce the interdecadal circulation variability.

(4) The interdecadal change of the general circulation statistics is regulated by the interdecadal variation of the

atmospheric circulation. In the thermal field, the transient heat flux diverges out of the warm anomalies and converges toward the cold anomalies. In the dynamic field, the interdecadal change of cyclone activity over the midlatitude storm track regions is regulated by the variability of north-south wind shear which is induced by the equatorward expansion of the circumpolar vortex.

(5) The linearized model simulations demonstrate that, as far as the maintenance of the interdecadal change of the NH winter circulation is concerned, (a) the diabatic heating anomalies are more important than the transient forcing anomalies, (b) the tropical heating anomalies dominate over the extratropical heating anomalies as the primary mechanism for the NH interdecadal circulation variability, and (c) the polar cooling can cause the amplification of stationary waves.

The results obtained from the present numerical study substantiate the hypothesis that the interdecadal SST change is one of the possible mechanisms for the interdecadal variability of the NH winter circulation. In addition, the present numerical study provides some advantages, with respect to the observational study, in studying the interdecadal circulation variability: (1) the effect of the interdecadal SST anomalies on the overlying atmosphere can be specifically examined and (2) the impact of tropical forcing on the interdecadal atmospheric anomalies can be studied (note that the observational data with multi-decade length are only available in the extratropics). On the other hand, the present study has a deficiency: the lack of possible mechanisms, other than the SST anomalies, in the simulations. Chen and Chen (1994) suggest that the Atlantic thermohaline circulation and polar cooling are two of the possible mechanisms for the interdecadal climate change. In order to incorporate the Atlantic thermohaline circulation, a coupled ocean-atmosphere model is needed. As for the polar cooling, Chen and Chen (1994) suggest that the most likely physical processes responsible for this cooling is radiative. For example, the increase of sea ice and cloudiness may result in the increase of albedo which reinforces the polar cooling.

Because the SST anomalies are only one of the several possible mechanisms for the interdecadal circulation variability, it is not surprising to find that the interdecadal circulation change simulated in our GCM experiment is different from the observed. Chen and Chen (1994) have identified two interdecadal modes from the observed stationary eddies: Pacific and Atlantic modes. They further suggest that the interdecadal Pacific mode may result from the mutual interactions of the Pacific Ocean and the atmospheric circulation, while the interdecadal Atlantic mode seems likely to be affected by the interdecadal change of the

Atlantic thermohaline circulation. In our real-time GCM experiment, the model generates one interdecadal mode over the North Atlantic region (i.e., NA mode) and two interdecadal modes over the North Pacific region (i.e., PNA and PNAW modes). As far as the existence of the interdecadal modes are concerned, the result of the model simulation is consistent with observations over the North Atlantic, but different over the North Pacific. Although the Atlantic Ocean is not included in our GCM simulation, the effect of the ocean on the atmospheric circulation variability can to some extent be exerted by the prescribed SST anomalies. Therefore, the consistency, in terms of the existence of interdecadal modes, between the model simulation and observations over the North Atlantic suggests that the observed NA interdecadal circulation variability is affected by the variations of the Atlantic Ocean. Similarly, the inconsistency between the existence of simulated and observed interdecadal modes over the Pacific implies that the effect of the ocean on the overlying atmosphere is not the only mechanism that affects the NP interdecadal circulation change. In other words, the observed interdecadal Pacific mode is likely induced by the mutual interactions between the Pacific Ocean and the overlying atmosphere.

B. Suggestions for Future Study

Although the present study provides some insights into the dynamic processes related to the interdecadal change of the ocean-atmosphere system, more questions remain unanswered:

(1) It was suggested by Chen and Chen (1994) and our GCM study that polar cooling is one possible mechanism for the interdecadal change of the NH winter circulation. Chapman and Walsh (1993) analyzed the interdecadal trends of the NH surface temperature and arctic sea ice. They demonstrated that the cooling over the polar cap is associated with the increase of sea ice. In view of the aforementioned results, we may ask what is the impact of the interdecadal sea ice anomalies on the overlying atmosphere? In particular, to what extent can the interdecadal sea ice anomalies affect the horizontal variation of the circumpolar vortex?

(2) As for the midlatitude circulation's variability, the relative importance of tropical and midlatitude SST anomalies has been studied by GCM experiments with the anomalous SST forcing from each of the two regions (Lau and Nath 1994; Graham et al. 1994). In view of the existence of the interdecadal variation modes over the NP and NA regions, one may ask what are the relative roles of the Pacific and Atlantic SST anomalies in the interdecadal change of

midlatitude atmospheric circulation. This issue has not been clarified by numerical studies to date.

(3) Recently, Miller et al. (1994) forced an ocean GCM with the observed atmospheric anomalous forcings and successfully simulated the 1977 wintertime climate shift in the Pacific SST field. As indicated by this study, the feedback processes from the atmosphere to the ocean is important in the ocean-atmosphere system. Nevertheless, an atmospheric GCM, such as the CCM1, is unable to incorporate these feedback processes because the SST forcing is prescribed. The alternative is to employ a coupled ocean-atmosphere model to simulate the interdecadal climate variability. With the coupled model, the effect of the interdecadal change of the Atlantic thermohaline circulation on the atmospheric anomalies can also be examined.

REFERENCES

Alexander, M. A., 1992a. Midlatitude atmosphere-ocean interaction during El Nino. Part I: The North Pacific Ocean. *J. Climate* 5, 944-958.

Alexander, M. A., 1992b. Midlatitude atmosphere-ocean interaction during El Nino. Part II: The Northern Hemisphere Atmosphere. *J. Climate* 5, 959-972.

Alexander, R. C. and R. L. Mobley, 1976. Monthly average sea-surface temperature and ice-pack limits on a 1° global grid. *Mon. Wea. Rew.* 104, 143-148.

Arpe, K. and E. Klinker, 1986. Systematic errors of the ECMWF operational forecast model in the midlatitudes. *Quart. J. Roy. Meteor. Soc.* 112, 181-202.

Barnett, T. P., 1984. Long-term trends in surface temperature over the oceans. *Mon. Wea. Rew.* 112, 303-312.

Bjerknes, J., 1964. Atlantic air-sea interaction. Advance in Geophysics. Academic Press, New York, 1-82.

Blackmon, M. L., J. E. Geisler, and E. J. Pitcher, 1983. A general circulation model study of January climate anomaly patterns associated with interannual variation of equatorial Pacific sea surface temperatures. *J. Atmos. Sci.* 40, 1410-1425.

Blackmon, M. L., J. M. Wallace, N.-C. Lau, and S. L. Mullen, 1977. An observational study of the Northern Hemisphere wintertime circulation. *J. Atmos. Sci.* 34, 1040-1053.

Bourke, W., B. McAvaney, K. Prui and R. Thurling, 1977. Global modeling of atmospheric flow by spectral methods. Methods in Computational Physics, Vol. 17, General Circulation Models of The Atmosphere, Academic Press, 267-324.

Branstator, G., 1985a. Analysis of general circulation model sea-surface temperature anomaly simulations using a linear model. Part I: Forced solutions. *J. Atmos. Sci.* 42, 2225-2241.

Branstator, G., 1985b. Analysis of general circulation model sea-surface temperature anomaly simulations using a linear model. Part II: Eigenvalue problems. *J. Atmos. Sci.* 42, 2242-2254.

Branstator, G., 1990. Low-frequency patterns induced by stationary waves. *J. Atmos. Sci.* 47, 629-648.

Branstator, G., 1992. The maintenance of low-frequency atmospheric anomalies. *J. Atmos. Sci.* 49, 1924-1945.

Burnett, A. W., 1993. Size variations and long-wave circulation within the January Northern Hemisphere circulation vortex: 1946-89. *J. Climate* 6, 1914-1920.

Chapman, W. L. and J. E. Walsh, 1993. Recent variation of sea ice and air temperature in high latitudes. *Bull. Amer. Meteor. Soc.* 74, 33-47.

Chen, T.-C., 1982. A further study of spectral energetics in the winter atmosphere. *Mon. Wea. Rew.* 110, 947-961.

Chen, T.-C., H. van Loon, K.-D. Wu and M.-C. Yen, 1992. Changes in the atmospheric circulation over the North Pacific-North America area since 1950. *J. Meteor. Soc. Japan* 70, 1137-1146.

Chen, T.-C. and J.-M. Chen, 1990. A note on the maintenance of stationary eddies with the streamfunction budget analysis. *J. Atmos. Sci.* 47, 2818-2824.

Chen, T.-C. and J.-M. Chen, 1994. Interdecadal variation of the wintertime Northern-Hemisphere circulation in the past four decades. (submitted to Journal of Climate)

Chen, T.-C. and M.-C. Yen, 1991a. A study of the diabatic heating associated with the Madden-Julian oscillation. *J. Geophys. Res.* 13,163-177.

Chen, T.-C. and M.-C. Yen, 1991b. Interaction between intraseasonal oscillation of the midlatitude flow and tropical convection during 1979 northern summer: The Pacific ocean. *J. Climate* 4, 653-671.

Chen, T.-C. and M.-C. Yen, 1993. Interannual variation of summertime stationary eddies. *J. Climate* 6, 2263-2277.

Chen, T.-C. and M.-C. Yen, 1994a. Interannual variation of the Indian monsoon simulated by the NCAR Community Climate Model: Effect of the tropical Pacific SST. *J. Climate* 7, 1403-1415.

Chen, T.-C. and M.-C. Yen, 1994b. An alternative index for interannual variation of the atmospheric circulation: Relative atmospheric angular momentum. (pending review)

Chen, T.-C. and M.-C. Yen, J. Pfaendtner, and Y. C. Sud, 1993. The vertical structure of diabatic heating associated with the Madden-Julian oscillation simulated by the Goddard Laboratory for Atmosphere climate model. *J. Geophys. Res.* 98, 8801-8813.

Chen, T.-C. and W. E. Baker, 1986. Global diabatic heating during FGGE SOP-1 and SOP-2. *Mon. Wea. Rew.* 114, 2578-2589.

Douglas, A. V., D. R. Cayan and J. Namias, 1982. Large scale changes in North Pacific and North America weather patterns in recent decades. *Mon. Wea. Rew.* 112, 1185-1862.

Folland, C. K. and D. Parker, 1989. Observed variations of sea surface temperature. Proc. NATO Advanced research Workshop on Climate-Ocean Interaction, Oxford, England, September 1988, Kluwer Academic Press.

Geisler, J. E., M. L. Blackmon, G. T. Bates, and S. Munoz, 1985. Sensitivity of January climate response to the magnitude and position of equatorial Pacific sea surface temperature anomalies. *J. Atmos. Sci.* 42, 1037-1049.

Graham, N. E., T. P. Barnett, R. White, M. Ponater, and S. Schubert, 1994. On the roles of tropical and midlatitude SSTs in forcing interannual to interdecadal variability in the winter Northern Hemisphere Circulation. *J. Climate* 7, 1416-1441.

Held, I. M., 1984. Stationary and quasi-stationary eddies in the extratropical troposphere: theory. In "Large-Scale Dynamical Processes in the Atmosphere", Academic Press, 397 PP.

Hense, A., P. Krahe and H. Flohn, 1988. Recent fluctuations of tropospheric temperature and water vapor content in the tropics. *Meteor. Atmos. Phys.* 38, 215-227.

Hollingworth, A., K. Arpe, M. Tiedtke, M. Capaldo, and H. Sarijarvi, 1980. The performance of a medium-range forecast model in winter: Impact of physical parameterization. *Mon. Wea. Rew.* 108, 1736-1773.

Holloway, J. L. Jr. and S. Manabe, 1971. Simulation of climate by a global general circulation model, 1, Hydrological cycle and heat balance. *Mon. Wea. Rew.* 99, 335-370.

Holton, J. R., 1992. An Introduction to Dynamic Meteorology. 3rd ED. Academic Press, 507 PP.

Horel, J. D. and J. M. Wallace, 1981. Planetary-scale atmospheric phenomena associated with the Southern Oscillation. *Mon. Wea. Rew.* 109, 813-829.

Hoskins, B. J. and D. J. Karoly, 1981. The steady linear response of a spherical atmosphere to thermal and orographic forcing. *J. Atmos. Sci.* 38, 1179-1196.

Jacqmin, D. and R. S. Lindzen, 1985. The causation and sensitivity of the northern winter planetary waves. *J. Atmos. Sci.* 42, 724-745.

Jones, P. D., 1988, Hemispheric surface air temperature variation: Recent trends and an update to 1987. *J. Climate* 1, 654-660.

Kasahara, A. 1982. Nonlinear normal mode initialization and the bounded derivative method. *Rev. Geophys Space Phys.* 20, 385-397.

Kitoh, A., 1992. Interannual variations in an atmospheric GCM forced by the 1970-1989 SST. Part II: Low-frequency variability of the wintertime Northern Hemisphere extratropics. *J. Meteor. Soc. Japan* 63, 271-291.

Knox, J. L., K. Higuchi, A. Shabbar and N. E. Sargent, 1988. Secular variation of Northern Hemisphere 50 Kpa geopotential height. *J. Climate* 1, 500-511.

Kushnir, Y., 1994. Interdecadal variations in North Atlantic sea surface temperature and associated atmospheric circulations. *J. Climate* 7, 141-157.

Kutzbach, J. E., 1967. Empirical eigenvectors of sea-level pressure, surface temperature and prediction complexes over North America. *J. Appl. Meteor.* 6, 791-802.

Lau, N.-C., 1978. On the three-dimensional structure of the observed transient eddy statistics of the Northern Hemisphere wintertime circulation. *J. Atmos. Sci.* 35, 1900-1922.

Lau, N.-C., 1981. A diagnostic study of recurrent meteorological anomalies appearing in a 15-year simulation with a GFDL general circulation model. *Mon. Wea. Rew.* 109, 2287-2311.

Lau, N.-C., G. H. White and R. L. Jenne, 1981. Circulation statistics for the extratropical northern hemisphere based on NMC analyses. NCAR Tech. Note, NCAR/TN-171+STR, 138 PP.

Lau, N.-C., 1985. Modeling the seasonal dependence of the atmospheric response to observed El Ninos. *Mon. Wea. Rew.* 113, 1970-1996.

Lau, N.-C. and J. M. Wallace, 1979. On the distribution of horizontal transports by transient eddies in the Northern Hemisphere wintertime circulation. *J. Atmos. Sci.* 36, 1844-1860.

Lau, N.-C. and M. J. Nath, 1990. A general circulation model study of the atmospheric response to extratropical SST anomalies observed during 1950-79. *J. Climate* 3, 965-989.

Lau, N.-C. and M. J. Nath, 1994. A modeling study of the relative roles of tropical and extratropical SST anomalies in the variability of global atmosphere-ocean system. *J. Climate* 7,1184-1207.

Madden, B., 1979. Observations of large-scale travelling Rossby waves. *Rev. Geoph. Space Phys.* 17,1935-1949.

Madden, R. A. and K. Labitzke, 1981. A free Rossby wave in the troposphere and stratosphere during January 1979. *J. Geoph. Res.* 86, C2, 1247-1254.

Miller, A. J., D. R. Cayan, T. P. Barnett, N. E. Graham and J. M. Oberhuber, 1994. Interdecadal variability of the Pacific Ocean: Model response to observed heat flux and wind stress anomalies. *Climate Dym.* 9, 287-302.

Namias, J., 1972. Experiments in objectively predicting some atmospheric and oceanic variables for the winter of 1971-72. *J. Appl. Meteor.* 11, 1164-1174.

Namias, J., 1974. Longevity of a coupled air-sea-continent system. *Mon. Wea. Rew.* 102, 638-648.

Nigam, S., I. M. Held and S. W. Lyons, 1986. linear simulation of the stationary eddies in a general circulation model. Part I: The no-mountain model. *J. Atmos. Sci.* 43, 2944-2961.

Nigam, S., I. M. Held and S. W. Lyons, 1988. Linear simulation of the stationary eddies in a general circulation model. Part II: The mountain model. *J. Atmos. Sci.* 45, 1433-1452.

Nitta, T. and S. Yamada, 1989. Recent warming of tropical sea surface temperature and its relationship to the Northern Hemisphere circulation. *J. Meteor. Soc. Japan* 67, 375-383.

Palmer, T. N. and Z. Sun, 1985. A modeling and observational study of the relationship between sea surface temperature in the north-west Atlantic and the atmospheric general circulation. *Quart. J. Roy. Meteor. Soc.* 111, 947-975.

Pitcher, E. J., M. J. Blackmon, G. T. Bates, and S. Munoz, 1988. The effect of North Pacific sea surface temperature anomalies on the January climate of a general circulation model. *J. Atmos. Sci.* 45, 173-188

Posmentier, E. S., M. A. Cane and S. E. Zebiak, 1989. Tropical Pacific climate trends since 1960. *J. Climate* 2, 731-736.

Rogers, J. C. and M. N. Raphael, 1992. Meridional eddy sensible heat fluxes in the extremes of the Pacific/North American teleconnection pattern. *J. Climate* 5, 127-139.

Rowntree, P. R., 1972. The influence of tropical east Pacific Ocean temperature of the atmosphere. *Quart. J. Roy. Meteor. Soc.* 98, 290-321.

Shabbar, A., K. Higuchi and J. L. Knox, 1990. Regional analysis of Northern Hemisphere 50 KPa geopotential heights from 1946 to 1985. *J. Climate* 3, 543-557.

Simmons, A. J., 1982. The forcing of stationary wave motion by tropical diabatic heating. *Quart. J. Roy. Meteor. Soc.* 108, 503-534.

Simmons, A. J., J. M. Wallace and G. Branstator, 1983. Barotropic wave propagation and instability, and atmospheric teleconnection patterns. *J. Atmos. Sci.* 40, 1363-1392.

Ting, M. and N.-C. Lau, 1993. A diagnostic and modeling study of the monthly mean wintertime anomalies appearing in a 100-year GCM experiment. *J. Atmos. Sci.* 50, 2845-2867.

Trenberth, K. E., 1990. Recent Observed interdecadal climate changes in the Northern Hemisphere. *Bull. Amer. Meteor. Soc.* 71, 988-993.

Trenberth, K. E. and J. W. Hurrell, 1994. Decadal atmosphere-ocean variation in the Pacific. *Climate Dym.* 9, 303-319.

Tzeng, R.-Y. and T.-C. Chen, 1990. A numerical study of blocking. Technical Rep, Iowa State University, 163 PP.

Valdes, P. J. and B. J. Hoskins, 1989. Linear stationary waves simulations of the time-mean climatological flow. *J. Atmos. Sci.* 46, 2509-2527.

van Loon, H. and J. C. Rogers, 1978. The seesaw in winter temperatures between Greenland and Northern Europe. Part I: General description. *Mon. Wea. Rew.* 106, 296-310.

van Loon, H. and J. Williams, 1976. The connection between trend of mean temperature and circulation at the surface : Part I. Winter. *Mon. Wea. Rew.* 104, 365-380.

Wallace, J. M., C. Smith and Q. Jiang, 1990. Spatial patterns of atmosphere-ocean interaction in the northern winter. *J. Climate* 3, 990-998.

Wallace, J. M. and D. S. Gutzler, 1981. Teleconnections in the geopotential height field during the Northern Hemisphere winter. *Mon. Wea. Rew.* 109, 784-812.

Wallace, J. M., Y. Zhang and K.-H. Lau, 1993. Structure and seasonality of interannual and interdecadal variability of the geopotential height and temperature fields in the Northern Hemisphere troposphere. *J. Climate* 6, 2063-2082.

Wiin-Nielsen, A. and T.-C. Chen, 1993. Fundamentals of Atmospheric Energetics. Oxford University Press, 376 PP.

Willett, H. C., 1950. Temperature trends of past century. Cent. Proc. Roy. Meteor. Soc. 195-206.

Williamson, D. L., J. T. Kiehl, V. Ramanathan, R. E. Dickinson and J. J. Hack, 1987. Description of NCAR Community Climate Model (CCM1). NCAR Tech. Note, NCAR/TN-285+STR, 112 PP.

Williamson, G. S. and D. L. Williamson, 1987. Circulation statistics from seasonal and perpetual January and July simulations with the NCAR Community Climate Model (CCM1): R15. NCAR Tech. Note, NCAR/TN-302+STR, 199 PP.

Woodruff, S. D., R. J. Slutz, R. L. Jenne and P. M. Steurer, 1987. A comprehensive ocean-atmosphere data set. *Bull. Amer. Meteor. Soc.* 68, 1239-1250.

ACKNOWLEDGMENTS

I wish to extend my sincere thanks to my major professor, Dr. Tsing-Chang Chen, for his instruction and support throughout my academic life at ISU and the course of this study.

Thanks also go to Drs. Douglas N. Yargar, Richard E. Carlson, Rujbir Dahiya, and William J. Gutowski, Jr. at ISU and Grant Branstator at NCAR for serving on my committee. The assistance provided by Dr. Ming-Cheng Yen in conducting the GCM experiments is greatly appreciated.

Additional thanks go to Ms. Ai-Chin Wang for her typing and Mr. Alvin Kapeyeh, Thomas G. Rink, and Christopher K. Wikle for their editorial help of this manuscript. This study was sponsored by the NSF Grant ATM-9416954, the DOE-NIGEC Grant LWT 62-123-06054, and a CGRER seed Grant V57896.